RESERVOIR FLUID TRANSPORT IN ORGANIC NANOPORES WITH MOLECULAR MODELING AND SIMULATION

A Dissertation

by

FENG FENG

Submitted to the Office of Graduate and Professional Studies of
Texas A&M University
in partial fulfillment of the requirements for the degree of

DOCTOR OF PHILOSOPHY

Chair of Committee,	I. Yucel Akkutlu
Committee Members,	Thomas A. Blasingame
	John Killough
	Yossef Elabd
Head of Department,	Jeff Spath

May 2019

Major Subject: Petroleum Engineering

ABSTRACT

Transport of small hydrocarbon molecules inside organic nanopores is important to our understanding of oil and gas production from source rocks such as shale. Unlike flow in conventional reservoirs, the fluid transport in unconventional reservoirs involves kerogen pore structure with much smaller capillaries. This, in turn, leads to large capillary wall surface area and, consequently, to a significant physical adsorption effect. Measurements are needed to understand the nature of flow inside kerogen structures. However, direct measurements are difficult and have large uncertainties related to kerogen isolation. Non-equilibrium molecular dynamics simulation allows numerical study of fluid transport inside model nanocapillaries representative of kerogen matrices.

First, we studied the transport in 1-D in single nanocapillaries. Based on the simulation results we observe that fluid flow velocity and mass flux are significant near the capillary surfaces where adsorption takes place. Hence, Hagen-Poiseuille equation based on the no-flow condition at the wall significantly underestimates the fluid flow in nanocapillary. The dependence of surface transport velocity, as well as flow enhancement, are determined quantitatively.

Second, we expand our study into 3-D nanoporous networks. Existing molecular models use nanoscale capillaries and do not describe the exact geometric structure of the organic nanopores in real source rocks, especially for mesopores, which widely exist in organic solids and are crucial for fluid transport in the source rocks. Here we present a new method to simplify the existing molecular kerogen models. Pore structures can be

built to reflect the exact porous structure of hydrocarbon bearing kerogen pores for fluid transport without losing accuracy. The kerogen pore network skeleton can be populated based on 3-D digital segments obtained from high-resolution TEM tomographs. We introduce a simplified molecular model approach to work with significantly larger volumes of 3-D segments. To test the transport simulation accuracy using molecular dynamics for this simplified model, sample pore network structures are populated with both the existing exact molecular model and the simplified model, the permeability of reservoir fluid flowing through the media is simulated and compared. The simplified kerogen model can be easily applied to larger organic porous material samples to reduce spatial uncertainty.

DEDICATION

To

My Family

and

My Professors

with

Love and Gratitude

ACKNOWLEDGEMENTS

I would like to thank all my committee members, for all their generosity with their precious time and expertise. Especially I want to thank Dr. Yucel Akkutlu, my advisor and the committee chair, for his hours of mentoring, encouraging, supporting, and the patience, especially during my down-times. I appreciate Dr. Tom Blasingame, Dr. John Killough and Dr. Yossef Elabd for agreeing to serve in my committee; and Dr. Jeff Spath for being the department head and helping to provide internship opportunities during my studies.

I also like to thank all the staff of the Department of Petroleum Engineering and Texas A&M University High-Performance Research Computing Center for providing resources and technical support and thank the Crisman Institute of Petroleum Research, and Dr. Stephen Holditch for the financial support to pursue my graduate studies at Texas A&M.

Finally, I would like to thank my colleagues for fruitful discussions, especially Dr. Khoa Bui; to thank to my parents, wife and in-laws for their encouragement and to my wife for her patience and love.

CONTRIBUTORS AND FUNDING SOURCES

Contributors

This work was supervised by a dissertation committee consisting of Professor I. Yucel Akkutlu (Chair of Committee), Thomas A. Blasingame, and John Killough of the Department of Petroleum Engineering, and Professor Yossef Elabd of the Department of Chemical Engineering. All work conducted for the dissertation was completed by the student independently.

Funding Sources

Graduate study was supported by a graduate research assistantship from Texas A&M University.

This work was also made possible in part by Crisman Institute of Petroleum Research under Grant Number 3.1.28. Its contents are solely the responsibility of the authors and do not necessarily represent the official views of the Crisman Institute of Petroleum Research

NOMENCLATURE

a	length of the bump
a	acceleration
b	length of the trench
c	molar concentration
Δc	concentration drop
d	inner diameter of the carbon nanotube
d	molecular diameter
D	diffusion coefficient
f	fugacity
f	external force in EF-NEMD
f	probability density in phase space
F	force
dp/dl, dp/dz	pressure gradient
m	atomic mass
n	number of atoms
h	height of the bump, nm
$L(c)$	transport coefficient
J	molar flux
k_B	Boltzmann constant
k	permeability

k_0	permeability, Darcy
k_{app}	permeability, apparent
Kn	Knudsen number
p	pressure
ΔP	pressure drop
q_{total}	total volumetric flux per capillary
q_{H-P}	volumetric flux from Hagen-Poiseuille equation
$q_{surface}$	volumetric flux per capillary contributed by surface velocity
q	atomic charge
R	radius of the capillary
R^2	coefficient of determination
Re	Reynolds number
r	distance to the center of capillary
r_{ij}	distance between two LJ sites
T	temperature, K
U_{ij}^{LJ}	Lennard-Jones interaction energy
v	velocity, m/s
v_z	streaming velocity along z direction, m/s
$\overline{v_x}$	average Darcy velocity, m/s
x	molar fraction
V, E, U	potential energy

β	thermal dynamic beta, $\frac{1}{k_B T}$
ρ	density
μ	viscosity
μ	chemical potential
σ_{ij}	distance between LJ sites
ϵ_{ij}	energy scale of the interaction between LJ sties
ϵ	permittivity
λ	mean free path
Ω	Bhatnagar–Gross–Krook operator
τ	relaxation time

TABLE OF CONTENTS

Page

LIST OF FIGURES

Page

LIST OF TABLES

Page

CHAPTER I

INTRODUCTION AND LITERATURE REVIEW

Background

Shale gas has attracted increasing attention as an important energy resource in recent years due to improvements in horizontal drilling and hydraulic fracturing techniques. This has invoked interest from several fields including fossil energy, chemical engineering and environmental science (Estrada & Bhamidimarri, 2016; Soeder et al., 2014; Q. Wang, Chen, Jha, & Rogers, 2014). Over the last decade, gas production from organic-rich source rocks has increased to over 40% of the total natural gas production in North America, and the future growth in using this energy source is anticipated worldwide (Figure 1, Figure 2).

Shale gas is categorized among unconventional resources, in the same category as coal bed methane (CBM) and tight gas. And the storage and transport processes of shale gas shares similarities and complexities to both CBM and tight gas. As a result, the experimental and theoretical work based on CBM and tight gas are widely applied for the study of shale gas systems (Figure 3). However, because they possess a multiscale pore structure with pore sizes spanning orders of magnitude from the molecular scale to the macroscopic scale, in both organic and inorganic forms, shale formations have added complexities. Hence, the methods of investigation used bot for tight gas and coal bed methane, including both experimental and theoretical, must be improved and new.

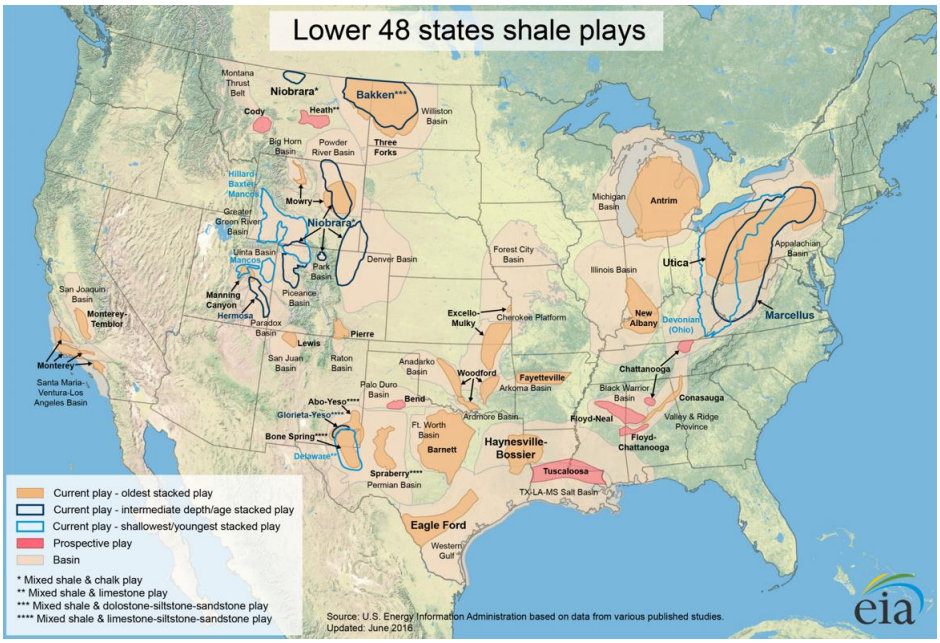

Figure 1. Shale gas and oil plays, Lower 48 States (6/30/2016) ("Shale gas and oil plays, Lower 48 States (6/30/2016)," 2016)

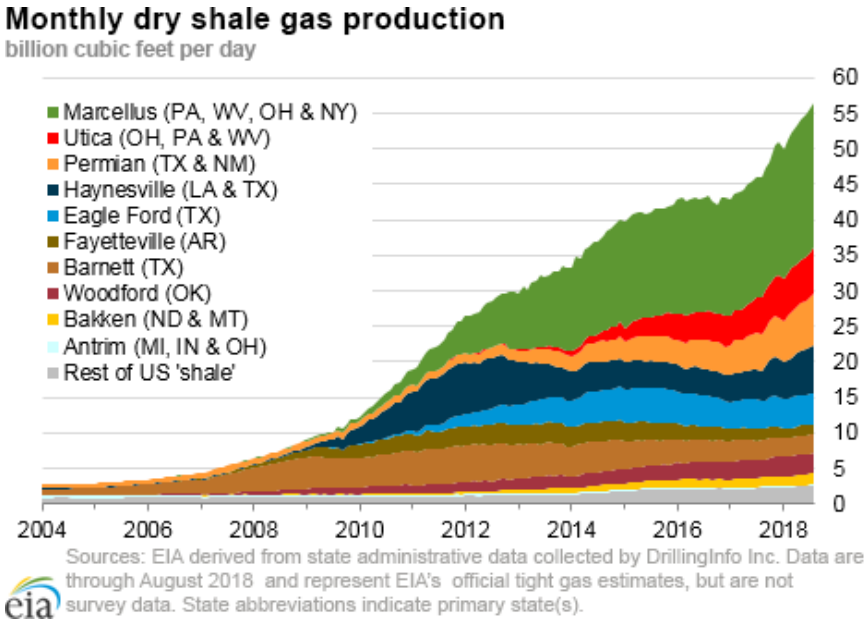

Figure 2. Monthly dry shale gas production of U.S. (Reprinted from "Natural Gas Weekly Update," 2018)

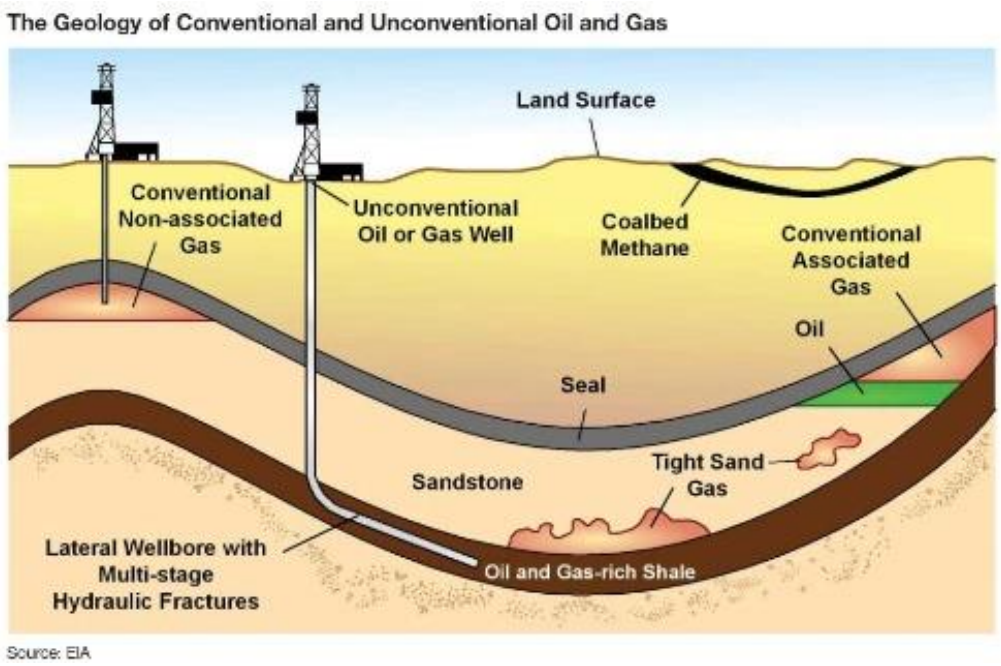

Figure 3. The geology of conventional and unconventional oil and gas (Reprinted from "Natural Gas Weekly Update," 2018)

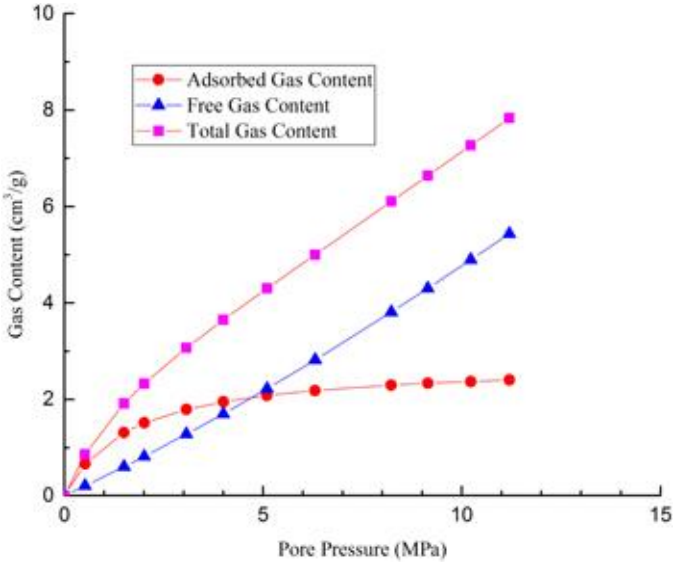

Figure 4. Gas content versus pore pressure for a typical shale plug (Reprinted from K. Liu, Sun, Gu, Liu, & Chen, 2017)

methodologies must be developed for understanding the shale formations (Etminan, Javadpour, Maini, & Chen, 2014)

The storage capacity of shale gas reservoirs is due to: 1) free compressed gas in the organic and inorganic pore network; 2) adsorbed gas on the surface of organic material pore network; 3) absorption or dissolution in liquids (oil and water) in the organic and inorganic pore network and in the solid organic matter. Previous researchers have shown that a substantial amount of hydrocarbon is stored in the organic nanopores, which can be potentially tapped into using improved recovery technologies (I Yucel Akkutlu & Didar, 2013; Hartman, Ambrose, Akkutlu, & Clarkson; Rahmani & Akkutlu, 2015). The adsorption of molecules on the inorganic surfaces are comparatively less, so this research mainly focuses on the adsorption on organic (kerogen) surfaces. Previous researchers also showed the importance of adsorbed hydrocarbons on production, both experimentally and theoretically (Figure 4, Figure 5). The production decline curves from the U.S. shale plays (Figure 6) show that the production rate of shale gas wells declines fast, with the adsorbed gas remain mostly untapped. This indicates there is potential to produce the adsorbed gas with future technologies apart from hydraulic fracturing.

Adsorption is the physical adhesion of molecules/atoms/ions onto a surface of a material. The adsorption process creates a film of hydrocarbon molecules on the surface of the kerogen pore walls, which differs from the process of absorption, in which the fluid permeates into the volume of solid kerogen. Sorption is the general terms for both processes, and desorption is the reverse process of them. The adsorption phase has

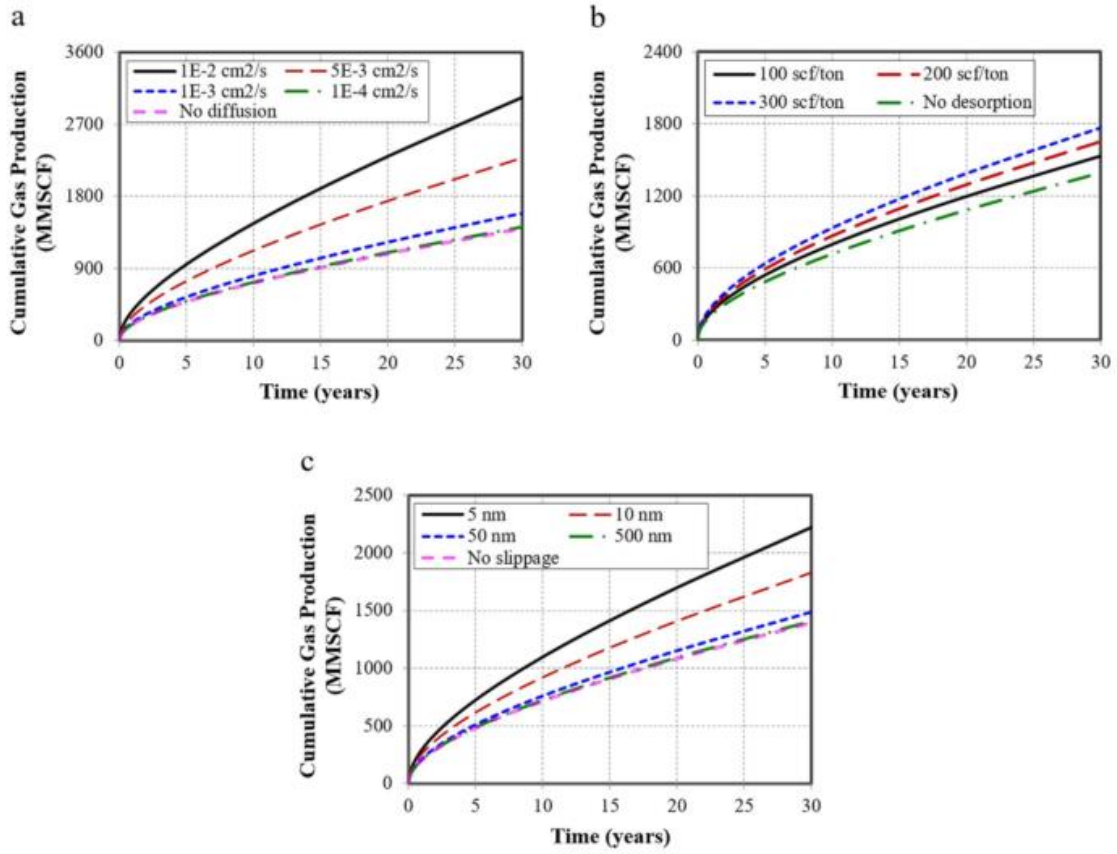

Figure 5. Effects of three gas transport mechanisms on cumulative gas production. (a) Effect of gas diffusion with different gas diffusion coefficients. (b) Effect of gas desorption with different Langmuir volumes. (c) Effect of gas slippage with different pore diameters (Reprinted from R. Y. Yang et al., 2016).

unique physical and chemical properties compared to the bulk fluid. When the specific surface area of a material is high, such as kerogen, the percentage of the adsorbed fluid is no longer negligible comparing to the total fluid amount in contact with the porous material, and the impact of adsorption may even dominate the overall fluid behavior. Kerogen is a typical example of a nanoporous material with significant amount of sorption in its nanopores with organic walls.

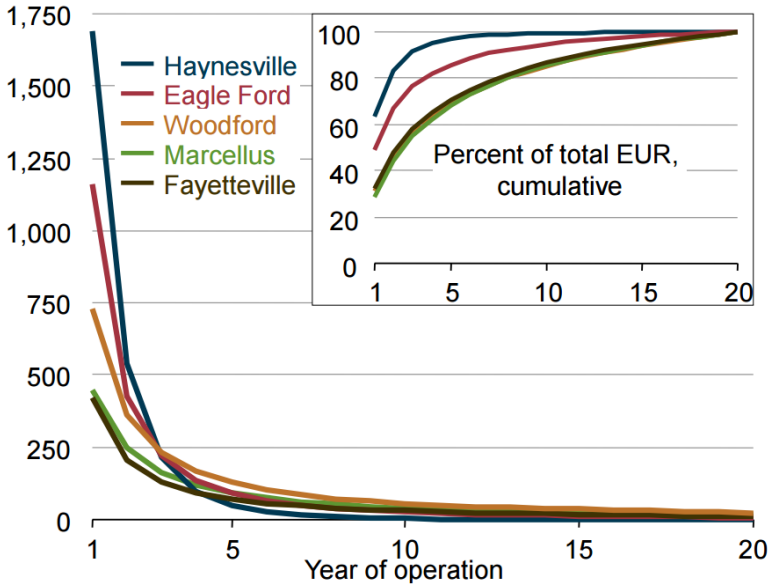

Figure 6. The sharp decline of shale gas through a well's life time, indicating the potential for tapping the adsorbed gas (Reprinted from Outlook, 2012).

According to IUPAC, based on the difference in size, nanopores can be subdivided into three categories: micropores (0.2-2nm) [1], mesopores (2-50nm), and macropores (>50nm). For ordinary fluid molecules related to oil and gas, in kerogen micropores, adsorption dominates; in kerogen macropores, free fluid dominates; in mesopores, both adsorption and free fluid are important (Kruk, Jaroniec, & Sayari, 1997). The size of the pores has an impact on both phase (Zottl & Stark, 2014) and transport (Arya, Chang, & Maginn, 2001) behavior of fluid in the pores. The pore size has huge impact on the thermodynamics, based on experimental results (Figure 7).

[1] For applications in petrophysics and geology, the term "micropore" sometimes refers to pores with diameters at the micrometer range.

Single file diffusion is an intuitive example (Figure 8) showing that different categories of pores can have unique impact on the fluid within.

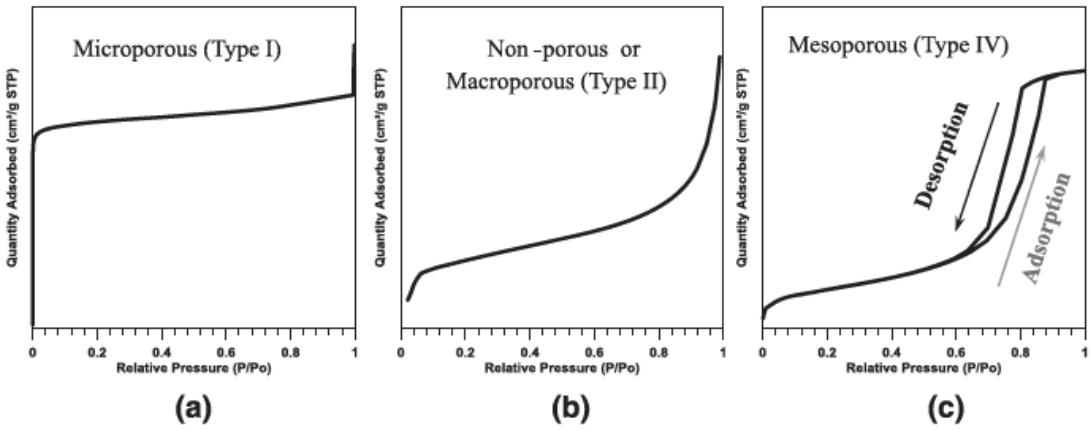

Figure 7. Typical isotherm shape exhibited by (a) purely microporous material (Type I, isotherm profile) (b) non-porous and microporous material (Type II, isotherm profile) and (c) purely mesoporous materials (Type IV, isotherm profile) (Reprinted from Donohue & Aranovich, 1998; Kuila & Prasad, 2013)

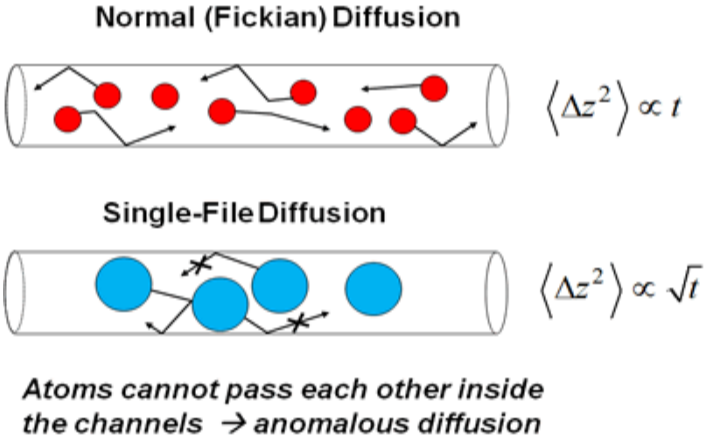

Figure 8. An illustration of single file diffusion: Micropores can only allow no more than one fluid molecule to pass through at a time, whereas mesopores allow multiple, resulting a difference in diffusivity (Reprinted from Cheng & Bowers, 2007)

Shale gas mainly contains methane (C1). And it may contain other hydrocarbons in significantly less amount, such as ethane (C2) and propane (C3). Hydrocarbons heavier than butane (C4) are usually very few. Non-hydrocarbon components such as CO_2 and N_2 sometimes exist (Bulba & Krouskop, 2009). As a result, in this research, we only analyze small hydrocarbon molecule up to C4.

Depending on its thermal maturity, that is the level of temperature the organic matter has been exposed to, kerogen consists of nanopores with a wide pore size distribution and large specific surface area for the storage of natural gas. The adsorbed gas amount in kerogen varies and makes up to 50% of gas in place (Ambrose, Hartman, Diaz Campos, Akkutlu, & Sondergeld, 2010). Thus, understanding the pore structure, petrophysical characteristics, and transport behavior of reservoir fluids in kerogen is of great importance. The kerogen microstructure and fluid it generates is highly impacted by the kerogen type (Figure 9). In Chapter III, we studied the fluid transport, and provided a simplified nanoporous network, in and for all four types of kerogen microstructures.

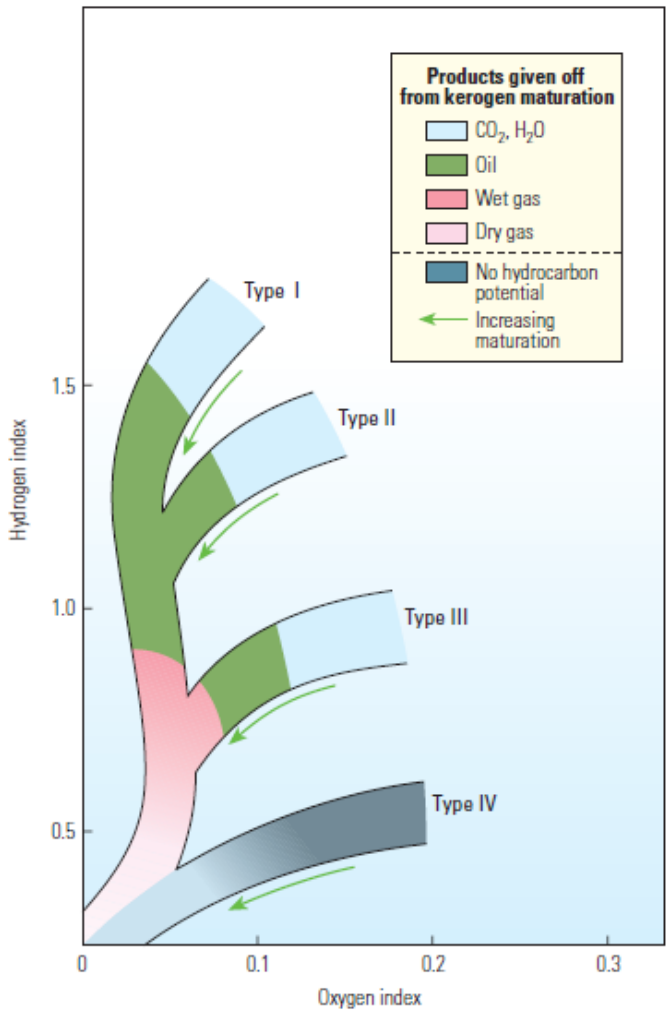

Figure 9. Modified Van Krevelen diagram showing the maturation pathways of kerogen upon burial and associated increase in temperature (Reprinted from McCarthy et al., 2011)

The study and characterization of pores in reservoir rocks has been a mature science for years. Figure 10 shows a range of pore throat sizes in typical siliciclastic rocks, and the corresponding characterization methods. When pore size goes under 10^{-2} μm, conventional methods for larger pores are no longer applicable and the characterization becomes more difficult, which calls for unique characterization technologies.

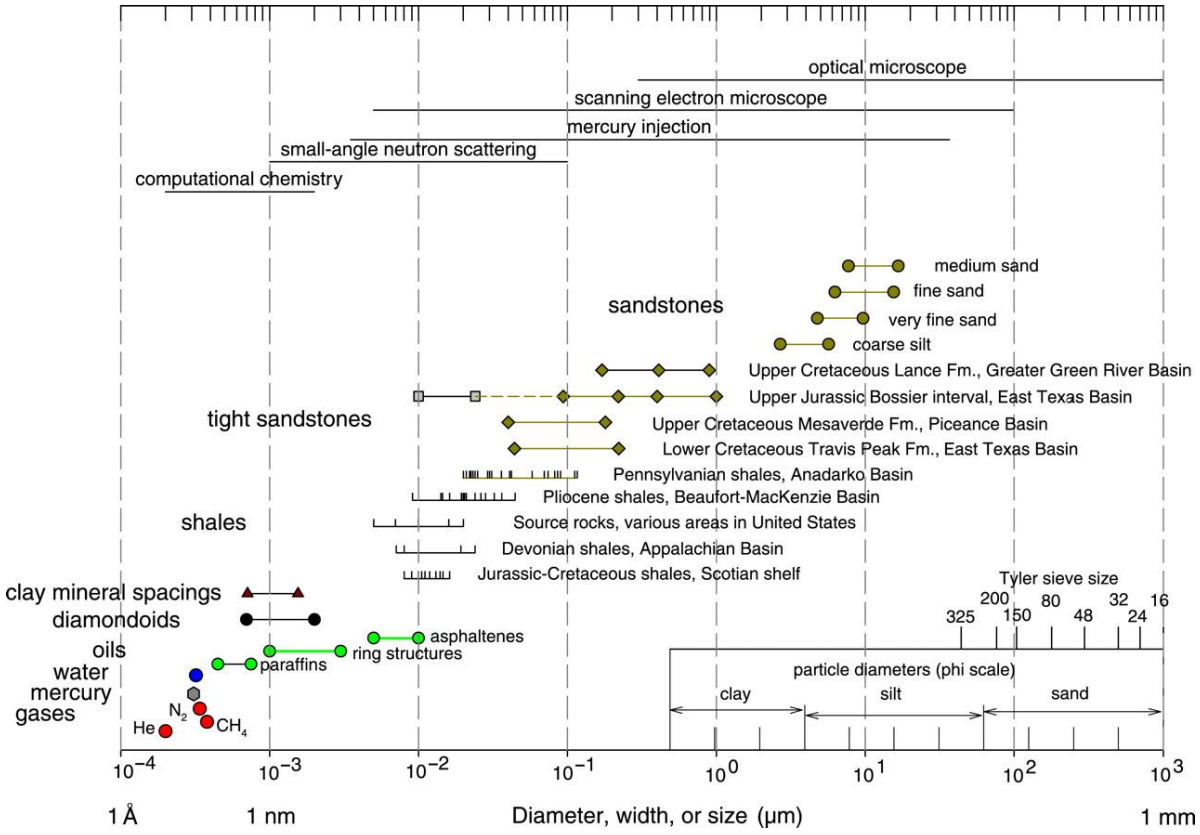

Figure 10. Pore throat sizes for typical siliciclastic rocks, with measurement methods, and molecular diameters of water, mercury, and three gases are also shown (Reprinted from Nelson, 2009).

The research on nanoporous materials and their physical phenomena is fast-evolving. To understand the elastic, storage and transport properties of shale gas, one challenge is to understand the complete pore structure, whereas the other is to understand how the pores interact with the fluid molecules.

To experimentally measure the pore size, shape and connectivity in shale gas samples, there are both direct and indirect methods. Direct methods include scanning electron microscopy (SEM), atomic force microscopy (AFM, Figure 11) (Chalmers, Bustin, & Power, 2012; Loucks, Reed, Ruppel, & Hammes, 2012) and transmission electron microscopy (TEM, Figure 12). Figure 13 gives a brief review on the applicability of each microscopic characterization method according to the length scale of the samples. We note that, nowadays, it is possible to get the 3-D imaging of material samples at the resolution <1 nm, which is the same as the diameter of typical atoms (Figure 19).

Indirect methods include pycnometry (Chalmers et al., 2012; Javadpour, Fisher, & Unsworth, 2007), nitrogen adsorption tests (Chalmers et al., 2012; Groen, Peffer, & Perez-Ramirez, 2003). Figure 14 shows the prevalent presence of micropores and mesopores in typical shale rock samples from adsorption tests. Figure 15 shows the basic setup of an indirect measurement. In addition, indirect methods requires some mathematical modeling to calculate the parameter being measured, as a result, the measurement results is highly sensitive to the accuracy of the model, and errors can be introduced during this process (Cui, Bustin, & Bustin, 2009; Q. H. Hu, Ewing, & Dultz, 2012; Mehmani, Prodanovic, & Javadpour, 2013). Specifically, permeability

measurement methods include pulse-decay method, canister desorption test, and measurement using crushed samples.

Direct methods can detect the geometric location of the pores in the sample, but the measurements are time-consuming; indirect methods can measure the pore-size distributions of the samples rapidly, but they cannot detect the location of the pores and cannot give the information how the pores are connected.

Another challenge for experimental measurement is sample preparation. For a highly heterogeneous reservoir rock, it is difficult to directly measure the contribution of flow of organic pores, and samples are prone to damage during the separation process. As a result, simulation methods can be considered very powerful alternative to experimental measurements.

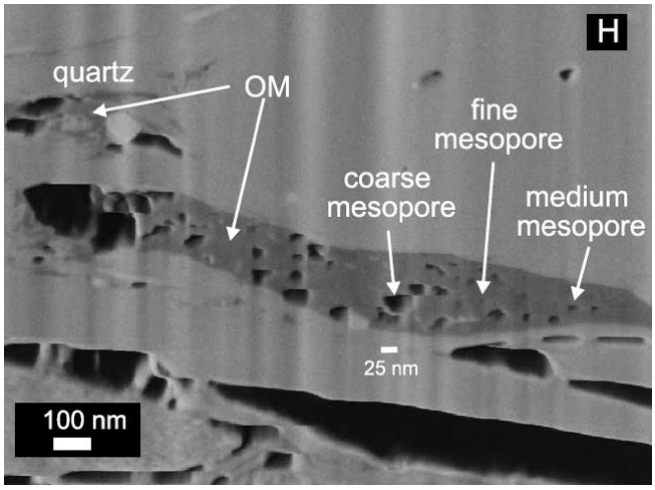

Figure 11. FIB/SEM image showing porosity and kerogen within shale. Black depicts pore, dark gray is kerogen, light gray is matrix (clay and silica) (Reprinted from Ambrose et al., 2010).

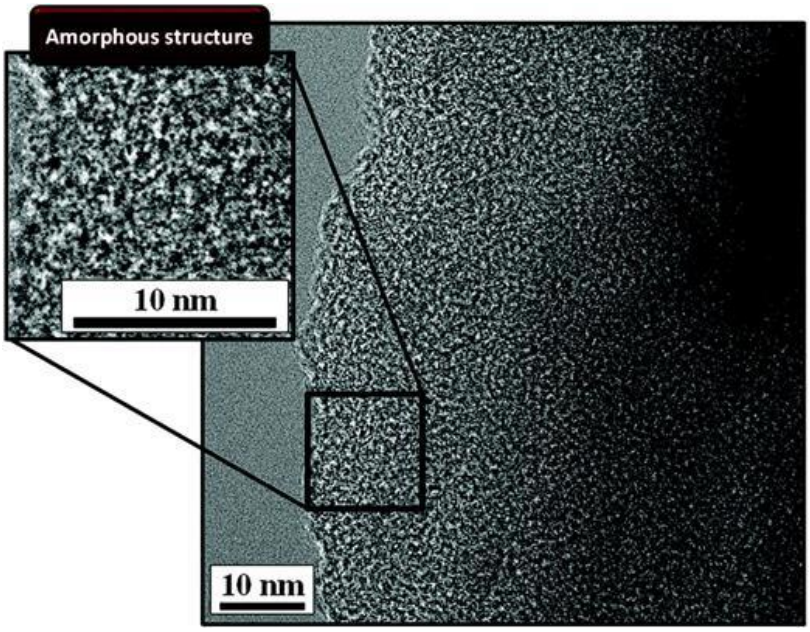

Figure 12. TEM image for an Eagle Ford kerogen sample (Reprinted from Firdaus & Heidari, 2015)

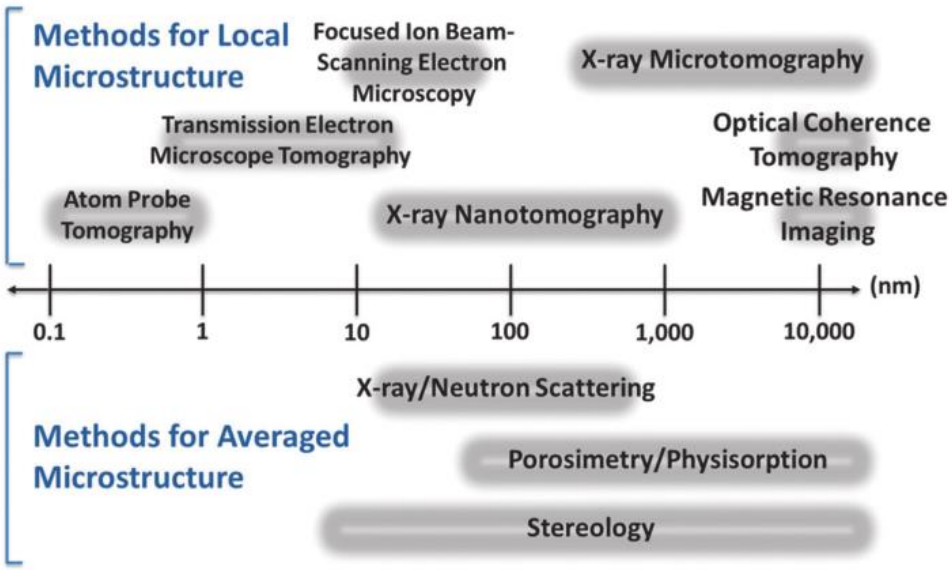

Figure 13. Overview of microscopic techniques. The resolution of each technique is displayed as an approximate range indicating its imaging capability (Reprinted from Cocco et al., 2013)

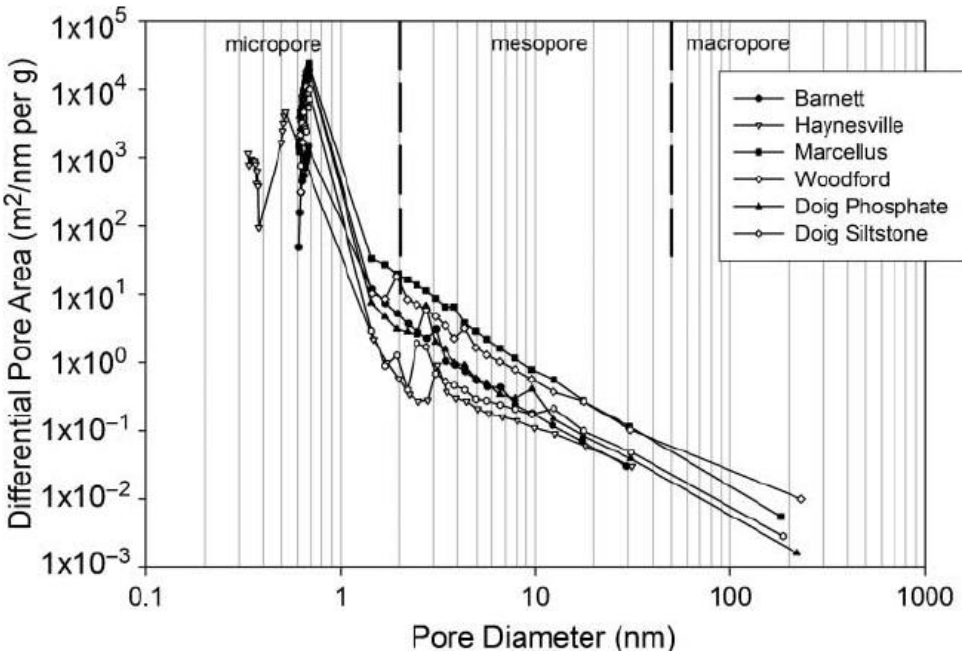

Figure 14. Pore-size distribution defined by differential pore volume using low-pressure gas (N_2 and CO_2) adsorption analyses (Reprinted from Chalmers et al., 2012)

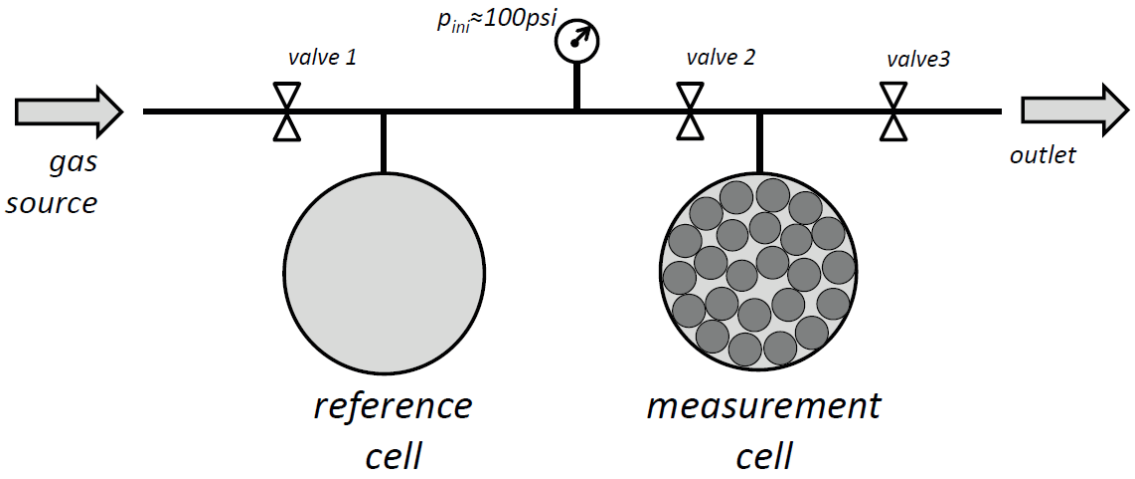

Figure 15. Laboratory measurement of low permeability unconventional gas reservoir rocks (Reprinted from Sander, Pan, & Connell, 2017)

The impact of pore size, shape and connectivity is the primary focus of this study. When pore size becomes small, there is deviation from conventional fluid dynamics. The first source of deviation from macropores is the significant contribution from adsorption. In many previous studies, the adsorption/desorption process is modeled as a diffusive process, and the dynamics can be described using diffusivities (L. Chen et al., 2015; Cui et al., 2009; Maginn, Bell, & Theodorou, 1993). This approach works relative well with micropores, in which the bulk fluid flow contribution can be ignored. However, in mesopores, the adsorption/desorption process is in parallel with bulk fluid flow, and it is reported that adsorbed molecules also contribute to the overall flow (Riewchotisakul, 2014).

The second source of deviation comes from confinement. This confinement effect can be described by Knudsen number (*Kn*). It is a dimensionless number defined as $Kn = \lambda/L$, which is the mean free path over the representative physical length scale, i.e. the pore size. When *Kn* gets large, the collision between fluid molecules and the confinement walls become non-negligible, and the fluid-wall interactions makes the transport phenomenon deviate from what is described by conventional fluid dynamics. The mean free path of molecules is impacted by pressure and temperature of the system, and the fluid molecule itself. Equation 1 describes the mean free path for ideal gas.

$$\lambda = \frac{k_B T}{\sqrt{2}\pi d^2 p} \qquad \textbf{Equation 1}$$

$$\frac{k_{app}}{k_0} = f(Kn, P) \qquad \textbf{Equation 2}$$

This effect is first reported by Klinkenberg (Klinkenberg, 1941). Previous numerical simulation results show that apparent permeability (the measured permeability considering Knudsen effect) is significantly dependent on pore throat size and pressure. With the decrease in reservoir pressure, slip flow, transition flow begins to dominate viscous flow (Brown, Dinardo, Cheng, & Sherwood, 1946; Javadpour, 2009; Klinkenberg, 1941). There are several models describing the Knudsen effect, however, the difference in apparent factors between the models can be huge, which indicates the uncertainty of the Knudsen effect (Figure 16, with flow regimes described in Table 1). This impact is crucial in determining the subsurface permeability, by making corrections to permeability measured in the lab, which typically has significant differences in pressure, temperature and fluid type than reservoirs.

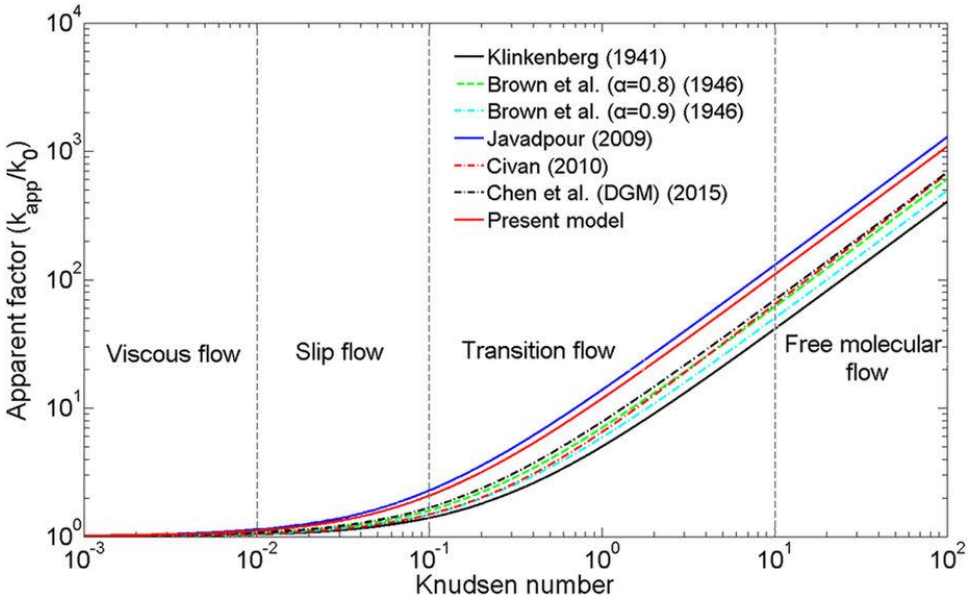

Figure 16. Comparisons of apparent permeability model ("α'' is the tangential momentum accommodation coefficient in Brown's model, reflect wall roughness) (Reprinted from Zhang, Hu, Meegoda, & Gao, 2015)

Table 1. Flow regime vs. Knudsen number

Flow regime	Knudsen number
Viscous flow	$<10^{-2}$
Slip flow	$(10^{-2}, 10^{-1})$
Transition flow	$(10^{-1}, 10^{1})$
Free molecular flow	$>10^{1}$

Forchheimer correction is another possible correction on Darcy's law, when the flow velocity is high (Re $\geq$ 10) (Whitaker, 1996). This effect is caused by the inertial accelerating or decelerating forces due to tortuosity, which introduces a non-linear term to the pressure ~ velocity relationship (Equation 3).

$$\nabla p = aU + bU^2 \qquad \textbf{Equation 3}$$

Multiscale transport and kinetics modeling is an approach to study transport behavior in unconventional reservoirs or rocks, and to predict the productivity of oil and gas (I. Yucel Akkutlu & Fathi; Fathi & Akkutlu; Fathi & Akkutlu, 2009; Fathi & Akkutlu, 2014; Wasaki & Akkutlu; Yi, Akkutlu, Karacan, & Clarkson, 2009). However, transport modeling and simulation requires accurate parameterization, especially those related to transport in nanopores and adsorption. Current novel reservoir simulation studies on highly heterogeneous reservoir rocks also require transport parameters of the nanopores to be determined to get more accurate results (Yan, Wang, & Killough, 2016).

There are several methods to simulate fluid flow in nanochannels, including molecular dynamics, direct simulation Monte Carlo (DSMC) (Oran, Oh, & Cybyk, 1998), dissipative particle dynamics (DPD) (Groot & Warren, 1997), Lattice-Boltzmann method (LBM) (S. Chen & Doolen, 1998; Raabe, 2004). Apart from molecular dynamics, which is the focus of this study, there are already many successful applications of these methods to study the transport phenomena in the shale gas reservoirs (L. Chen et al., 2015; Fathi & Akkutlu, 2013). Figure 17 suggests that the selection of the methods above, together with dynamics simulation methods based on Navier-Stokes equation, can be applied based on the size of the system, desired computational efficiency, Knudsen number, and the level of microscopic complexity.

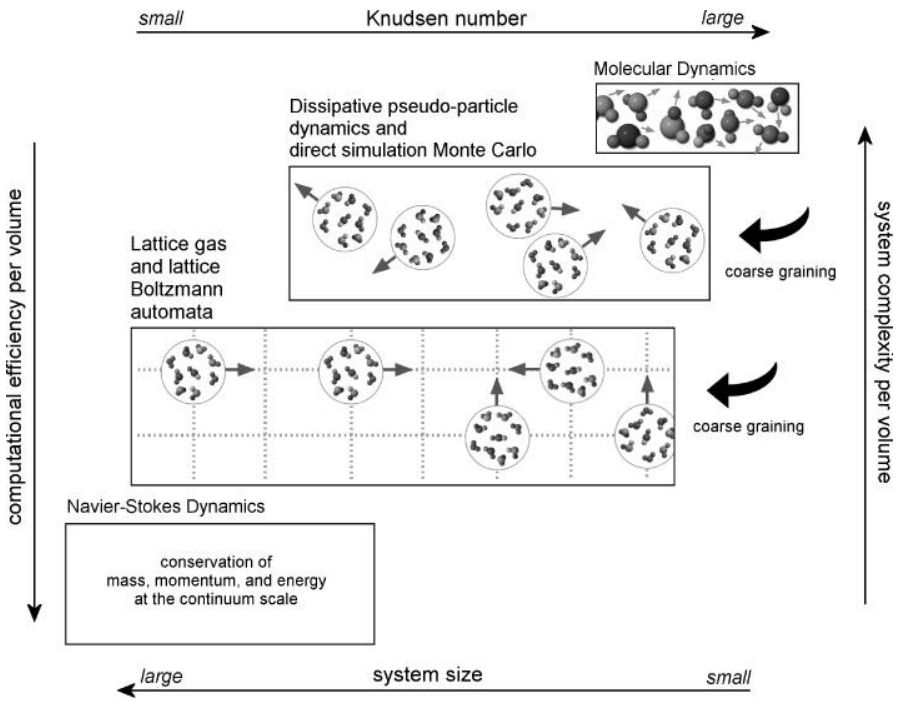

Figure 17. Various approaches to computational fluid dynamics together with their preferred range of applicability (Reprinted from Raabe, 2004)

Specifically, Lattice-Boltzmann method (lattice gas and lattice Boltzmann automata) is coarser than DPD and DSMC, instead of Navier-Stokes equations, it solves discrete Boltzmann equation with collision models (such as Bhatnagar–Gross–Krook). The direct simulation Monte Carlo (DSMC) uses Monte Carlo simulation to solve the Boltzmann equation (Equation 4, in the next section) with high Knudsen number. DSMC is commonly used for large and low-pressure systems. Because of its low computational cost, it is also used in simulation of transport in nanopores (Roy, Raju, Chuang, Cruden, & Meyyappan, 2003). Dissipative (pseudo-) particle dynamics (DPD) is a stochastic simulation method, which can avoid the lattice artifacts (exists in LBM) and saves significant computational cost than molecular dynamics and works very well for complex fluids (Espanol & Warren, 1995). Molecular dynamics simulation is by far the finest method used to simulate fluid flow. It not only considers all intra-atomic interactions, but also not possible to bypass the transient stage when it is used to simulate steady state behaviors. However, thanks to the rapid increase of computation power, molecular dynamics is becoming more and more popular. Molecular dynamics also makes model parameterization very easy. If the chemical structure of the system is accurately determined, the simulation results should be accurate.

There are already numerous modeling studies on the transport in porous media, specifically reservoir rocks, using the methods above, using idealized pore geometry and structures. These studies can be very useful in determining the impact of different variables, but since the idealized models are usually far away from the actual pore samples, the results cannot be directly used to accurately describe the

permeability/diffusivity in the porous media. As a result, finding ways to apply the numerical methods on accurate nanopore structures are crucial.

The application with a similar approach in macropores is a mature technology. The pore network models of conventional rocks such as sandstone (Blunt, 2001) is an tested application of Navier-Stokes dynamics in microporous media. Together with the sophisticated pore structure characterization method, engineers and scientists have created a new technology called digital rock physics for microporous media (Figure 18). The primary goal of digital rock physics studies is to relate measured geophysical observables to the in-situ rock properties. It includes in the analysis the shape and connectivity of the pores, which cannot be captured by the conventional macroscopic techniques such as porosimetry and NMR. The first necessary step for digital rock physics is to obtain a digital image of the porous material. This could be done using x-ray CT or micro-CT. Then, imaging artifacts are removed, and the separation between the solid material that makes up the skeleton and the pore space is performed for the investigations (Andra et al., 2013a). Finally, physical quantities of interest, for example, the permeability of the porous medium, can be computed considering steady-state flow throughout the pore network. Fluid flow for segments with large-scale pores is often simulated using Lattice-Boltzmann simulation method and the explicit jump Stokes method (Andra et al., 2013b).

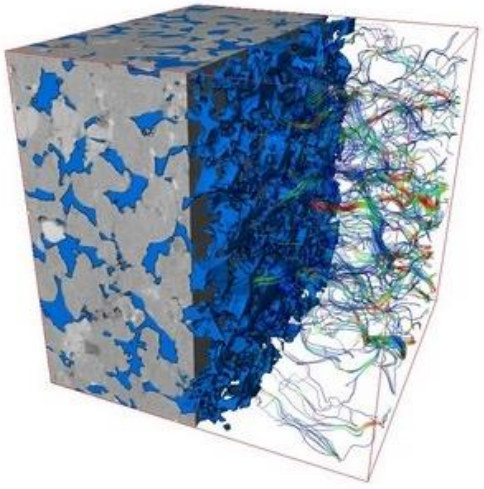

Figure 18. A graphical illustration of digital rock physics, from FEI (Reprinted from FEI, 2018)

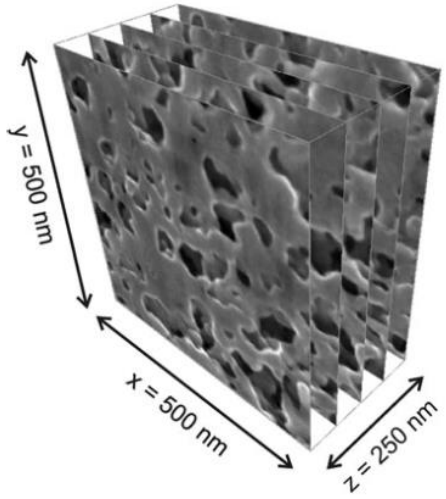

Figure 19. Stack of images produced with FIB-nt from sample, showing capability of high-resolution 3-D imaging (Reprinted from Balach, Soldera, Acevedo, Mucklich, & Barbero, 2013)

We are inspired to apply this methodology to smaller pores, to take the advantage of the advancement in simulation and characterization technologies. When pore size is reduced to the nanometer scale, the current imaging techniques, such as TEM, have a

sub-nanometer scale (0.1~0.2 nm) resolution which could capture the detailed 3-D images of the pores (Milliken & Curtis, 2016) (Figure 19). At this scale, the fluid-wall interactions are significant, hence, the chemical variability of the pore walls matters. However, the conventional approaches assuming homogeneous fluid properties such as the methods based on the Navier-Stokes equation and the Lattice-Boltzmann method may no longer be valid. Non-equilibrium molecular dynamics simulations could be used instead (Fathi & Akkutlu, 2013). The details will be covered in Chapter III.

Molecular Mechanics and Molecular Dynamics

Molecular modelling is the methodology that includes all theoretical and computational methods, to model or approximate the behavior of molecules, atoms and ions. This includes molecular mechanics, which treats atoms, ions or atomic groups as the smallest modelling unit; and quantum chemistry, which explicitly models the electrons.

Molecular mechanics relies on classical mechanics to model the behavior of the molecular systems, and the quantum effects are partially considered, by using different forms of model equations and parameters. In molecular mechanics, the Born-Oppenheimer approximation (Koppel, Domcke, & Cederbaum, 1984) is used, which assumes that the motion of atomic nuclei and the motion of the electrons in a molecule or ion can be treated separately. As a result, the potential energy of the entire molecular system can be calculated using the coordinates of the nuclei, with the impact of electrons implicit. Force fields, or interatomic potentials, are a series of functions (and their set of parameters) describing the interactions between atoms or coarse-grained particles within the molecular system, using the coordinates of atoms or particles as variables. The functions of force fields are determined empirically or theoretically; and the parameters of the force fields can be derived from experiments and/or quantum mechanical calculations.

The basic idea of molecular mechanics is illustrated in Figure 20, which requires statistical thermodynamics to combine the microscopic behavior to macroscopic properties. For processes that are not at thermodynamic equilibrium, non-equilibrium

statistical mechanics must be used to analyze the results from molecular mechanical simulations. The Boltzmann equation describes the statistical behaviors of systems that are not at non-equilibrium. The general form of Boltzmann equation can be written as Equation 4, with $f(\boldsymbol{r}, \boldsymbol{p}, t)$ being the probability density function of a state within the phase space, the "force" term corresponds to the influence of external forces, the "diffusion" term represents particle diffusion, and "collision" term represents the impact of particle collisions. The major challenge for solving this equation comes from the collision term. Bhatnagar, Gross and Krook (Bhatnagar, Gross, & Krook, 1954) proposed a simplification for the collision term (Equation 5), which maintains the accuracy in describing macroscopic behavior, being the theoretical foundation of molecular dynamics simulation (will be discussed later). In the Boltzmann equation, despite the “delta” in the phase space is selected to be infinitesimally small macroscopically, but the “delta” is still considered much larger than individual molecule. This implicit assumption also makes the analysis of molecular dynamics simulation valid. Another class of non-equilibrium statistical method applied in molecular mechanics is the perturbation from equilibrium (near-equilibrium methods), with tools includes Green-Kubo relations (Searles & Evans, 2000), Onsager reciprocal relations (Monroe & Newman, 2006), etc.

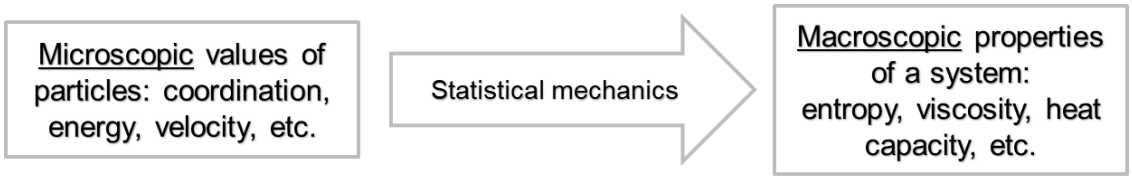

Figure 20. The basic idea of molecular modeling and simulation

$$\frac{df}{dt} = \left(\frac{\partial f}{\partial t}\right)_{force} + \left(\frac{\partial f}{\partial t}\right)_{diffusion} + \left(\frac{\partial f}{\partial t}\right)_{collision}$$ **Equation 4**

$$\Omega(f) = -\frac{1}{\tau}\left(f - f^{(0)}\right)$$ **Equation 5**

Since the simulation results must be analyzed using statistical thermodynamics, the simulation must be carried out under some certain restrictions to make the analysis valid, these restrictions are the same as those for statistical ensembles. An ensemble is like a probability distribution of a state of the system. There are three basic ensembles, and some certain thermodynamic quantities must be kept constant. Specifically, these are microcanonical ensemble (constant NVE ensemble), canonical ensemble (constant NVT ensemble) and grand canonical ensemble (constant μVT ensemble). Apart from these three ensembles, Gibbs ensemble (with constant NPT), and isenthalpic-isobaric ensemble (with constant NPH) are also commonly used in molecular mechanics.

To ensure that the entire molecular model fulfills the requirement of certain ensembles, some algorithms must be applied to adjust the trajectories (and/or velocities), other than the common molecular mechanical operations in a typical simulation cycle/step. Specifically, temperature and pressure are the two quantities which cannot be always kept constant during regular molecular simulation cycles/steps, thus "thermostats" and "barostats" can be applied to keep them constant. The common control methods include Nose-Hoover (Evans & Holian, 1985), Berendsen (Lemak & Balabaev, 1994), Langevin (Soddemann, Dunweg, & Kremer, 2003) and direct rescaling.

Typically, there are two ways to model a multi-atomic system, all-atom and united-atom. All-atom (AA) force fields treat each atom separately and assign parameters for every one of them; while the united-atom (UA) approach necessarily combine the impact of smaller atoms (e.g. hydrogen) into the impact of nearby larger atoms, which could reduce the degrees of freedom of the system and save computational cost, but at the risk of losing accuracy. Coarse-grained potential is a united-atom approach which further simplify the molecular model by combining more atoms together into larger grains, which could significantly reduce the computational cost, and widely used in long-time simulations of large molecular systems, such as proteins, DNAs and polymers.

The basic form for potential energy in molecular mechanics is shown in Equation 6. The classical force fields include: Assisted Model Building and Energy Refinement (AMBER) (Weiner & Kollman, 1981), Chemistry at HARvard Molecular Mechanics (CHARMM) (Brooks et al., 1983), Consistent Valence Force Field (CVFF) (Hwang, Stockfisch, & Hagler, 1994; Maple et al., 1994), GROningen MOlecular Simulation (GROMOS), Optimized Potential for Liquid Simulations (OPLS) (W. L. Jorgensen, Maxwell, & TiradoRives, 1996), Transferable Potentials for Phase Equilibria (TraPPE), Condensed-phase Optimized Molecular Potentials for Atomistic Simulation Studies (COMPASS) (Sun, 1998; Sun, Ren, & Fried, 1998; J. Yang, Ren, Tian, & Sun, 2000), PCFF (Sun, 1995; Sun, Mumby, Maple, & Hagler, 1994), PCFF+ (Collell, Ungerer, et al., 2014), and Universal Force Field (UFF) (Rappe, Casewit, Colwell, Goddard, & Skiff, 1992). The common force fields can be classified to Class I, Class II and Class III

force fields. The force field equation for Class I is shown in Equation 7, which uses harmonic terms to describe intramolecular interactions, and Lennard-Jones and Coulomb terms to describe intermolecular interactions; the Class II force field is built on top of the Class I force field, but added the secondary and tertiary interaction terms between bonds, angles, dihedrals, and improper dihedrals (Equation 8), and the conformational energies and vibrational spectra can be successfully predicted; the Class III force field is invented to overcome the limitations of the additive empirical force fields, including polarizable force fields, hybrid methods (QM/MM), and reactive force fields. In this study, the commonly used force fields for organic materials: OPLS, CVFF, PCFF and PCFF+ are used. A multi-body force field, Tersoff potential (Dodson, 1987), is used to model carbon nanotubes.

$$E_{total} = E_{bonded} + E_{nonbonded}$$
$$E_{bonded} = E_{bond} + E_{angle} + E_{dihedral} + E_{improper} \quad \textbf{Equation 6}$$
$$E_{nonbonded} = E_{electrostatic} + E_{van\ der\ Waals}$$

$$E_{total} = \sum_{bonds} k_b(b - b_0)^2 + \sum_{angles} k_\theta(\theta - \theta_0)^2 + \sum_{dihedrals} \frac{V_n}{2}(1 + \cos(n\phi - \delta)) + \sum_{impropers} k_\omega(\omega - \omega_0)^2 + \sum_{electrostatic} \left(\frac{q_i q_j}{\epsilon r_{ij}}\right) + \sum_{van\ der\ Waals} \epsilon_{ij}\left[\left(\frac{R_{min,ij}}{r_{ij}}\right)^{12} - 2\left(\frac{R_{min,ij}}{r_{ij}}\right)^{6}\right] \quad \textbf{Equation 7}$$

$$
\begin{aligned}
E_{total} = & \sum_{bonds} [k_{b.2}(b-b_0)^2 + k_{b.3}(b-b_0)^3 + k_{b.4}(b-b_0)^4] \\
& + \sum_{angles} \left[k_{\theta,2}(\theta-\theta_0)^2 + k_{\theta,3}(\theta-\theta_0)^2 + k_{\theta,4}(\theta-\theta_0)^2\right] \\
& + \sum_{dihedrals} \left[k_{\phi,1}(1-\cos\phi) + k_{\phi,2}(1-\cos 2\phi)\right. \\
& \left. + k_{\phi,3}(1-\cos 3\phi)\right] + \sum_{impropers} k_\chi \chi^2 \\
& + \sum_{bonds} \sum_{bonds'} k_{bb'}(b-b_0)(b'-b_0') \\
& + \sum_{angles} \sum_{angles'} k_{\theta\theta'}(\theta-\theta_0)(\theta'-\theta_0') \\
& + \sum_{bonds} \sum_{angles} k_{b\theta}(b-b_0)(\theta-\theta_0) \\
& + \sum_{bonds} \sum_{dihedrals} (b-b_0)\left[k_{\phi,b1}\cos\phi + k_{\phi,b2}\cos 2\phi\right. \\
& \left. + k_{\phi,b3}\cos 3\phi\right] \\
& + \sum_{bonds'} \sum_{dihedrals} (b'-b_0')\left[k_{\phi,b'1}\cos\phi + k_{\phi,b'2}\cos 2\phi\right. \\
& \left. + k_{\phi,b'3}\cos 3\phi\right] \\
& + \sum_{angles} \sum_{dihedrals} (\theta-\theta_0)\left[k_{\phi,\theta1}\cos\phi + k_{\phi,\theta2}\cos 2\phi\right. \\
& \left. + k_{\phi,\theta3}\cos 3\phi\right] \\
& + \sum_{angles} \sum_{angles'} \sum_{dihedrals} (\theta-\theta_0)(\theta'-\theta_0')cos\phi \\
& + \sum_{electrostatic} \left(\frac{q_i q_j}{\epsilon r_{ij}}\right) \\
& + \sum_{van\ der\ Waals} \epsilon_{ij}\left[\left(\frac{R_{min,ij}}{r_{ij}}\right)^{12} - 2\left(\frac{R_{min,ij}}{r_{ij}}\right)^{6}\right]
\end{aligned}
$$

Equation 8

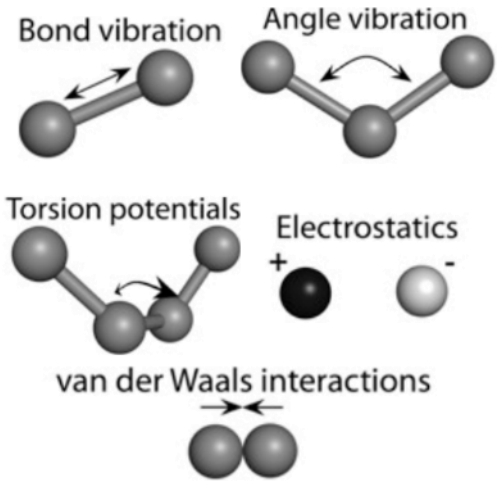

Figure 21. Common force field interactions

Lennard-Jones potential (Verlet, 1967) (Equation 9) is a simple model which approximates the van der Waals interaction between a pair of neutral atoms or molecules. For van der Waals interactions involving different types of atoms, a series of combination rules or mixing rules are applied. The Lorentz-Berthelot rules (Schoen & Hoheisel, 1984) (Equation 10) are the most commonly used among all of them.

$$U_{ij}^{LJ}(r_{ij}) = 4\epsilon_{ij}\left[\left(\frac{\sigma_{ij}}{r_{ij}}\right)^{12} - \left(\frac{\sigma_{ij}}{r_{ij}}\right)^{6}\right] \qquad \textbf{Equation 9}$$

With ϵ_{ij} and σ_{ij} being the energy and length scale of the interaction between two Lennard-Jones sites i and j, and r_{ij} is the distance between them.

$$\sigma_{ij} = \frac{\sigma_{ii} + \sigma_{jj}}{2}, \epsilon_{ij} = \sqrt{\epsilon_{ii}\epsilon_{jj}} \qquad \textbf{Equation 10}$$

Like van der Waals interaction, many interatomic forces decrease significantly with the increase in distance. As a result, to reduce computational cost, it is necessary to

ignore the interactions at longer distance by only considering the interaction within the Verlet list or cell list (Figure 22, Figure 23). For interactions which decay slowly (like electrostatic interaction), algorithms like Ewald summation (Hautman & Klein, 1992) and Particle Mesh Ewald (Darden, York, & Pedersen, 1993) is used to prevent accuracy loss while managing the computational cost.

Boundary condition is another important consideration for molecular mechanics. Unlike conventional mechanical modeling, molecular models are typically much smaller than the real systems to be investigated. In addition, it is generally considered not easy to make a fixed accurate boundary condition. As a result, periodic boundary condition is the most commonly used boundary condition for molecular mechanics (Figure 24).

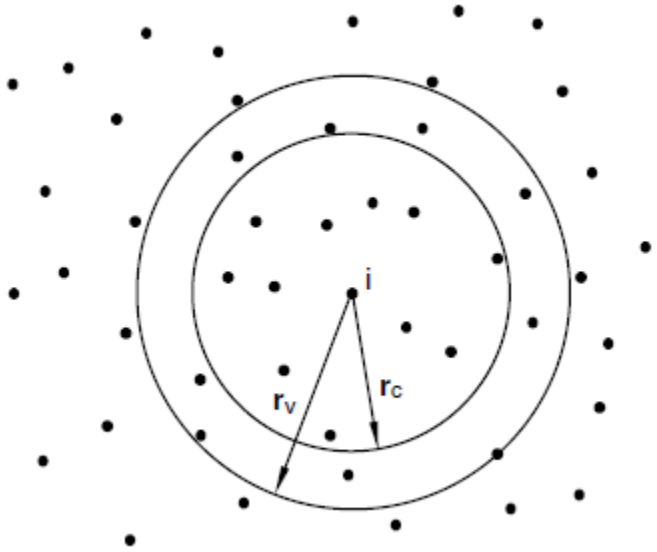

Figure 22. The Verlet list: a particle i interacts with those particles within the cutoff radius r_c; the Verlet list contains all the particles within a sphere with radius r_v (Reprinted from Frenkel & Smit, 2002)

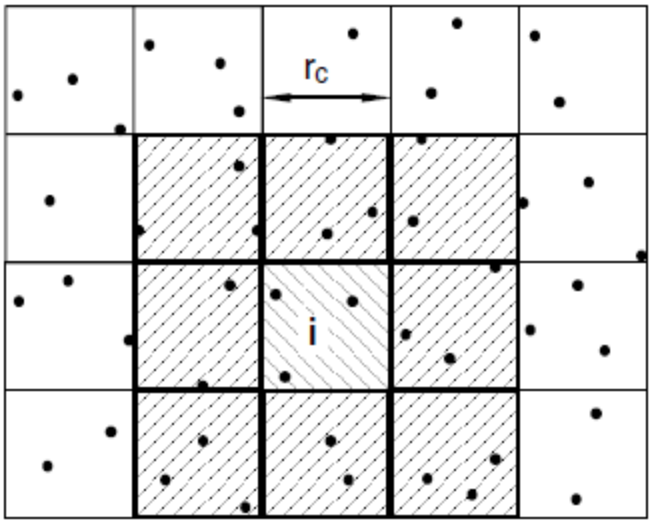

Figure 23. The cell list: the simulation cell is divided into cells of size $r_c \times r_c$ a particle i interacts with those particles in the same cell or neighboring cells (Reprinted from Frenkel & Smit, 2002)

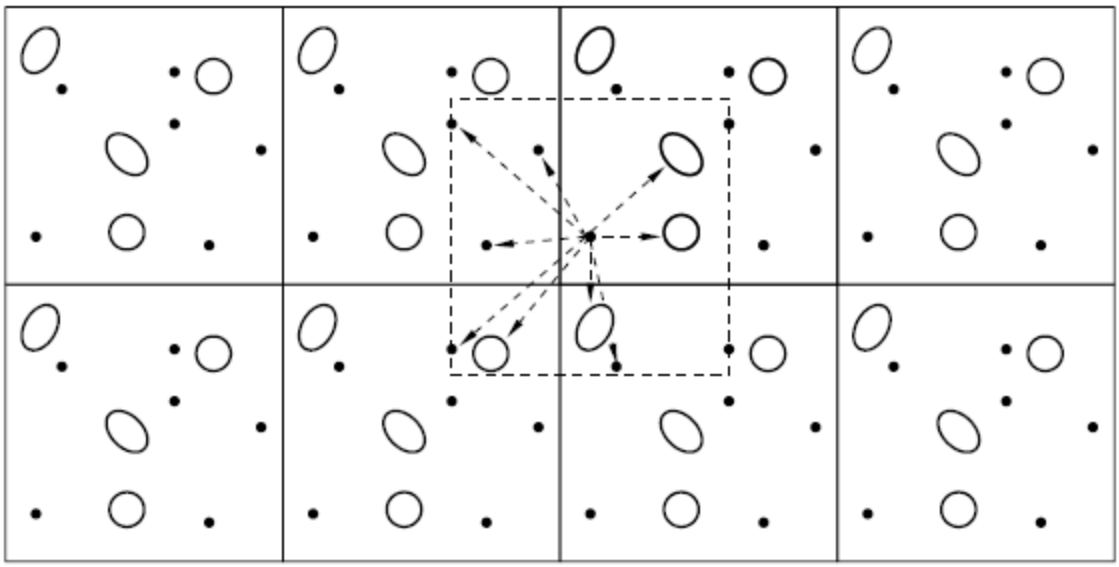

Figure 24. Schematic representation of periodic boundary conditions (Reprinted from Frenkel & Smit, 2002)

Molecular mechanics have certain limitations which could reduce its accuracy and even prevent it from generating valid results. These limitations include: 1) Reaction is not easy to be implemented; 2) Polarization needs special parameterization; 3) The parameterization of large molecules comes from analogies from small molecules, which could introduce errors. However, in this study, since there are no chemical reactions and the fluid molecules are not strongly polar, it can be expected that the accuracy loss only comes from the pore model.

Molecular mechanics is first mentioned by Andrews et al. (Kettering, Shutts, & Andrews, 1930), and the concept was proved by Allinger (Allinger, 1976), and further implemented in 1980s with the emergence of several popular force fields. Since 2000, there are more and more applications and publications about classical molecular mechanics simulations. Thanks to the fast development of high-performance parallel computing, molecular mechanics now can be utilized to study molecular systems with millions to billions of atoms, up to large biological systems and living cells (Perilla et al., 2015). And now it has been applied to investigate structure, dynamics, and properties of various subjects, including materials science, chemical biology, polymer chemistry, and so on.

Molecular dynamics is the main application of molecular mechanics. It uses force fields to calculate the forces between each interaction pairs, then with a proper integration algorithm and Newton's second law (Equation 11) of motion, the coordinates and velocities of all particles in the model are updated for the next time step. A typical molecular dynamics simulation cycle is shown in Figure 25, with the trajectory, forces,

and velocities being the main output. Using statistical mechanics, the macroscopic properties of interest can be calculated at the last step or on the fly. Other than the issues mentioned above, the entire molecular dynamics simulation requires some additional steps. The first is energy minimization. This process considers all the potential energy of the system without regard of the kinetic energy, and results in a local minimum and slight changes of the initial coordinates, to make the simulation more robust. Second, before the actual molecular dynamics production stage, the system shall go through a simulated annealing process, which further, and faster minimize the energy of the system.

$$\boldsymbol{F} = m\boldsymbol{a} \qquad \textbf{Equation 11}$$

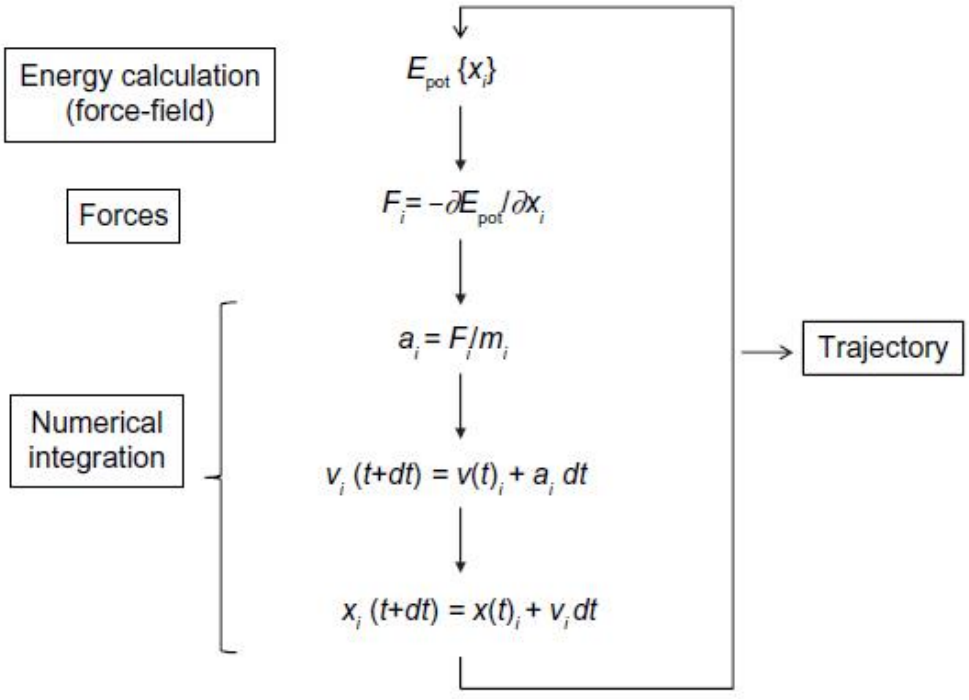

Figure 25. A typical cycle of molecular dynamics simulation (Reprinted from Hospital, Goñ i,Orozco, & Gelpí ,2015)

The molecular simulation work carried out in this study is performed using Large-scale Atomic/Molecular Massively Parallel Simulator (LAMMPS) (Plimpton, Crozier, & Thompson, 2007) is a molecular dynamics program from Sandia National Laboratories, which uses spatial-decomposition to partition the simulation into small sub-domains, which allows parallel computing in both CPUs and GPUs. GROMACS (Hess, Kutzner, van der Spoel, & Lindahl, 2008) is an alternative simulator which is used in the beginning of the project for ideation and comparison/validation purposes. VMD (Humphrey, Dalke, & Schulten, 1996) is a visualization software for molecular structure and modeling, and it is used for visualization in this study.

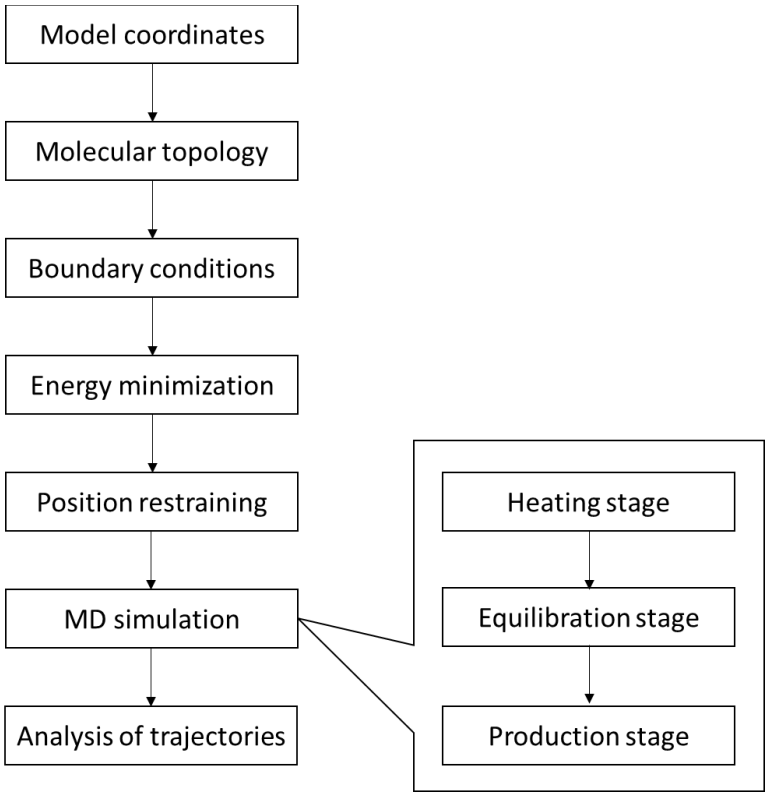

Figure 26. A typical workflow for molecular dynamics simulation

Molecular Monte Carlo simulation is another important application for molecular mechanics. Unlike molecular dynamics, it only considers the potential energy of the particles, without regard of the kinetic energy. However, based on the equipartition theorem, the kinetic energy per degree of freedom at equilibrium should be the same as potential energy per degree of freedom. The molecular Monte Carlo does not require integration of an equation of motion, thus the computational cost can be significantly reduced. And the thermodynamic properties of the system can be accurately determined. In this study, we use molecular Monte Carlo simulation to simulate the thermodynamic properties in equilibrium, such as density and adsorption capacity. Specifically, MCCCS Towhee (Martin, 2013) is used. Towhee is designed for the prediction of fluid equilibria with some solid/porous phases, using the Gibbs ensemble.

The Metropolis–Hastings algorithm (Chib & Greenberg, 1995), a Markov chain Monte Carlo method, is a key step in molecular Monte Carlo simulation. Since the total number of possible states in the phase space is enormous (because of the high dimension), it is not easy to arrive at a fair sampling using direct sampling. This method can be used to calculate the probability distribution or to compute an integral (thermodynamic property). The basic steps of the Metropolis–Hastings algorithm are as follows.

1) Randomly select particles and calculate the energy of the system.
2) Give the particles a random change in coordinates, then calculate the new energy of the system.

3) And then decide whether to accept the move or not based on the criterion:

$$\mathrm{acc}(\mathrm{o} \to \mathrm{n}) = \min(1, \exp\{-\beta(U_{new} - U_{old})\}) \quad \textbf{Equation 12}$$

After the sampling is completed, the thermodynamic quantities can be calculated based on statistical principles. Grand-canonical Monte Carlo (GCMC) is a widely used method to simulate thermodynamic equilibrium state, which relies on grand canonical ensemble. GCMC simulations are used in this study to construct adsorption systems at equilibrium.

The transport simulations using molecular dynamics has been extensively investigated. There are two common approaches to study fluid transport: equilibrium molecular dynamics (EMD) and non-equilibrium molecular dynamics (NEMD). Using EMD, it is possible to calculate the self-diffusivity of the fluid sample using the Einstein equation (Equation 13), and then calculate transport diffusivity or corrected diffusivity using the Darken equation (Equation 14). However, EMD is not suitable for calculating transport parameters for heterogeneous systems, and more samples are required to arrive at a stable D_0 (Maginn et al., 1993).

$$D_s = \frac{1}{6} \lim_{t \to \infty} \frac{d}{dt} \langle |\boldsymbol{r}(t) - \boldsymbol{r}(0)|^2 \rangle \quad \textbf{Equation 13}$$

$$D_t(c) = D_0(c) \left(\frac{\partial ln f}{\partial ln c} \right)_T$$

$$D_0 = \frac{1}{3N} \int_0^\infty \sum_{i=1}^{N} \sum_{j=1}^{N} \langle v_i(t') \cdot v_j(0) \rangle \quad \textbf{Equation 14}$$

when molecules rarely encounter each other, $D_0 = D_s$.

NEMD simulation has several different techniques. The first is gradient relaxation molecular dynamics (GRMD), which requires to setup a one-dimensional diffusion problem. GRMD is computationally intensive because the size of the system must be large enough to obtain a "continuum-like" behavior (Maginn et al., 1993). The other two commonly used methods includes external field nonequilibrium molecular dynamics (EF-NEMD) and dual-control volume grand canonical molecular dynamics (DCV-NEMD), which will be elaborated in Chapter II (Arya et al., 2001). Another method is to use a fluidized piston to provide a driving force (Itsuo Hanasaki & Akihiro Nakatani, 2006). This method cannot directly control the pressure gradient and has a maximum time limit on simulation. Previous research has utilized this method (Riewchotisakul, 2014), however, an "entry-effect" at the capillary throat presents, which makes it hard to tell the exact impact of the capillary walls.

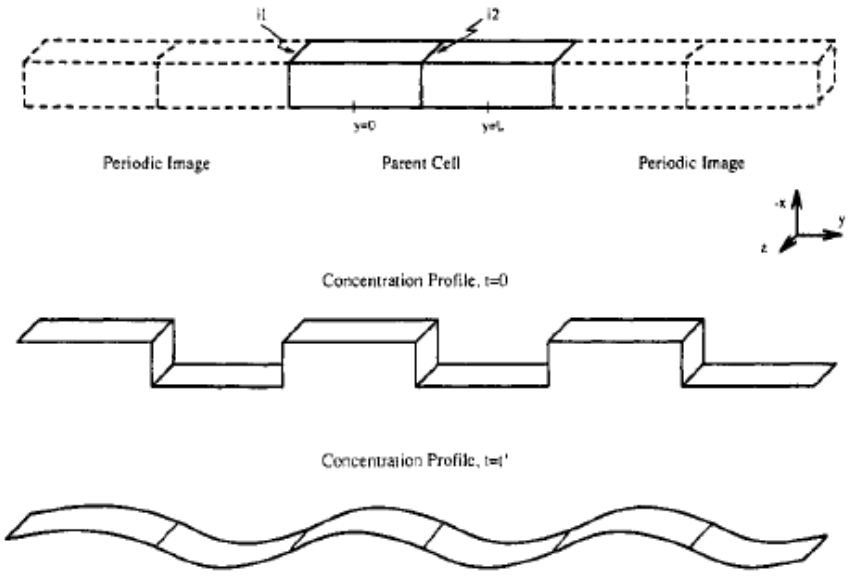

Figure 27. Schematic representation of the gradient relaxation MD simulation box, with periodic images shown along the direction of the concentration gradient (Reprinted from Maginn et al., 1993).

1-D nanochannel is a popular analogy for the study of nanopores using molecular dynamics simulation. Several studies has been done for the application in unconventional oil and gas (Firouzi & Wilcox, 2013; Frentrup, Avendaño, Horsch, Salih, & Müller, 2012; Z. Liang & H. L. Tsai, 2012; Mutat, Adler, & Sheintuch, 2012b; Riewchotisakul, 2014; Wu & Zhang, 2016). However, all of them failed to honor the real surface chemical structure of their capillary models, instead, the use of over-simplified capillary model may lead to spurious results.

Another approach is to build 3-D molecular models and using them run transport simulations. Before full chemistry kerogen models are invented, several porous carbon structures are used as analogies for organic porous media in unconventional reservoirs for molecular dynamics simulation (Cai, Buts, Seaton, & Biggs, 2008; Firouzi, Alnoaimi, Kovscek, & Wilcox, 2014; Firouzi, Rupp, Liu, & Wilcox, 2014; Firouzi & Wilcox, 2012; Mosher, He, Liu, Rupp, & Wilcox, 2013). Despite these results provide meaningful insights of the transport phenomena, failure to address the accurate chemical structure of the porous media makes it impossible for them to make accurate predictions. Afterwards, several consecutive studies have been done to construct accurate kerogen building blocks, based on lab characterization results of kerogen sample, including NMR, X-Ray photoelectron spectroscopy, vitrinite reflectance, and elemental analysis. Then, these models are used to construct microporous structures (
Figure 28), which are used to study thermodynamic and transport properties (Bousige et al., 2016; Collell, Galliero, et al., 2014; Collell et al., 2015; Collell, Ungerer, et al., 2014;

Falk, Coasne, Pellenq, Ulm, & Bocquet, 2015; Falk, Pellenq, Ulm, & Coasne, 2015; Ungerer, Collell, & Yiannourakou, 2015). However, these full chemistry models do not have direct control over the pore structure and connectivity, and mesopores are not yet been included. In Chapter III, we tried to overcome these drawbacks by introducing mesopores with controlled PSD; and provided a simplified molecular model which enables complete control over pore structures.

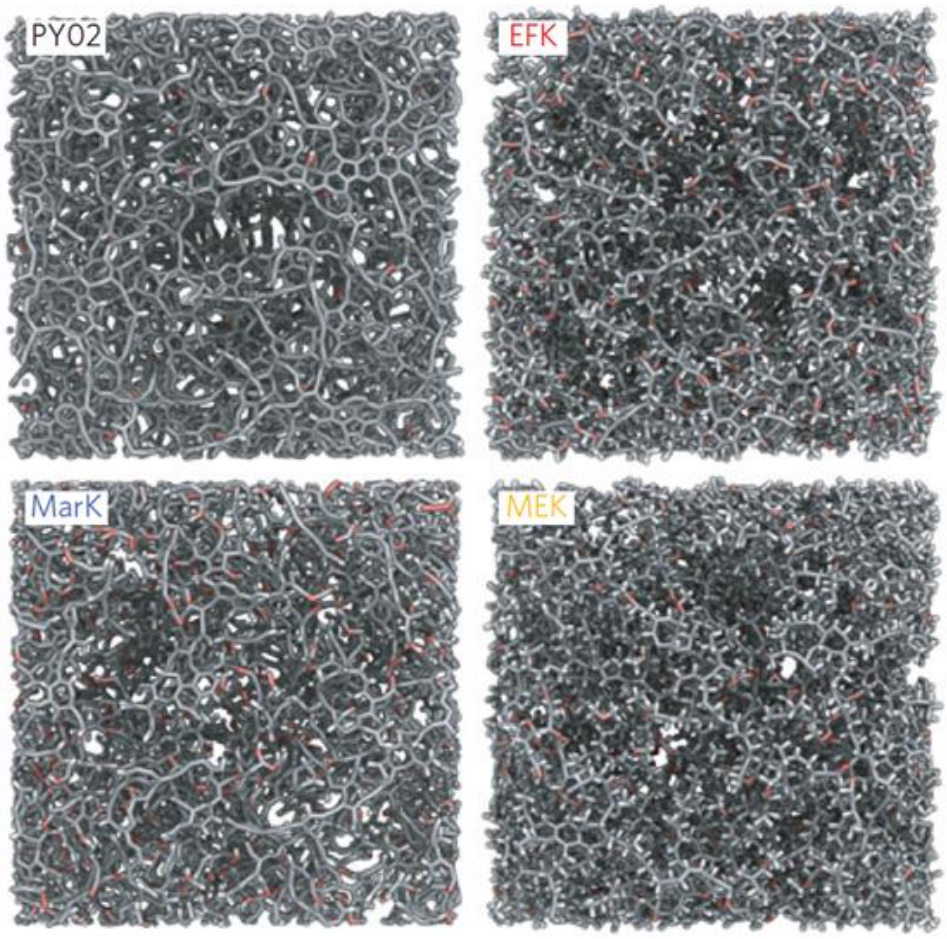

Figure 28. Realistic molecular model for kerogen, with micropores only (Reprinted from Bousige et al., 2016)

CHAPTER II

MODELING AND SIMULATION OF 1-D NANOCAPILLARY*

In this molecular mechanics simulation study, we first use 1-D nanochannel as the most simplified case to study the general relationship of transport in mesopores, then we construct 3-D realistic pore network models to mimic the transport of fluid molecules in real kerogen samples.

Model Description

Shale gas production involves fluid transport from nanoscale capillaries where the fluid flow may be affected by the capillary walls. In small nanocapillaries, the walls have the potential to influence the flow through microscopic parameters, such as fluid-wall molecular attractive forces and binding energy. These quantities are not considered in the classical fluid mechanics calculations. Thus, a deep understanding of the fluid transport in nanocapillaries could be critical for a better interpretation of the shale gas production. Conventional reservoir engineering methods rely on Hagen-Poiseuille equation of laminar flow, which is built on the assumption that the flow velocity by the capillary walls is negligible, i.e., no-flow boundary condition. There exists viscous coupling in the fluid,

* Part of this chapter is reprinted with permission from "Flow of hydrocarbons in nanocapillary: A non-equilibrium molecular dynamics study." by F. Feng, I. Yucel Akkutlu, *SPE Asia Pacific Unconventional Resources Conference and Exhibition.* Society of Petroleum Engineers, 2015.

which dictates a parabolic velocity profile for the flow (Figure 29). Superficially, for a cylindrical capillary, we have Equation 15, where $v_z(r)$ is the streaming velocity along the flow direction.

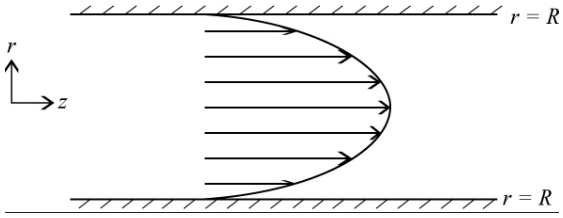

Figure 29. Illustration of velocity profile inside a cylindrical capillary, with assumption that $v_z(R) = 0$. Reprinted with permission from Society of Petroleum Engineers, Copyright 2015.

$$v_z(r) = -\frac{1}{4\mu}\frac{dp}{dz}(R^2 - r^2) + v_z(r = R) \qquad \textbf{Equation 15}$$

Based on the assumption of no-flow boundary condition, we have the foundation of the Darcy's law:

$$v_z(r = R) = 0 \qquad \textbf{Equation 16}$$

$$v_z(r) = -\frac{1}{4\mu}\frac{dp}{dz}(R^2 - r^2) \qquad \textbf{Equation 17}$$

This assumption is valid for large capillaries, where the velocity of the fluid at the center of the capillary is large such that $v_z(r = 0) \gg v_z(r = R)$. However, for small capillaries this velocity becomes significantly reduced, where $v_z(r = R)$ is comparable to $v_z(r = 0)$; then, no-flow boundary assumption needs to be re-visited.

With the non-zero velocity near the capillary walls, the mass flux at or near the walls may have a significant contribution to the overall hydrocarbon transport. As a result, permeability of nanocapillaries would be not only a function of pore size, but also a

function of the pore wall properties, such as surface roughness and heterogeneities in surface chemistry. In oil-wet structures, such as in the case of the kerogen pore network with large pore wall surface area, the number of adsorbed molecules is not trivial compared to the total amount of hydrocarbons in place. Then, how would the flow field in these structures appear? Would the capillary walls influence the flow to a scale that one could observe significant non-Darcy effects?

It has previously been discussed by several authors that mass transport in nanocapillary mainly consists of four mechanisms: a) Knudsen diffusion, b) molecular diffusion, c) surface diffusion, and d) convection (Albo, Broadbelt, & Snurr, 2006). In high pressure cases, such as shale gas reservoirs conditions, the contribution of Knudsen diffusion is relatively small compared to the other mechanisms; hence it could be safely neglected. Molecular diffusion, on the other hand, does not contribute in the single-component gas cases. Then, considering the presence of convection and surface transport only, one would write the total velocity as follows:

$$v_z(r) = v_{z,H-P}(r) + v_{z,surface} \qquad \textbf{Equation 18}$$

$$q_{total} = q_{H-P} + q_{surface} = q_{H-P} + \int_0^R \rho(r) v_{z,surface} r dr \qquad \textbf{Equation 19}$$

Here, note that the surface contribution of the pore walls on the flow rate is an integral in the radial direction. Albo et al. (2006) and several other authors introduced the surface transport as an activated process and its diffusivity can be described with the Arrhenius form. However, real capillaries are not perfectly smooth, which make previous conclusion dubious and requires further investigation. For the overall gas transport

experiencing only the pressure gradient as the driving force, the total flow rate can be simply adjusted by adding a surface flow term.

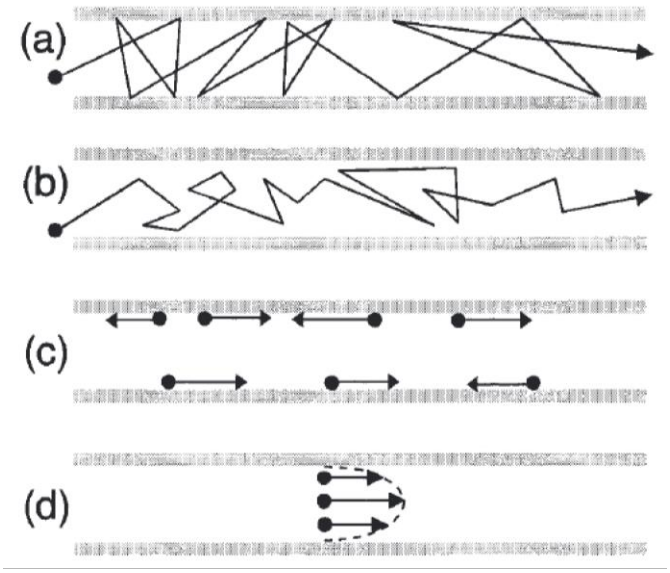

Figure 30. Previously proposed mass transport mechanisms in nanocapillaries (Reprinted from Albo et al., 2006).

Fundamentally, true driving force on the mass transport is the chemical potential gradient. The transport of guest molecules confined in nanocapillaries is common in systems such as catalysts, membranes and porous separators. Both experimental and theoretical work has been done to study this phenomenon (Kärger & Ruthven, 1992; Maginn et al., 1993; Xiao & Wei, 1992). Diffusive transport can be described by the generalized Fick's law, which is a linear combination of chemical potential gradients for multi-components:

$$J_i = -c_t \sum_{i=1}^{n-1} D_{ij} \nabla x_j \qquad \textbf{Equation 20}$$

in which D_{ij} is Fickian diffusivity, or simply diffusivity, and depends on concentration but not the magnitude of the gradient (Taylor, 1993). For the single-component fluid case, the relationship can be written as

$$J = -\frac{L(c)}{k_B T} \nabla \mu \qquad \textbf{Equation 21}$$

where $L(c)$ is the single-component transport coefficient (Arya et al., 2001). This model has been validated for cases involving various porous media (Kapteijn, Bakker, Zheng, Poppe, & Moulijn, 1995; Krishna, 2000) (Maginn et al., 1993) and the diffusivity can be derived from the transport coefficient.

Based on statistical mechanics, connecting microscopic values of particles and macroscopic properties of a system, molecular dynamics (MD) simulation and molecular Monte Carlo (MC) simulation have been widely used to study equilibrium and non-equilibrium thermodynamic properties.

Equilibrium and non-equilibrium MD simulations can both be used to calculate diffusivities. In equilibrium MD simulation method, L and D_t can be calculated from Green-Kubo relation (Theodorou, Snurr, & Bell, 1996):

$$L = \frac{V}{3} \int_0^\infty dt' < \boldsymbol{J}(t') \cdot \boldsymbol{J}(0) > \qquad \textbf{Equation 22}$$

$$D_t = \frac{1}{3N}\left(\int_0^{\infty} dt' < \sum_{i=1}^{N} \boldsymbol{v_i}(t') \sum_{j=1}^{N} \boldsymbol{v_j}(0) > \right)\left(\frac{\partial lnf}{\partial lnc}\right)_T \qquad \textbf{Equation 23}$$

where f is fugacity and N is the number of molecules. No driving force (chemical potential gradient) is applied externally. The thermodynamic factor term $\left(\frac{\partial lnf}{\partial lnc}\right)_T$ must be calculated with other methods to get transport diffusivity (X. Liu et al., 2012; X. Liu et al., 2011). For multi-component case, similar equations apply. Theodorou et al. (1996) also proposed so-called gradient-relaxation MD simulation based on transient flow simulation (Maginn et al., 1993). However, due to the unstable nature of transient flow, this simulation method is not widely used.

The most commonly used methods to simulate mass transport and calculate transport diffusivities are homogeneous molecular dynamics, or external field non-equilibrium molecular dynamics (EF-NEMD), and inhomogeneous molecular dynamics methods, or boundary driven molecular dynamics.

In EF-NEMD method, the chemical potential gradient $-\nabla\mu$ is replaced by an external force term f, to mimic the chemical potential gradient, which is identical to imposing a pressure gradient or concentration gradient to the fluid system. The simulation box of this method is relatively easy to setup, and it is faster than the inhomogeneous methods (Maginn et al., 1993). Modifications can be made to this method, by only applying external force field on a segment of the simulation box, to allow simulation for more complex porous media (Z. Liang & H.-L. Tsai, 2012). In this work, EF-NEMD

method is used primarily and inhomogeneous method is only used to verify the simulation results.

In boundary driven non-equilibrium molecular dynamics, two reservoirs with high and low concentrations are constructed to apply driving force on the opposite sides of the flow region. Usually, Grand Canonical Monte Carlo (GCMC) techniques are used on the two reservoir tanks to maintain constant pressure and constant driving force, which is called Dual Control Volume Grand Canonical Molecular Dynamics (DCV-GCMD). The concept of this method is more intuitive than EF-NEMD method; however, it requires larger simulation system and longer simulation time. Thus, it is more suitable to simulate fluid flow through membrane systems (Lin & Murad, 2001). This method not only allows the study of both linear and non-linear responses, but also allows the simulation study for non-regular shaped porous media (Arya et al., 2001; Heffelfinger & Swol, 1994). The near-equilibrium approximation of irreversible thermodynamics, which stipulates the linear relationship between diffusive flux and the chemical potential gradient, is often disrupted by real or artificial momentum transfer. Also, this method may lead to severely underestimated fluxes, or additional mass transfer resistance, if not used properly (Lin & Murad, 2001). Instead of using GCMC simulation periodically to keep a constant driving force, some researchers choose to use two large enough reservoirs so that in the short simulation time, the change in chemical potential difference can be negligible (L. Wang, 2012). The conversion of external force and pressure gradient can be determined by the relationship between chemical potential vs. pressure, to determine chemical potential

gradient at a certain pressure gradient, and external force equals chemical potential gradient.

Carbon nanotube is a typical analog for the representation of the nanoscale capillaries of kerogen, based on which, critical parameters such as the pore size, pore wall roughness, and the strength of the liquid-wall interactions, can be modified and studied. In this work, single-wall carbon nanotubes made of a graphene sheet with inner diameters varying from 3nm to 9nm are used. Graphene represents the ultimate maturation in source rocks and has uniform surface properties. Graphene wall roughness can be modified relatively easily to mimic the roughness on the pore wall surfaces. The fluid flow inside the nanocapillary has been investigated for other applications such as nano- and micro-fluidics, however, these were far away for the subsurface conditions. In addition, for the shale oil/gas production, the shapes of the capillaries are not of regular shapes, and the fluids are multi-component hydrocarbons, which are foundationally different from the previous investigations. Hence, the research on the unconventional shale oil/gas production is still at an infancy stage.

Flow Simulations

In this study the fluid flow is simulated using both EF-NEMD and DCV-GCMD. These are thermodynamic non-equilibrium molecular simulation methods. The simulation box is mainly composed of a 25nm long straight carbon nanotube, with varying diameter. In EF-NEMD method, the simulation is set with periodic boundary condition that is applied on both sides perpendicular to the flow direction, with a constant external force applied on every molecule, and the strength of the external force is assigned to a corresponding pressure gradient. In DCV-GCMD method, the simulation box consists of three regions, upstream (5nm long), midstream (15nm long) and downstream (5nm long), with GCMC simulations to control the upstream and downstream pressures, by setting the corresponding chemical potentials and temperatures, to drive net flow from upstream to downstream regions (Figure 31, Figure 32). The movement of the carbon atoms of the nanotube wall can be either fixed or allowed to vibrate. In the latter case, the carbon atoms within 2nm to the boundary of the simulation box are fixed to ensure that the movement of the carbon nanotube is confined.

Prior to molecular dynamics simulation, the carbon nanotubes are charged to the desired temperature and pressure using GCMC simulation, more details are given in the Appendix. During the MD simulation, Nosé–Hoover thermostat is applied to the whole simulation system to ensure that the simulation is performed under the constant pressure

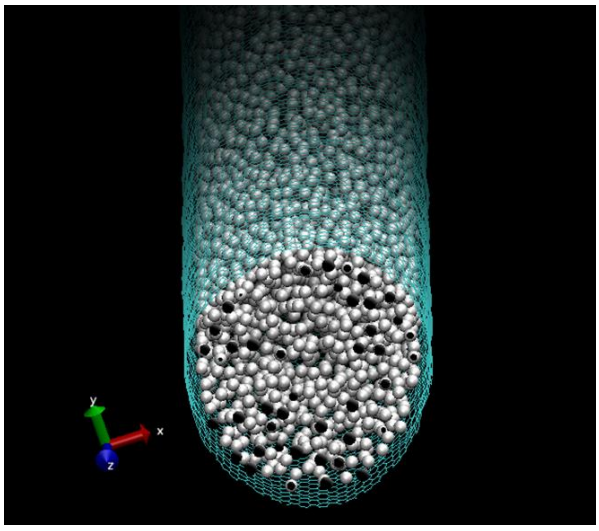

Figure 31. An illustration of methane charged in a smooth carbon nanotube: metallic colored balls are methane molecules, cyan skeleton is the carbon nanotube made of graphene sheet, diameter = 5nm. Reprinted with permission from Society of Petroleum Engineers, Copyright 2015.

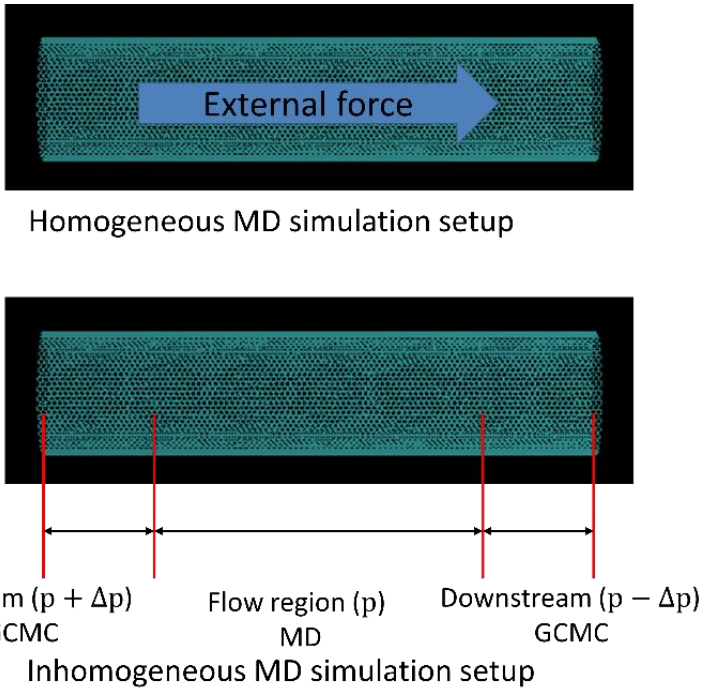

Figure 32. Simulation setup for homogeneous molecular dynamics (top) and inhomogeneous molecular dynamics (bottom) simulations. Fluid molecules are not shown. Reprinted with permission from Society of Petroleum Engineers, Copyright 2015.

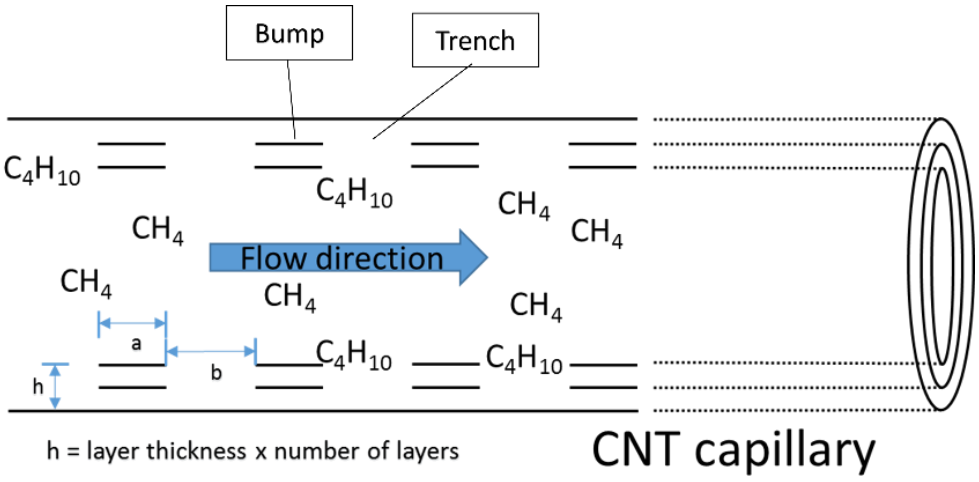

Figure 33. Simulation setup for molecular dynamics simulation of binary mixture in nanocapillary with rough surface. Reprinted with permission from Society of Petroleum Engineers, Copyright 2015.

and temperature. The temperature is set to a value varying from 86 F to 356 F, the pressure, on the other hand, is set to a value varying from 1000 psia to 12000 psia. The diameter of the tube is set to a value varying from 3 nm to 9 nm. During the MD simulations, the pressure gradient is set to a value between 1 to 100 psi/nm. Although the pressure gradient is large, due to the small capillary diameter, the flow is kept laminar, so the results obtained can be reasonably extrapolated to lower pressure gradients. Although using smaller pressure gradient may be perceived as real and a lot more meaningful, here we should note that the simulation takes longer, and the results have higher level of uncertainty due to a significantly smaller number of molecules, which leads to large fluctuations in the velocity field. In addition, under the imposed conditions, no Knudsen flow effect is expected due to high fluid density.

In addition to the single-component flow simulation in smooth capillaries, multi-component fluid flow simulations and simulations involving capillaries with rough

surfaces are performed, See Figure 33. In the latter case, the segmented, multi-layered smaller carbon nanotube rings can be placed inside the original carbon nanotube to mimic the roughness on the tube walls. The heavier component of the fluid which has more tendency to be adsorbed to the wall are more likely to be trapped by the trenches inside the tube. Realistic sizes of bumps and trenches (*a*, *b*, and *h* values) are used, to match the sizes of the most common chemical functional groups in real kerogen nanocapillaries. Figure 34 shows a snapshot of methane transport in nanocapillary with rough surfaces.

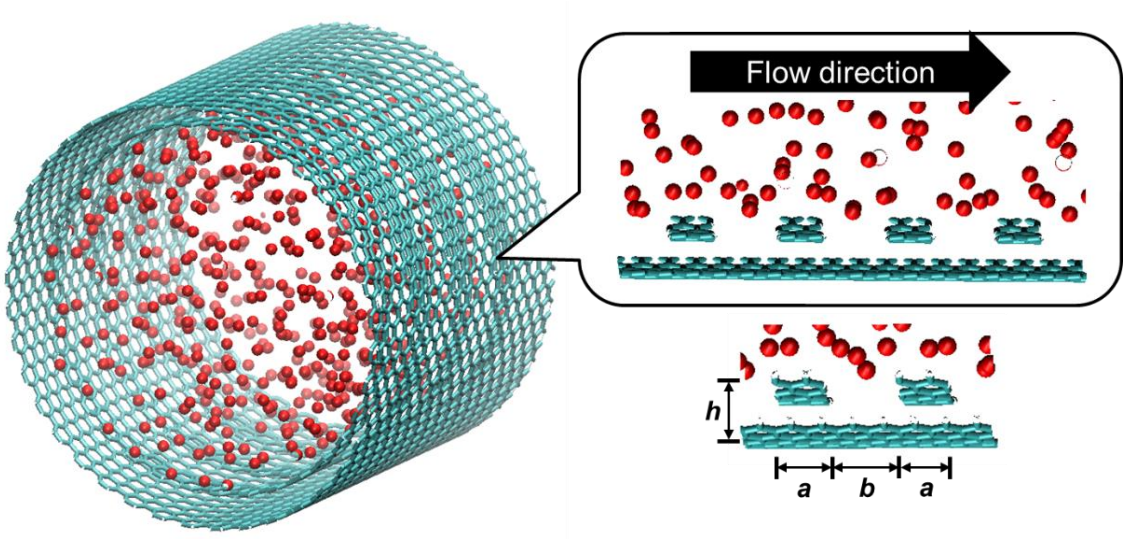

Figure 34. The structure of a capillary with a rough inner surface, built with carbon nanotube walls (Cyan skeleton), filled with methane (red) (Feng & Akkutlu, 2015) a, b and h are parameters describing the roughness of the capillaries. Reprinted with permission from Society of Petroleum Engineers, Copyright 2015.

Results

First, we performed equilibrium simulations to charge the capillary with the fluid. GCMC simulation is used for this purpose. The obtained fluid mass density profiles across the radius of the capillary are shown in Figure 35. The figure also contains the methane bulk density value at the same pressure and temperature conditions as the dotted line. Note that the adsorption layer is somewhat sensitive to the pressure, although its value does not vary significantly at high pressures. This is because the adsorption layer has fully developed at these high pressures. The second layer of high density by the wall, here we are going to call it transition layer following the terminology given in Rahmani and Akkutlu (2013), could be perceived as the deviation from the Langmuir theory, and it indicates that the adsorption is taking place under equilibrium, i.e., constant release and adsorption of methane molecules. Note that, with the increase in pressure, the density of the central layers by the carbon nanotube wall increases significantly, indicating that more methane molecules are stored at the central portion of the capillary as a compressed free fluid.

Next, we consider the flow of methane inside the nanocapillary under steady-state conditions using EF-NEMD. In Figure 36, the actual streaming velocity profile (in blue) is shown along with the Hagen-Poiseuille velocity (in dotted red), with the no-flow boundary condition. Notice that the molecular simulation gives a higher velocity. In addition, we record non-zero velocity values at the wall. This could be perceived at the first sight as decoupling of viscosity and a transition from convection to diffusion but it is clear that the parabolic nature of the velocity profile still prevails. Hence, convection is

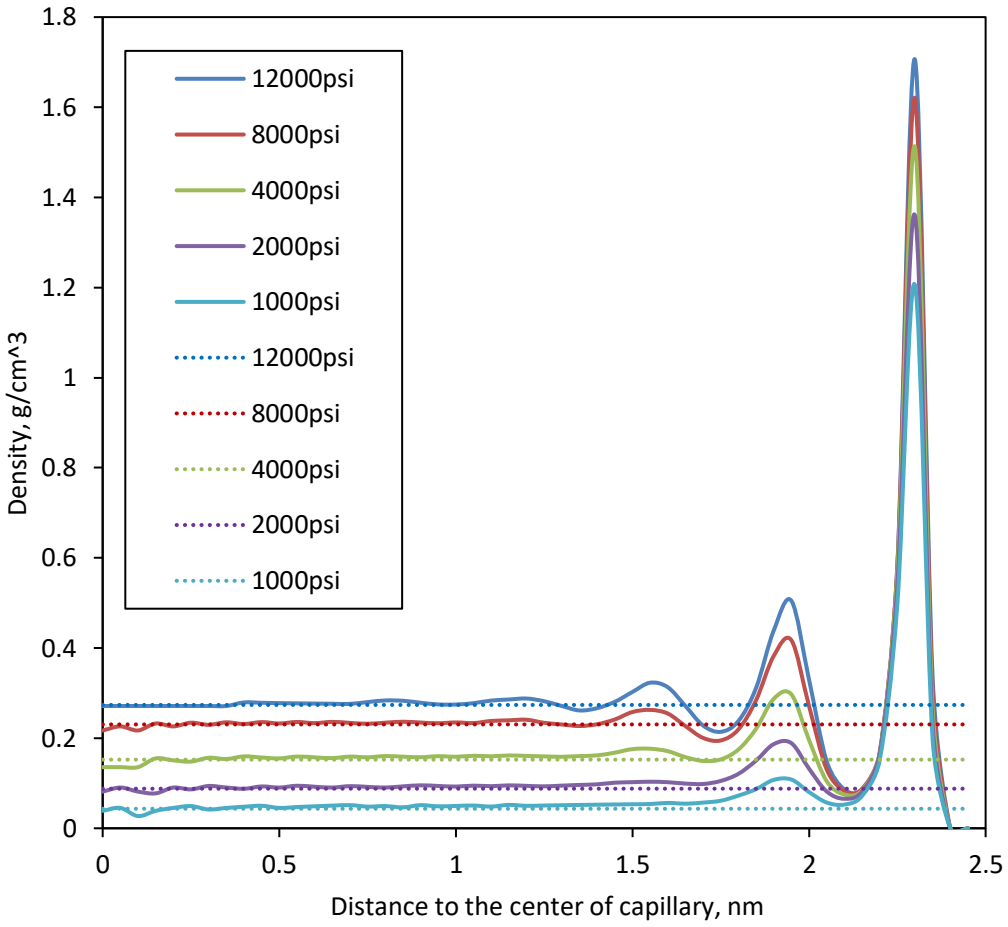

Figure 35. Methane density profile across the radius of a 5nm capillary is shown in solid line at various pore pressures. The bulk methane density values at these pressures are also shown as dotted lines. Temperature is kept constant and equal to 176F. Reprinted with permission from Society of Petroleum Engineers, Copyright 2015.

still the dominant transport mechanism in the simulation. What leads to non-zero velocity by the capillary wall is then the surface velocity of the adsorbed molecules. This could be clearly seen, when we the density profile and the velocity profile are compared in Figure 36, on the top: the two plateaus on the velocity profile near the wall align exactly with the

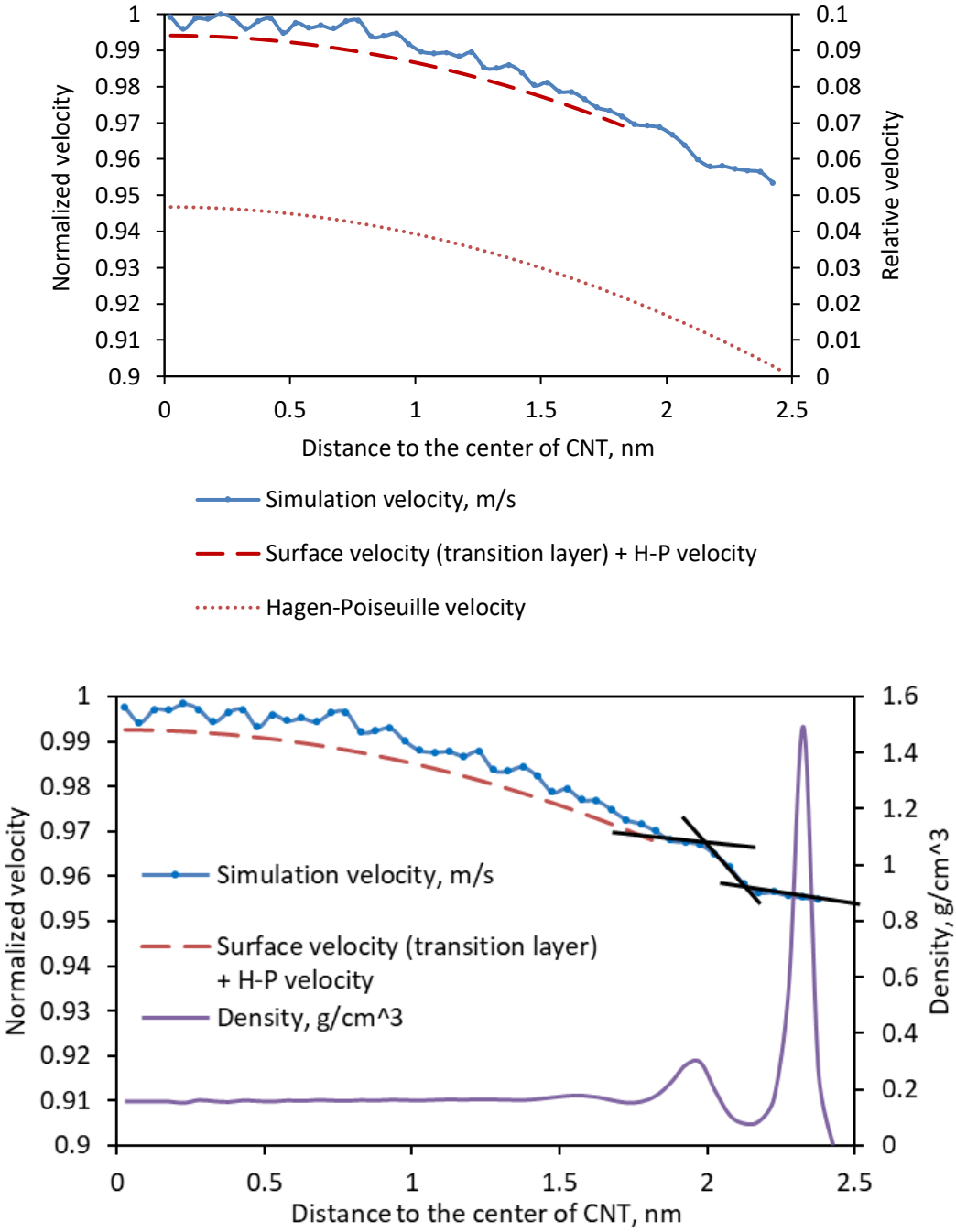

Figure 36. Illustration of surface transport inside a smooth nanocapillary, with diameter = 5nm, temperature = 176F, pressure = 4000psia, pressure gradient = 10psi/nm. The plot is from r = 0 to r = 2.5nm. Note that the Hagen-Poiseuille velocity is plotted to the secondary y-axis (left). Reprinted with permission from Society of Petroleum Engineers, Copyright 2015.

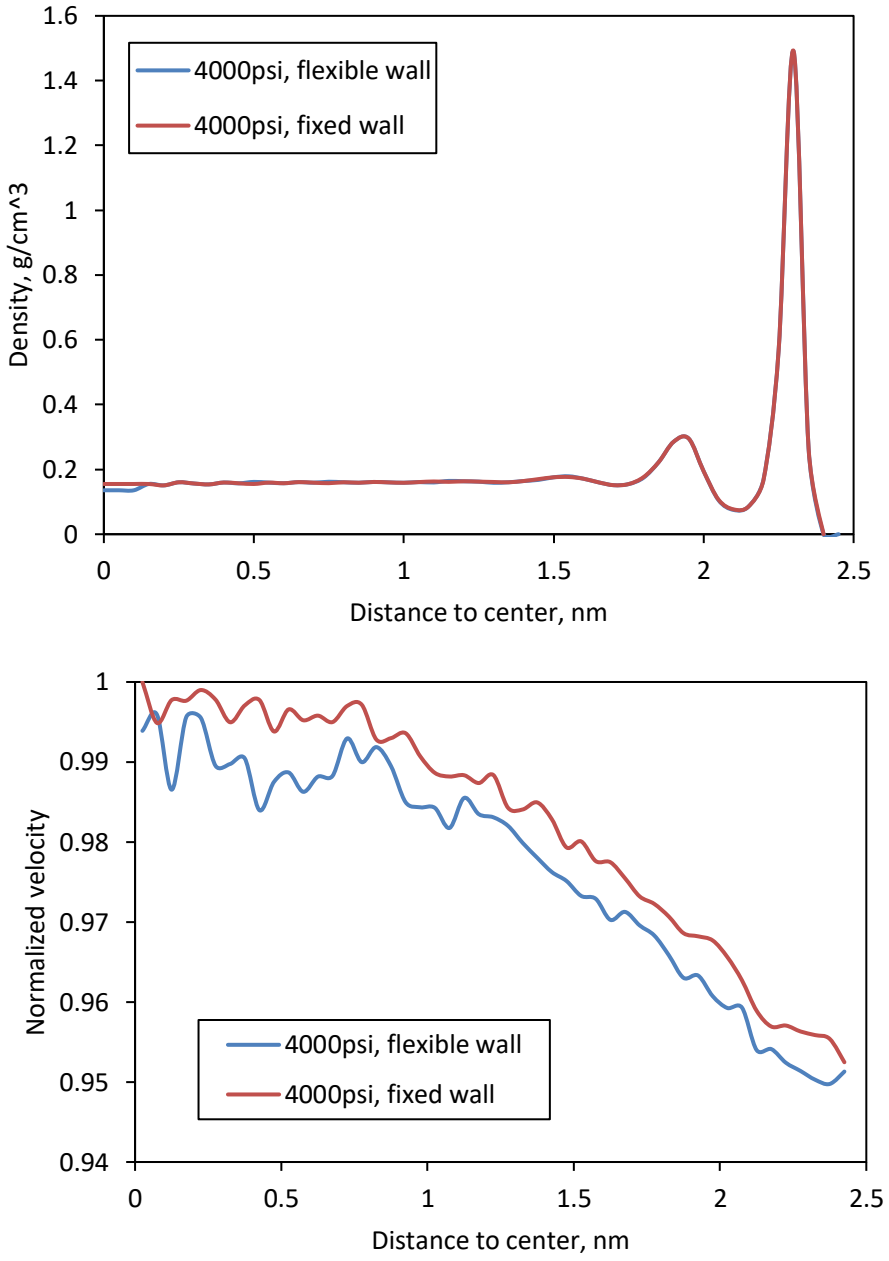

Figure 37. Treatment of carbon nanotube wall: fixed vs. flexible (modeled with Tersoff potential), with diameter = 5nm, temperature = 176F, pressure = 4000psia, pressure gradient = 10psi/nm. Reprinted with permission from Society of Petroleum Engineers, Copyright 2015.

peaks on the density profile at the bottom, indicating a mobile phase both in the adsorption layer and in the transition layer.

Another important aspect of the molecular simulation results is the fact that the superposition of the surface velocity to Hagen- Poiseuille velocity shifts up the latter to a level comparable to the numerically predicted velocity. This has recently been discussed by Riewchotisakul and Akkutlu (2015) as the lack of another transport mechanism, such as Knudsen diffusion.

It should be mentioned that the molecular simulations we have discussed so far are performed with fixed carbon atoms on the nanotube walls. However, atoms on the surface of the capillary wall can be partly mobile upon the collisions with fluid molecules. To see the wall effects, we used Tersoff potential allowing the movement of the single wall carbon nanotube atoms on the wall. The velocity profile is plotted and compared to that with fixed wall in Figure 37. The results show that the fixed-wall model can be considered as a reasonable approximation without compromising on accuracy, when considering the advantage in low computational cost.

Using the simulation setup described above, we performed a series of simulation runs varying pressure gradient, temperature, capillary diameter, and the average capillary pressure. We investigated the dependence of surface velocity on these factors. In Figure 38, we show that the estimated surface velocity can be well fitted with linear regression to the pressure gradient applied. Independently, Riewchotisakul and Akkutlu (2015) previously observed a linear dependence of the surface velocity to the pressure gradient based on their NEMD simulation study using a moving piston model. Surface velocity is

plotted with respect to the reciprocal of pore pressure for a wide range of pressures in between 1000 psia to 12000 psia. It is understandable that higher pressure means higher adsorbed density, and higher resistance to the fluid flow; and larger pore diameter means less confinement and thus smaller resistance to the fluid flow. Although it has been argued that the surface transport obeys Arrhenius relationship (Albo et al., 2006), in a small temperature range, which is the reservoir temperature range, we observe that the relationship is controlled by the applied pressure gradient. Figure 39 clearly shows that the flow is dominated by surface transport for smooth capillaries.

So far, we have discussed the surface transport in smooth capillaries. In real kerogen capillaries, the capillary walls are not perfectly smooth. Roughness could influence the surface velocity, which in turn could influence the enhancement in fluid flow in the capillary. For this purpose, we performed simulations involving rough capillary walls as shown in Figure 40, involving segmented carbon nanotubes placed inside the main carbon nanotube. The lengths and the depth of the trenches and the bumps are used as the parameters to control the morphology of the roughness, and they are set close to the sizes of common functional groups exist in kerogen. Figure 40 also shows the fluid flow behavior compared to that in capillary with smooth walls.

The double black dotted lines represent the inner carbon nanotube layer, the distance between the two layers is set to the diameter of a carbon atom. The inner layer occupies half of the volume by the wall of the main carbon nanotube and now becomes the place for the adsorbed methane molecules. Consequently, we observe limited change in the density profile of methane across the diameter of the capillary, Figure 40 (top).

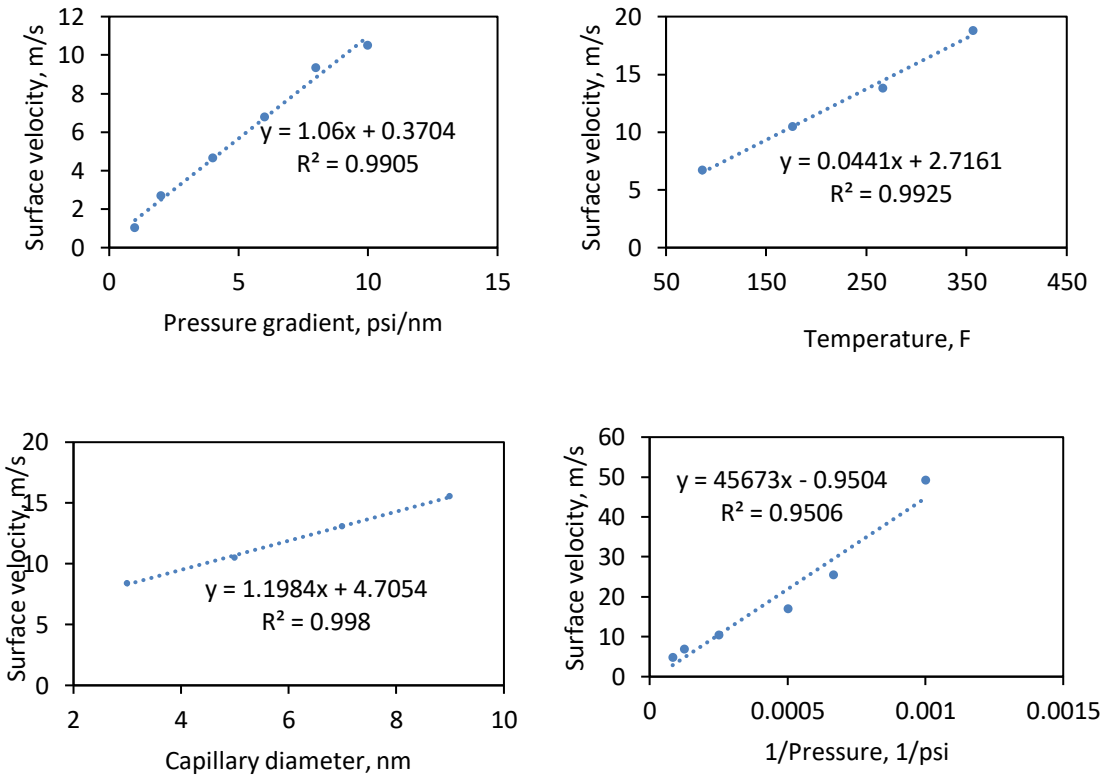

Figure 38. Sensitivity analysis of surface velocity, with respect to pressure gradient, temperature, 1/pressure, and pore diameter, if not specified, diameter = 5nm, temperature = 176F, pressure = 4000psia, pressure gradient = 1psi/nm. Reprinted with permission from Society of Petroleum Engineers, Copyright 2015.

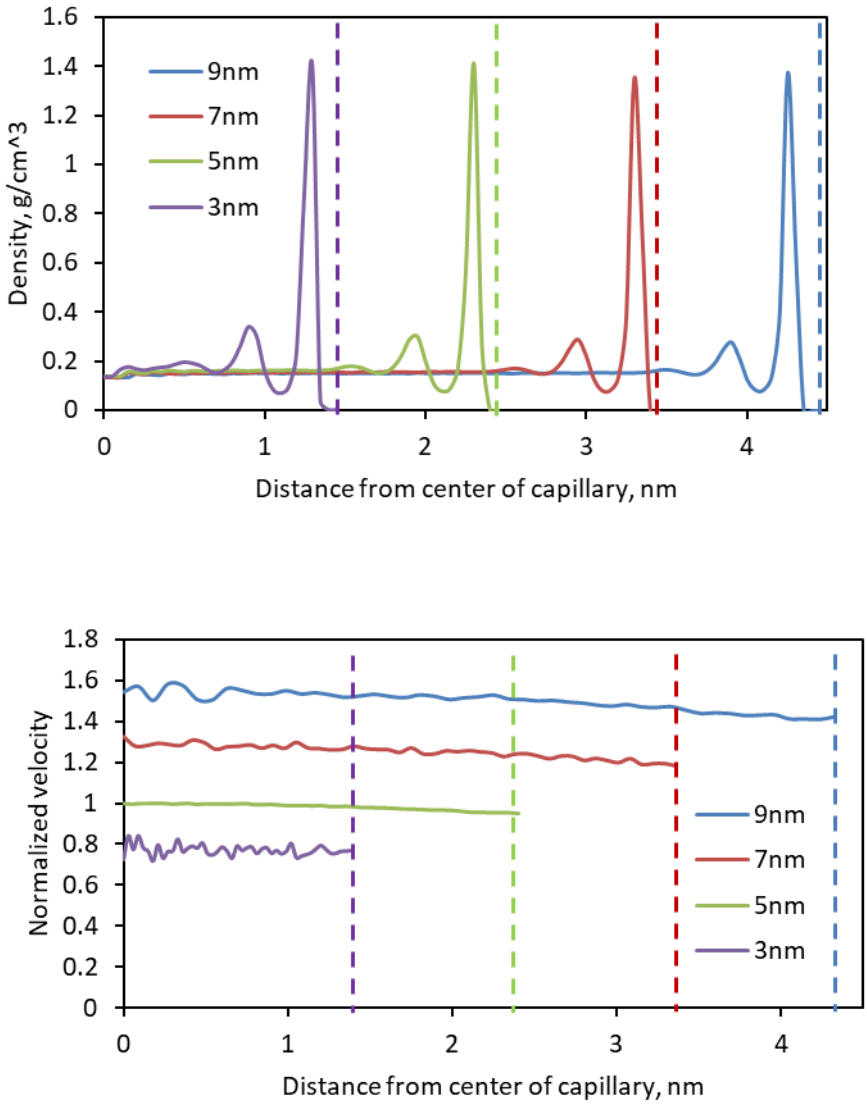

Figure 39. Density and velocity profiles at different capillary diameters, with diameter = 5nm, temperature = 176F, pressure = 4000psia, pressure gradient = 10psi/nm. Reprinted with permission from Society of Petroleum Engineers, Copyright 2015.

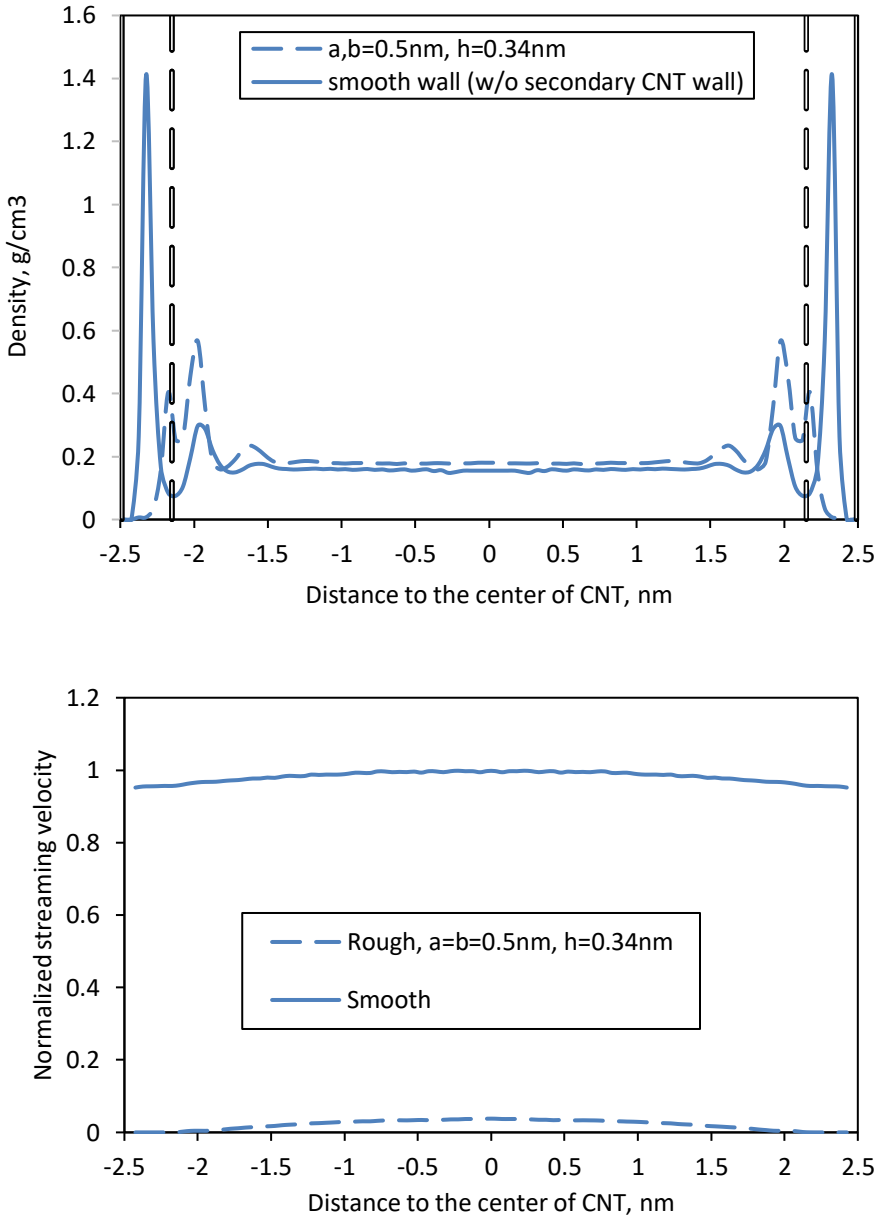

Figure 40. Comparison of rough and smooth capillaries, density profile (left) and velocity profile (right), dotted straight lines represents the segmented CNTs (Figure 34), with diameter = 5nm, temperature = 176F, pressure = 4000psia, pressure gradient = 10psi/nm. Reprinted with permission from Society of Petroleum Engineers, Copyright 2015.

Note, however, that the imposed roughness drastically reduces the surface velocity, Figure 40 (bottom), since increased number of collisions occur under the same driving force. Although the surface velocity has been decreased significantly, it is still non-zero. Figure 41 compares the simulated velocity profile to the Hagen-Poiseuille solution, shown as the dashed line. Part of the adsorbed molecules is "trapped" by the trenches, whereas a significant amount of them are still mobile near the discontinuous surfaces. So, it is conclusive that using Hagen-Poiseuille equation to describe the transport in nanocapillaries would significantly underestimates the mass flux. From the velocity profile comparison, after adding the surface velocity, the Hagen-Poiseuille velocity profile is still beneath the simulated profile, which indicates that the nanoscale confinement may also change the fluid viscosity. As in the smooth case, changing the applied pressure gradient does not affect the shape of the velocity profile (Figure 42), in other words, the surface velocity is still proportional to the pressure gradient.

The effect of surface morphology is studied by changing a, b, and h values, as shown in Figure 34. Decreasing the frequency of the inner segmented carbon nanotubes, or using larger a, b values, or increasing the smoothness, leads to an increase in surface velocity. This feature does not affect the shape of the velocity profile, however. On the other hand, adjusting the depth of the trenches by adding more inner carbon nanotube layers, reduces the effective inner diameter where flow occurs, but does not affect the surface velocity at all. The density of the inner most adsorption layer, which contributes to the transport because of the surface velocity, stays constant with the change in h value. However deeper trenches lead to more immobile methane molecules (Figure 45).

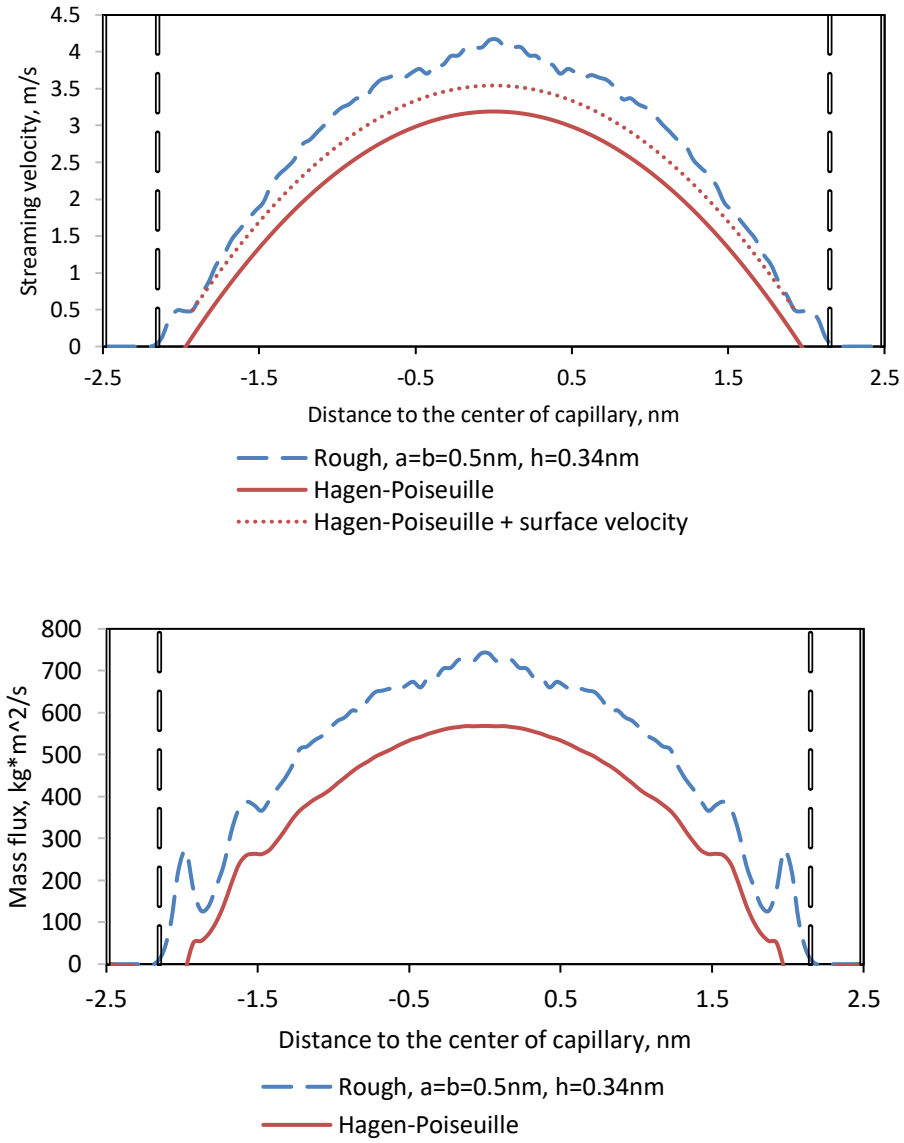

Figure 41. Comparison of simulated velocity profile and result from Hagen-Poiseuille equation, for rough capillaries: velocity (left), mass flux (right), with diameter = 5nm, temperature = 176F, pressure = 4000psia, pressure gradient = 10psi/nm. Reprinted with permission from Society of Petroleum Engineers, Copyright 2015.

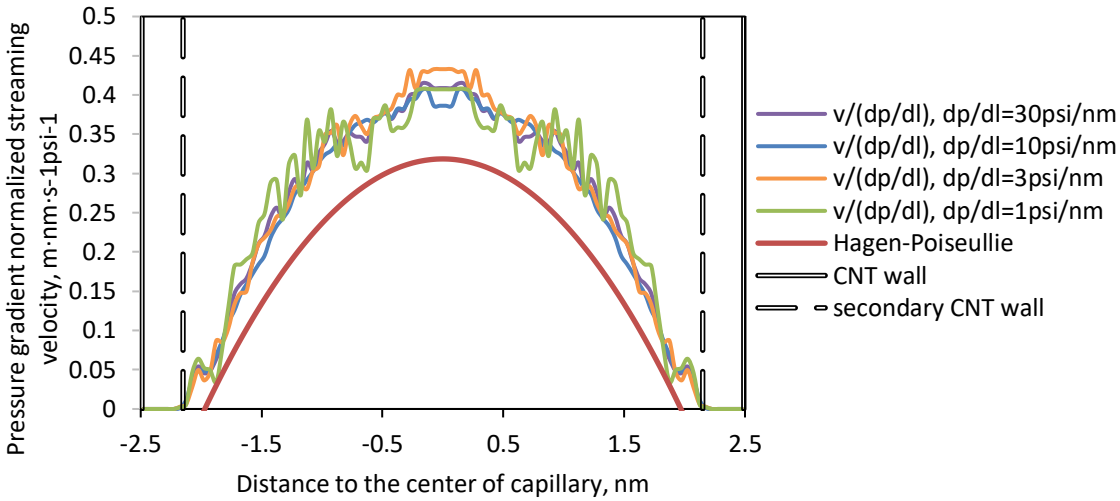

Figure 42. Pressure gradient normalized velocity profile, varying pressure gradient, with diameter = 5nm, temperature = 176F, pressure = 4000psia, pressure gradient = 10psi/nm, *a, b* = 0.5nm, *h* = 0.34nm. Reprinted with permission from Society of Petroleum Engineers, Copyright 2015.

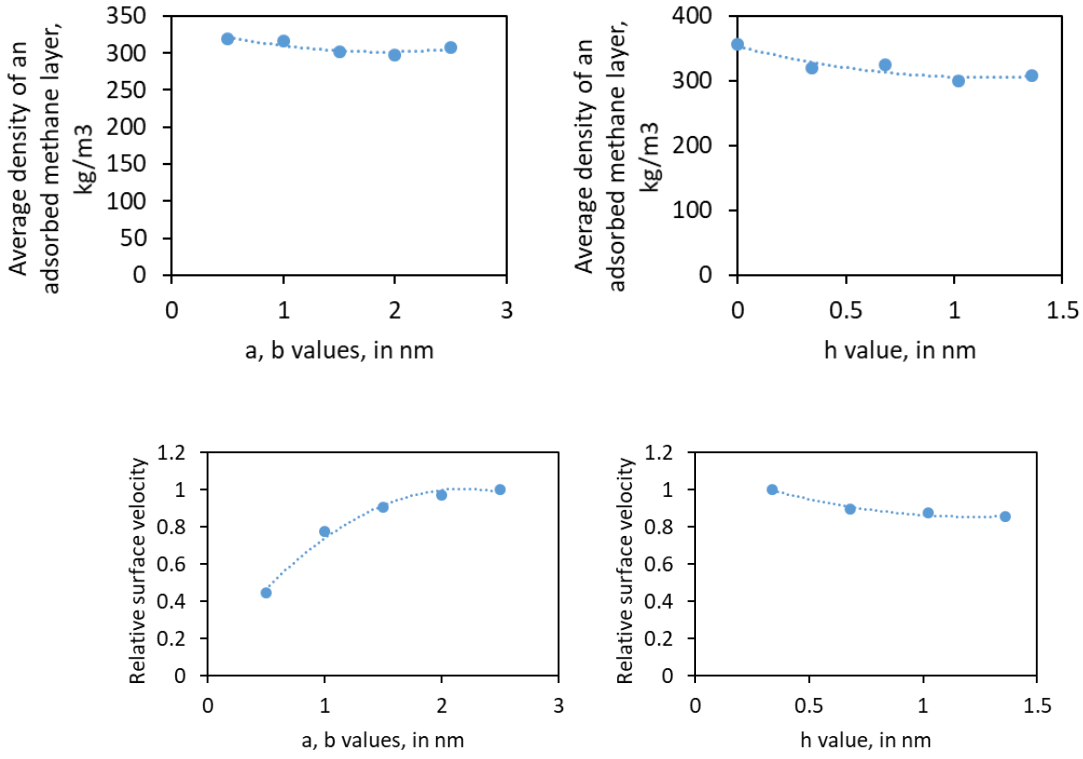

Figure 43. The relationship between surface roughness and surface velocity. Reprinted with permission from Society of Petroleum Engineers, Copyright 2015.

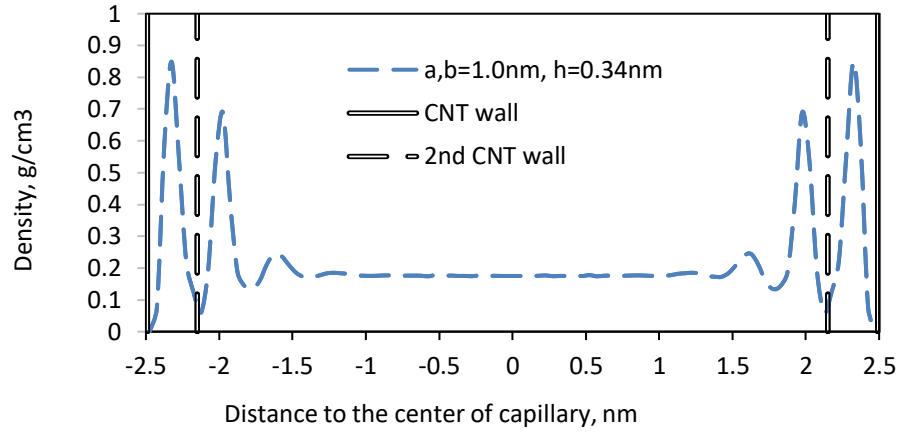
Density, g/cm3
1
0.9
0.8
0.7
0.6
0.5
0.4
0.3
0.2
0.1
0
-2.5
-2
-1.5
-1
-0.5
0
0.5
1
1.5
2
2.5
a,b=1.0nm, h=0.34nm
CNT wall
2nd CNT wall
Distance to the center of capillary, nm

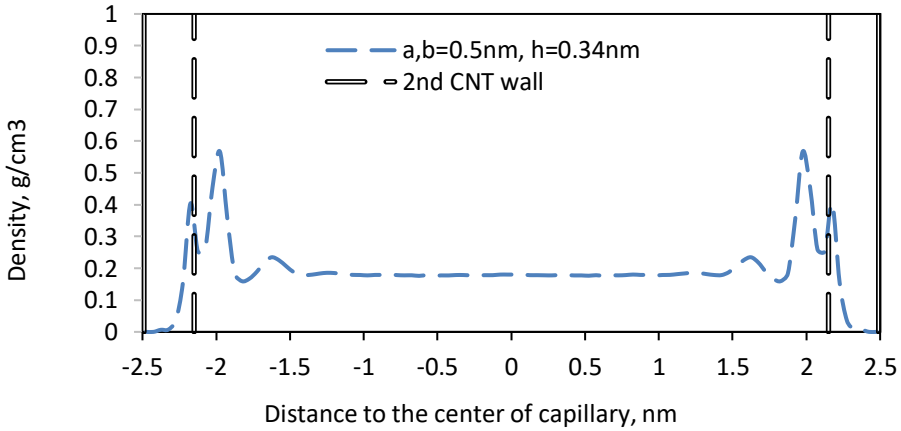
Density, g/cm3
1
0.9
0.8
0.7
0.6
0.5
0.4
0.3
0.2
0.1
0
-2.5
-2
-1.5
-1
-0.5
0
0.5
1
1.5
2
2.5
a,b=0.5nm, h=0.34nm
2nd CNT wall
Distance to the center of capillary, nm

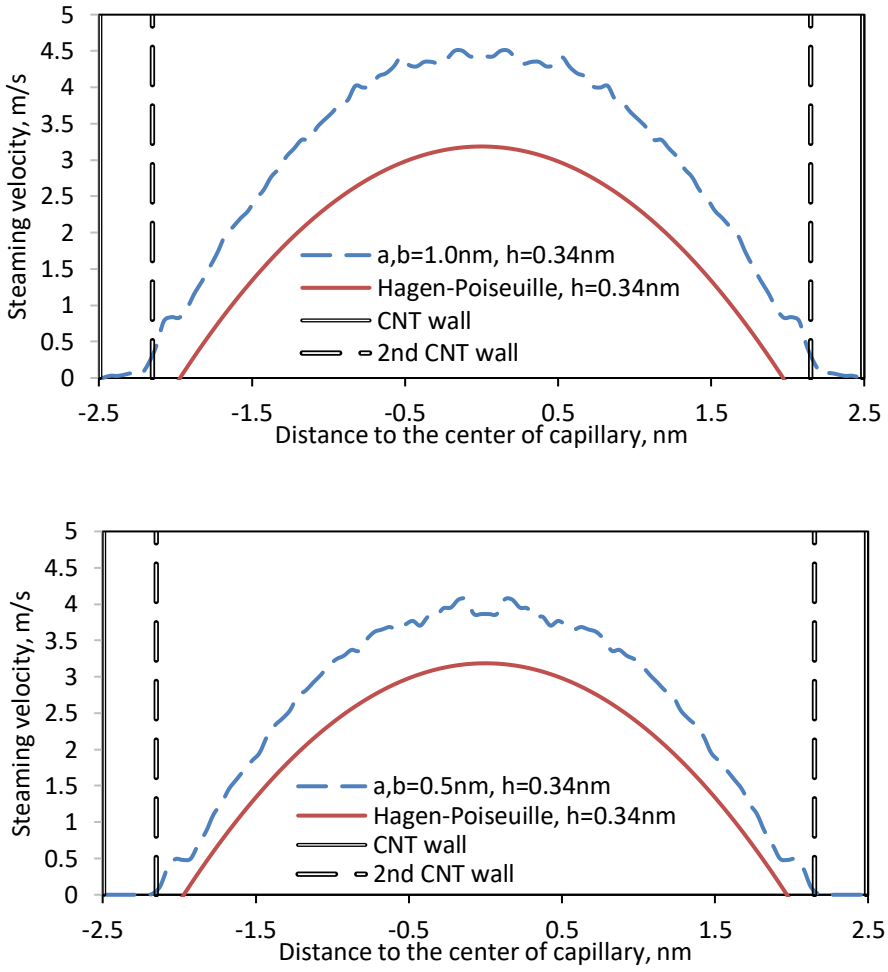

Figure 44. Density and velocity profiles of rough capillaries, changing *a, b* values, with diameter = 5nm, temperature = 176F, pressure = 4000psia, pressure gradient = 10psi/nm. Reprinted with permission from Society of Petroleum Engineers, Copyright 2015.

Determination of *a*, *b* and *h* values based on the real kerogen pore structure can be challenging since the nanocapillaries are too small to measure such intricate features using the conventional measurement techniques. Figure 46 shows the contribution of surface transport under varying capillary diameter, pressure and temperature and compares to the Hagen-Poiseuille flow. With the decrease in diameter, although the relative flow rate is

reduced, the contribution of surface transport increases and eventually in capillaries with a diameter less than 4nm, exceeds that contribution expected from Hagen-Poiseuille. Surface transport also favors low pressure and high temperature conditions. Contribution of surface transport prevails for reservoir pressures as low as 1000 psi. The deviation from conventional Hagen-Poiseuille flow behavior is determined by the density ratio of the free/adsorbed phases, viscosity, and surface velocity.

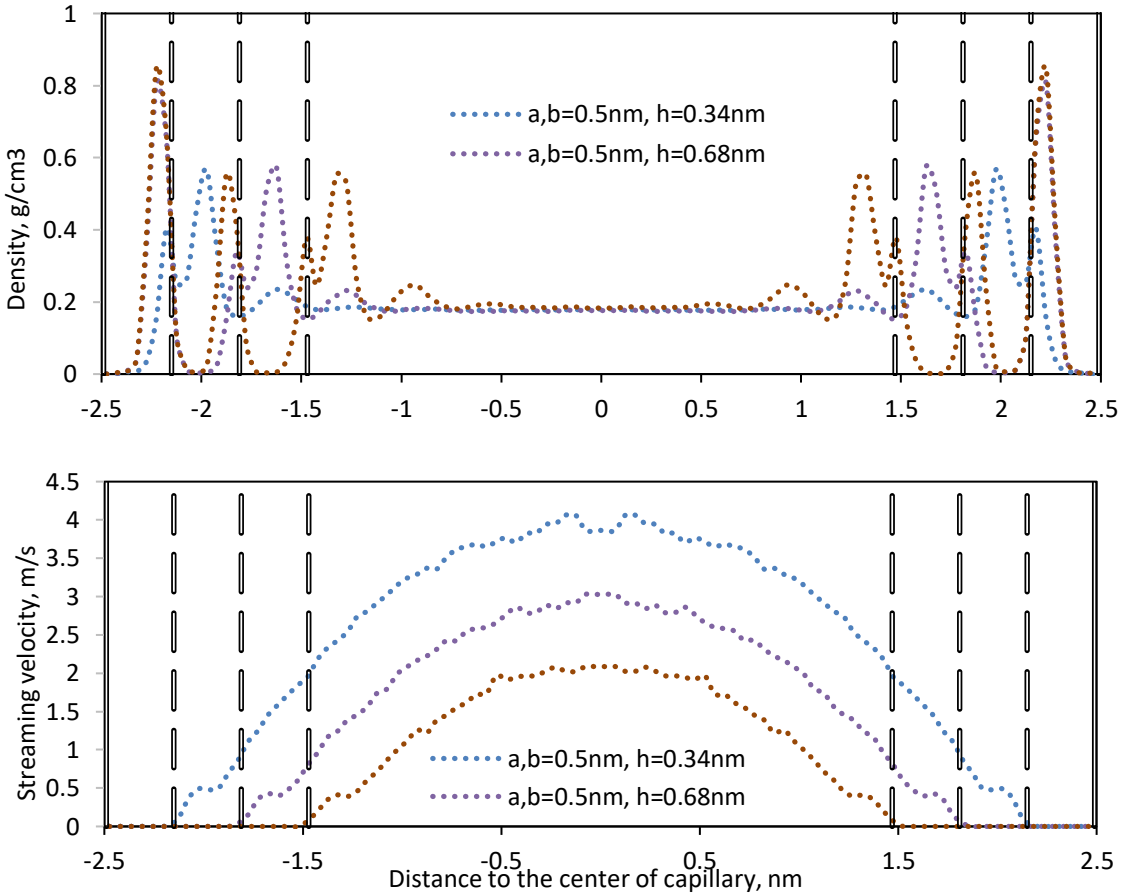

Figure 45. Density and velocity profiles of rough capillaries, changing h value (1~3 layers, respectively), with diameter = 5nm, temperature = 176F, pressure = 4000psia, pressure gradient = 10psi/nm. Reprinted with permission from Society of Petroleum Engineers, Copyright 2015.

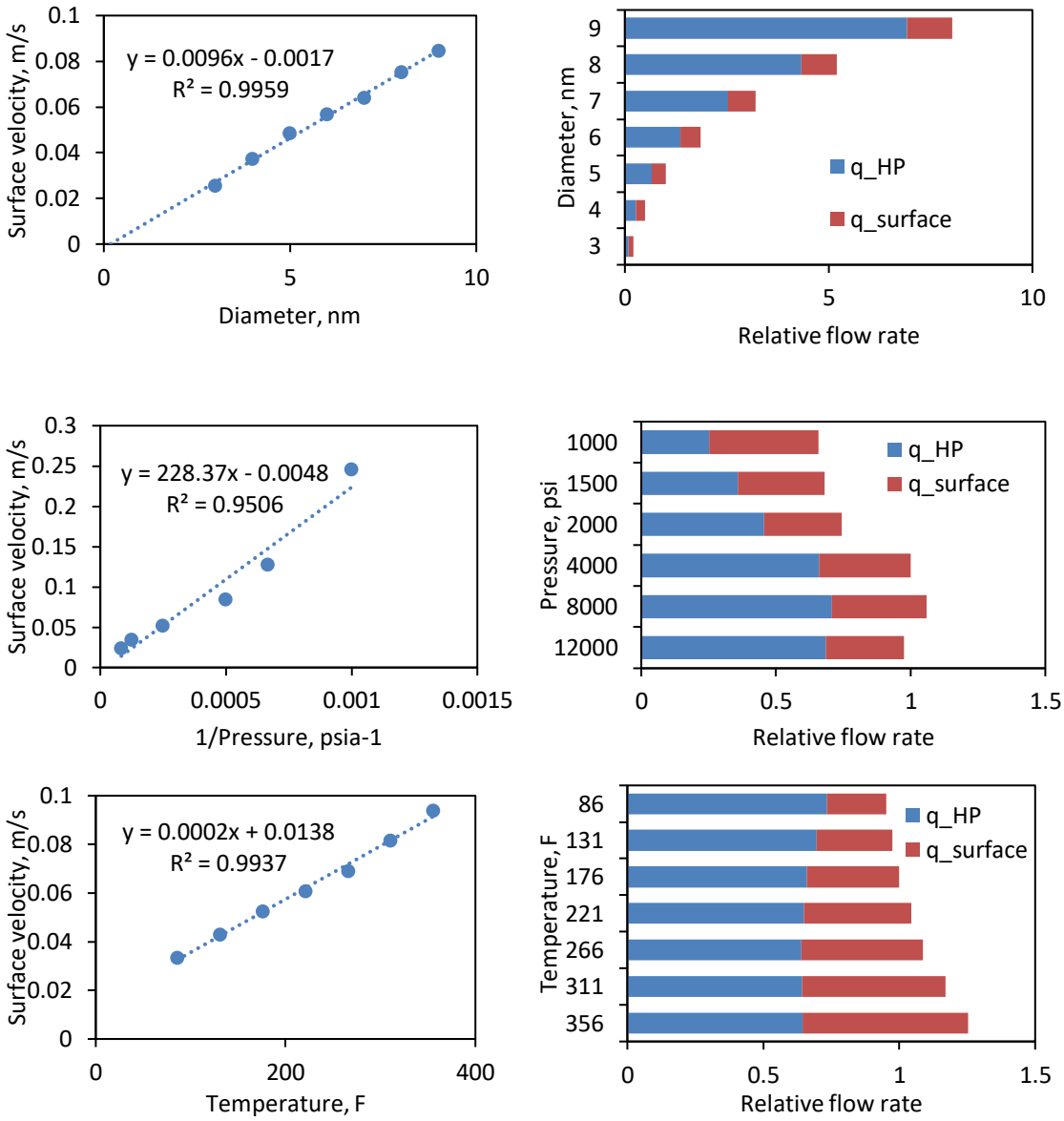

Figure 46. Dependence of surface velocity on diameter, pressure, and temperature for rough capillaries (left), relative flow rate (right, total flow rates for 5nm, 4000psi, 176F are set to 1, respectively), with diameter = 5nm, temperature = 176F, pressure = 4000psia, pressure gradient = 1psi/nm, *a*, *b* = 0.5nm, *h* = 0.34nm. Reprinted with permission from Society of Petroleum Engineers, Copyright 2015.

In the case of multi-component fluids, the classical single-phase fluid flow theory assumes that the streaming velocity should be the same for each component. However, in organic nanocapillaries with strong adsorption effect, since different components have different sizes and weights, the interactions with rough surfaces should have different levels of effects on the adsorption and transport of the fluid molecules. Literature on gas separation technologies and on coalbed methane is large and includes such discussions, see for example Yi et al. (2008) and Fathi and Akkutlu (2014) for selective adsorption, counter and co-diffusion effects.

Figure 47, includes the flow simulation results for a binary (methane, n-butane) mixture. The surface roughness is kept the same for the simulations. Note that the surface velocity of the two components are different. Heavier component, n-butane, molecules are moving slower near the wall compared to the lighter component, methane. At the center of the capillary both velocities are the same, but as the walls are approached, we observe that the lighter component is transported faster. In the transition zone, co-flow has a dragging effect on methane and acceleration effect on n-butane. Hence, once again, we experience a deviation in flow based on the classical Hagen-Poiseuille formulation. Furthermore, if we consider larger spacing in between the wall and the inner tube, then transport in the transition layer develops within that inner space due to the molecules trapped in the trenches contributing to the overall transport by “hopping” through the barriers. This results in a non-zero surface velocity between the inner and outer capillaries. Whether the fluid molecules will be trapped or not really depends on the steric effects, i.e., the relative sizes of the fluid molecules (Table 2) and the sizes of the bumps and trenches.

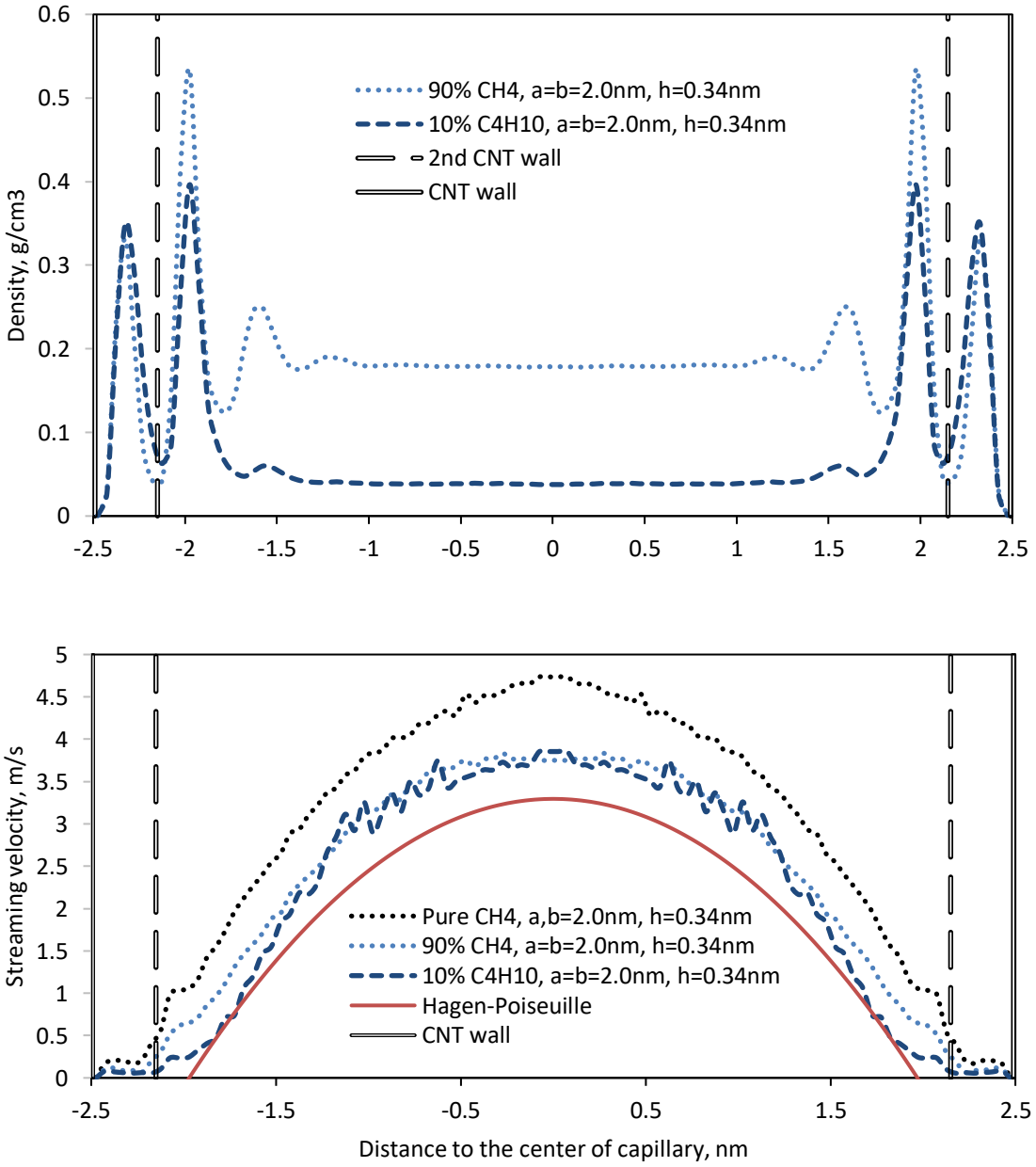

Figure 47. Density and velocity profiles of rough capillaries, for methane-butane mixture, mole fraction (90% CH_4 -10% C_4H_{10}), changing h value, with diameter = 5nm, temperature = 176F, pressure = 4000psia, pressure gradient = 10psi/nm. Note that the pure methane velocity profile is also plotted, showing the dragging effect of adding a heavier component. Reprinted with permission from Society of Petroleum Engineers, Copyright 2015.

This observation indicates the complexity of transport in rough capillaries, albeit we are using a very simple inner surface model. Note that, comparing the multi-component results with that in a capillary with smooth surfaces under the same condition, the surface-velocity of the binary case is the same as the single-component case. The mobile adsorption layer is rich in heavier component, which reduces the overall surface velocity; on the other hand, with the rough surfaces the reduction is much larger, due to the inner capillary ring reducing the mobility of the adsorbed phase. Figure 48 shows density and velocity profiles of fluid smooth capillaries for comparison purposes.

Table 2. Effective sizes and length of common fluid molecules (Reprinted from Mao & Sinnott, 2001)

Component	**Effective diameter nm**	**Effective length nm**
Methane	0.399	0.399
Ethane	0.399	0.476
n-Butane	0.415	0.824
iso-Butane	0.635	0.635

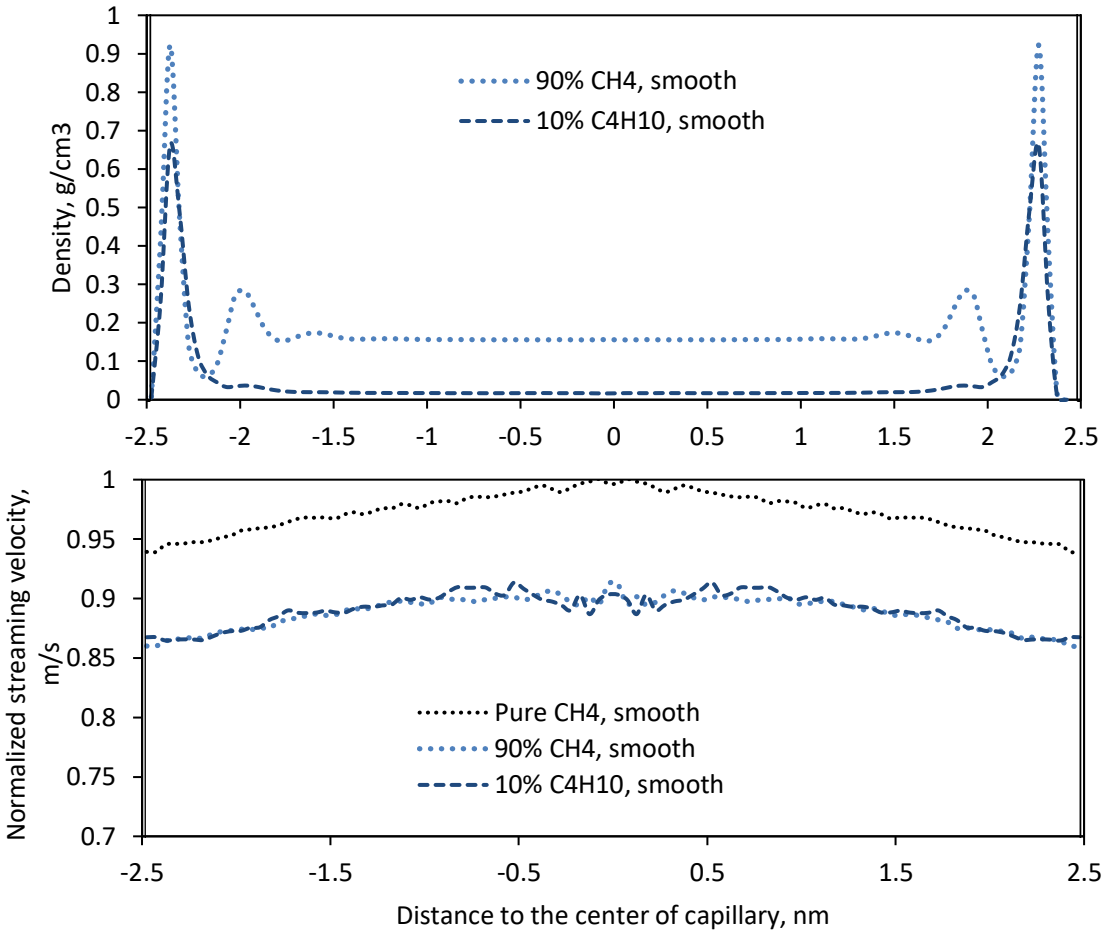

Figure 48. Density and velocity profiles of smooth capillaries, for methane-butane mixture, mole fraction (90% CH_4 -10% C_4H_{10}), changing h value, with diameter = 5nm, temperature = 176F, pressure = 4000psia, pressure gradient = 10psi/nm. Note that the pure methane velocity profile is also plotted, showing the dragging effect of adding a heavier component. Reprinted with permission from Society of Petroleum Engineers, Copyright 2015.

Summary

In this chapter, we considered the fluid transport inside model nanocapillaries with varying sizes and wall properties to gain insight into the shale gas transport and production mechanisms. It is found that the surface transport associated with the adsorbed phase plays an important role in enhancing the fluid flow. The transport enhancement can be clearly observed using the concept of relative flow rate, or simply by calculating the mass flux across the capillary by multiplying the non-zero surface velocity by the total amount of hydrocarbons across the intersection of the capillary. Transport behavior is additionally controlled by the inner capillary wall surface morphology, which requires considerable modeling work from the real kerogen structures to fully determine the transport enhancement. Using segmented carbon nanotube rings inside the single-wall carbon nanotube is a simple way to mimic the rough structures in real kerogen capillaries, without diving into the chemical complexity of the real functional groups. For the transport of multi-component fluids, the surface velocity is different for each component and needs to be considered separately.

CHAPTER III

MODELING AND SIMULATION OF 3-D KEROGEN POROUS NETWORK*

Understanding the molecular structure of kerogen as part of the source rock characterization efforts is an important and fast-evolving science. The basic chemical structure of kerogen has been under investigation by the geochemists long before the interest in shale gas production (Vandenbroucke, 2003). Hybrid experimental-simulation methods have been extensively used to create realistic molecular models for kerogen nanostructures. Based on the optimized molecular reconstruction procedure, kerogen samples of all maturity levels from representative basins are taken to generate molecular structures as basic molecular building blocks. The recently published kerogen molecular structures are validated with molecular simulation and agree well with the experimental results (Bousige, Botan, Ulm, Pellenq, & Coasne, 2015; Bousige et al., 2016; Ungerer et al., 2015). The molecular simulation methods are also widely applied to solve real-world problems such as natural gas storage capacity and transport in kerogen (Collell et al., 2015; Falk, Coasne, et al., 2015; Falk, Pellenq, et al., 2015; Ho, Criscenti, & Wang, 2016; Lee, Bocquet, & Coasne, 2016). The force fields often used in these studies include a series of Class I and Class II force fields: CVFF (Dauberosguthorpe et al.,

* Part of this chapter is reprinted with permission from "A Simple Molecular Kerogen Pore-network Model for Transport Simulation in Condensed Phase and Digital Source-Rock Physics" by F. Feng, I. Yucel Akkutlu, Transport in Porous Media, 126.2 (2019): 295-315. Copyright 2018 by Springer Nature B.V.

1988), PCFF (Sun, 1995; Sun et al., 1994), PCFF+ (Collell, Ungerer, et al., 2014), and COMPASS (Sun, 1998).

However, these molecular models are far from being perfect representations of kerogen with a certain desired quality. First, the molecular simulation systems investigated have scales less than 100 nm, which are much smaller than the representative elementary volume (REV, Figure 49) of rocks (Kou, Alafnan, & Akkutlu, 2017). Previous methods focus on the detailed atomistic description of the kerogen such that their sizes are limited, and they do not include the complete pore network information of the kerogen, such as the presence of mesopores, which have a significant influence on the gas transport (Figure 50). Fluid molecules could experience larger mass fluxes and different transport mechanisms as the pore size change (Hahn, Karger, & Kukla, 1996; Mutat, Adler, & Sheintuch, 2012a). Second, the pore network geometry information can be obtained from TEM imaging but TEM does not help us to build the molecular models of the solid kerogen. Finally, obtaining the exact molecular model of kerogen can be costly or impractical for today's oil and gas industry because substantial experimental and simulation work is required to obtain the basic kerogen building block. Whereas often the industry's only concern is obtaining the petrophysical properties of the source rock. Therefore, simplifications on the exact kerogen molecular models are required to better adapt to the industrial applications. Such a process should include simplification of the molecular structure of the kerogen, implementation of new force field parameters for the imposed simplification, and validation. With the simplified

models, one would hope to accurately determine the permeability of the kerogen using molecular simulation based on microscopic structure, without losing accuracy.

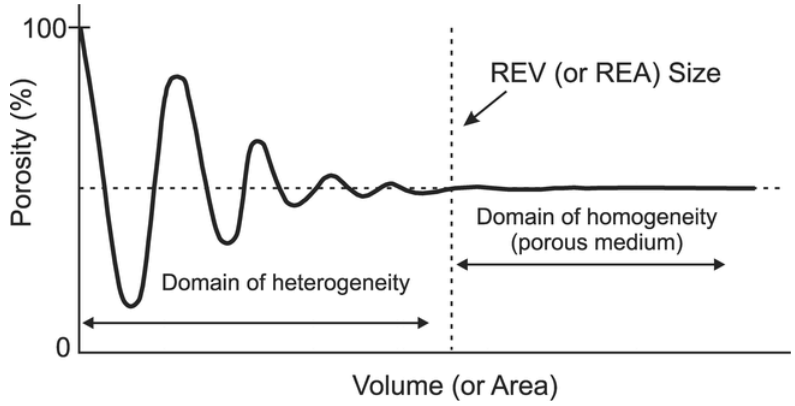

Figure 49. Representative elementary volume (REV) (Reprinted from Norris & Lewis, 1991)

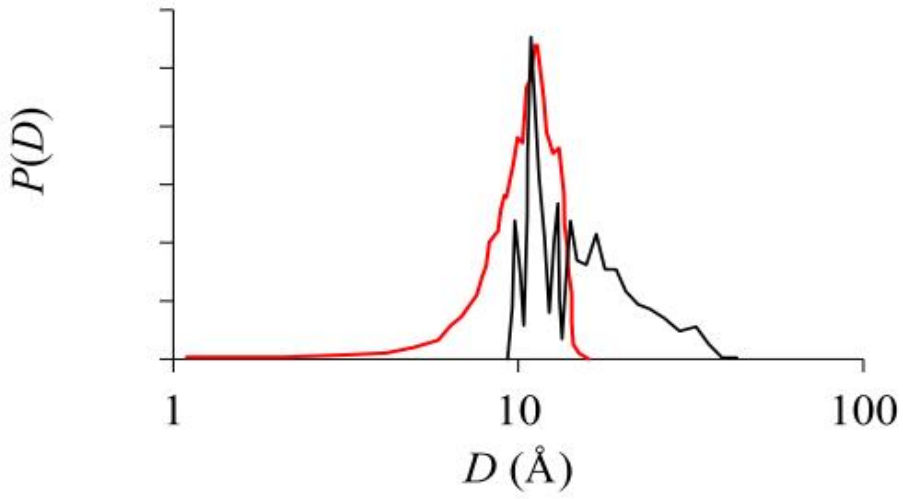

Figure 50. Pore size distribution P(D) for the numerical sample considered in this work (red line) and for an experimental kerogen sample (Marcellus kerogen, black line). The experimental data, which are taken from Clarkson et al. Fuel (2013), were obtained by means of CO_2 adsorption (Falk, Coasne, et al., 2015)

Model Description

In previous studies, 3-D kerogen models have been generated by replicating the molecular structure representing the basic kerogen building block, which consists of hundreds of C, H, N, O, S atoms, but mainly C and H. The radical groups only contain C and H are non-polar. On the other hand, the common fluid molecules, hydrocarbons (C_xH_y), N_2, and CO_2 are all non-polar. As a result, the inter-atomic interactions between fluid and kerogen can be mostly described by Lennard-Jones potential (Equation 6, Equation 7, Equation 8). In addition, the Lennard-Jones parameters for different united atoms (containing C, N, and O) are close. Based on this fact, we see the potential to degenerate different types of atoms in the kerogen model into one unified atom type, so that the inter-atomic interactions are mostly kept the same as the full chemistry model. Specifically, the basic idea is to keep the number of united atoms unchanged, and the pore volume unchanged, with some method to average the Lennard-Jones parameters of the different atoms in the full chemistry model. Several combinations of weighted means for ϵ and σ, including arithmetic, geometric and harmonic means are tested. Different close-packing methods, including face-centered cubic (FCC), hexagonal close-packed (HCP), and diamond cubic packing (DCP).

After several experiments, an ideal simplification method is found. With this method, all intra-molecular and inter-molecular interactions of the full chemistry model, described by Class I or Class II force field formulations, are expected to be replaced by a uniform, simple interatomic Lennard-Jones 12-6 potential (Equation 24). The force field

parameters which are used to calculate the average (Equation 25) are obtained from the PCFF force field (Sun et al., 1994) with $\sigma_{12-6} = \sigma_{9-6}/1.12246$ and summarized in

In the flow simulation, OPLS-AA force field is used to describe fluid molecules, with bond, angles, dihedrals described in the equation forms below.

$$E = K\ r - r02 \quad \textbf{Equation 33}$$

$$E = K\ \theta - \theta 02 \quad \textbf{Equation 34}$$

$$= 12K11+cos\phi+12K21-cos2\phi+12K31+cos3\phi+12K41-cos4\phi \quad \textbf{Equation 35}$$

Table 5, Appendix. In the PCFF force field, the atoms at different chemical environments are of different atom types, however, only the most common types in kerogen molecules shown in Figure 51 are used to represent all the atoms of the same element name. In this model, despite the intra-molecular forces are ignored to save computational cost, most geometrical information of the structure, as well as the intermolecular forces, can be retained.

$$V(r) = 4\epsilon\left[\left(\frac{\sigma}{r}\right)^{12} - \left(\frac{\sigma}{r}\right)^{6}\right] \quad \textbf{Equation 24}$$

where ϵ and σ are weighted geometric, arithmetic mean of atoms, respectively.

$$\epsilon = \prod_{i=C,H,N,O,S} \epsilon_i^{\frac{n_i}{n_{total}}}$$

$$\sigma = \frac{\sum_{i=C,H,N,O,S} n_i\sigma_i}{n_{total}} \quad \textbf{Equation 25}$$

the density of the atom can be determined by the arithmetic mean (Equation 26).

$$m = \frac{\sum_{i=C,H,N,O,S} n_i m_i}{n_{total}} \quad \textbf{Equation 26}$$

The simplified molecular pore network model shall be built based on a given 3-D voxel image of kerogen pore network. The organic matter volume that makes up the skeleton is filled with the averaged "pseudo-atoms". Diamond cubic packing is used when populating with the pseudo-atoms (Figure 52). This packing has a coordination number of atoms equal to 4, which is close to that in a typical organic matter that make up kerogen. Thus, the chemical environment of the pseudo-atoms can best mimic the exact kerogen molecular structure. When filling up the solid spaces, a trial interatomic distance can be assigned first and then adjusted iteratively until the density of the solid system reaches the desired value.

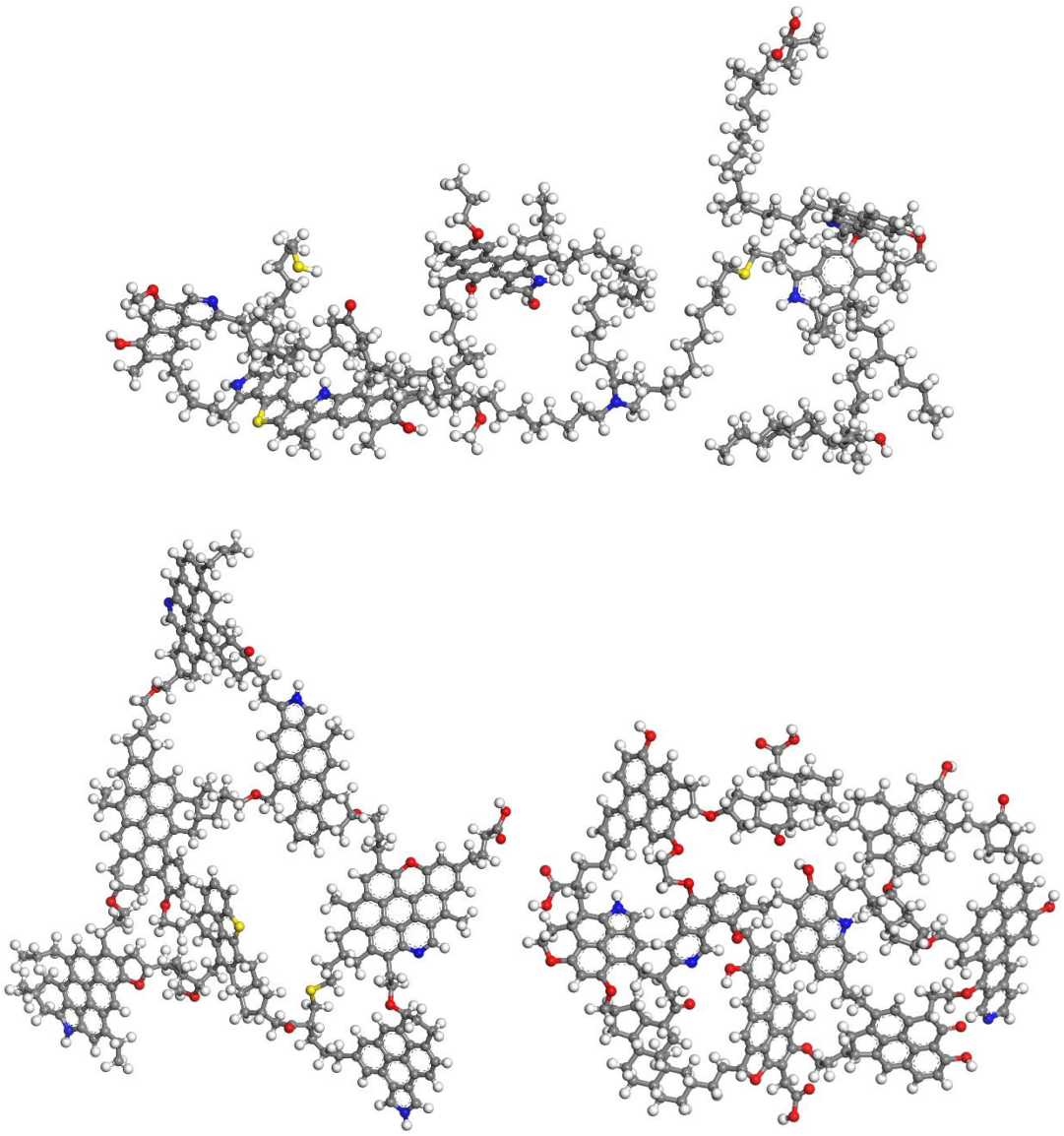

Figure 51. Kerogen molecular structures, act as molecular building blocks used in this work, Type II-C, Type I-A, and Type III-A, respectively (Reprinted from Ungerer et al., 2015)

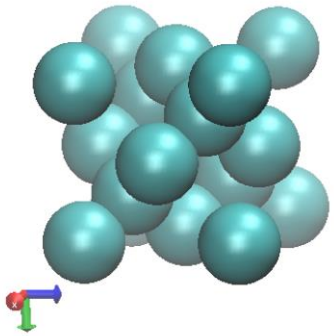

Figure 52. Diamond cubic packing: note that the atoms are the averaged pseudo atoms instead of carbon. Reprinted with permission from Springer Nature B.V., Copyright 2018.

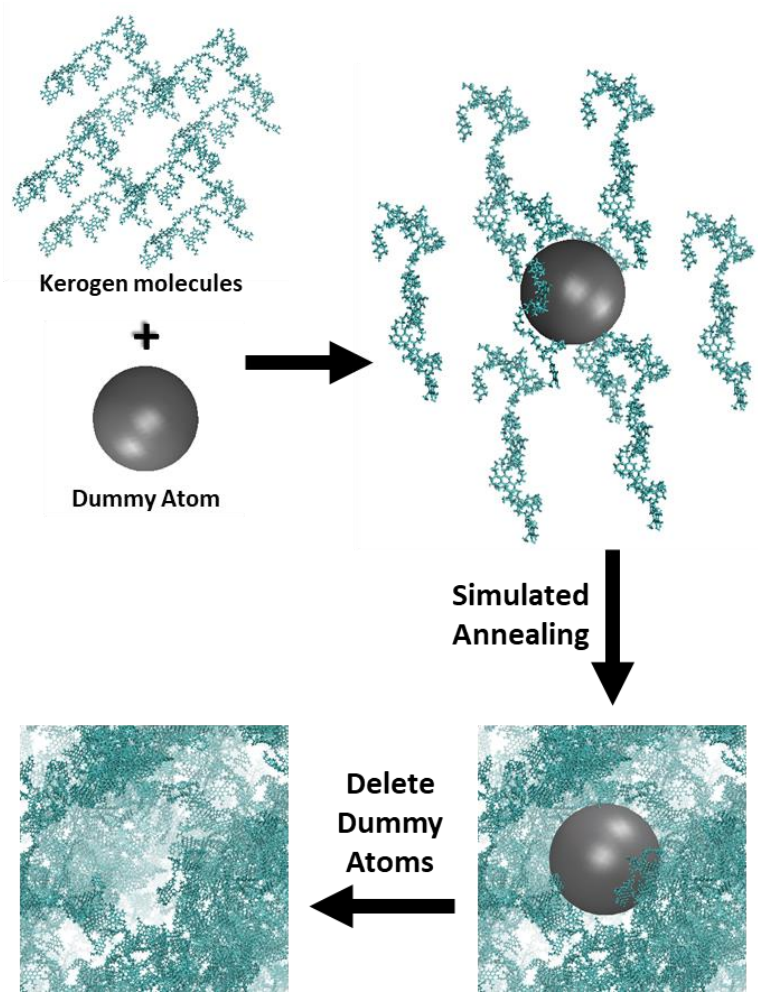

Figure 53. Using dummy atoms to create mesopores and control PSD. Reprinted with permission from Springer Nature B.V., Copyright 2018.

The 3-D voxel images can be generated using 3-D TEM or STEM tomography of the real kerogen samples, with resolution high enough to capture the detailed geometrical information of the pore network. However, when experimental tomography is not available, imaginary sample structures can be used to test the validity of the methodology explained above. Specifically, samples pore structures containing the much needed mesopores can be generated using multiple previously published kerogen building blocks with simulated annealing molecular dynamics simulation (Collell, Ungerer, et al., 2014; Ungerer et al., 2015). To include necessary mesopores and pore network in the kerogen molecular structure, dummy atoms of different sizes can be mixed together with kerogen building blocks before simulated annealing, and then be

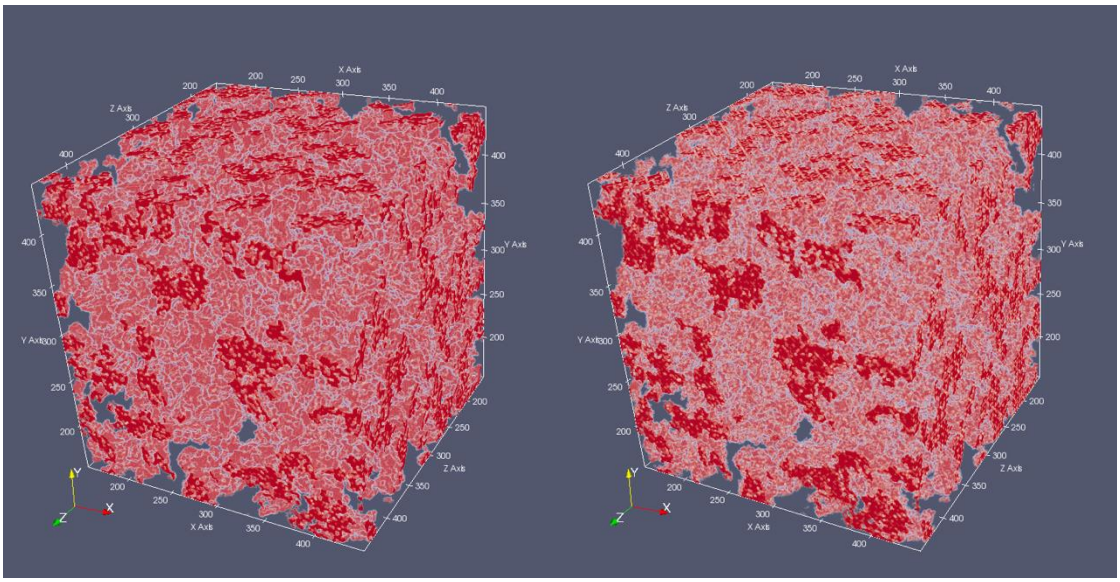

Figure 54. A sample 3-D pore network, visualized with Paraview, pore space shown in grey, organic solid shown in red, left: random kerogen sample constructed by exact kerogen building blocks (Type II-C), right: the same kerogen sample constructed by the simplified kerogen molecular model, with length unit of Angstrom. Reprinted with permission from Springer Nature B.V., Copyright 2018.

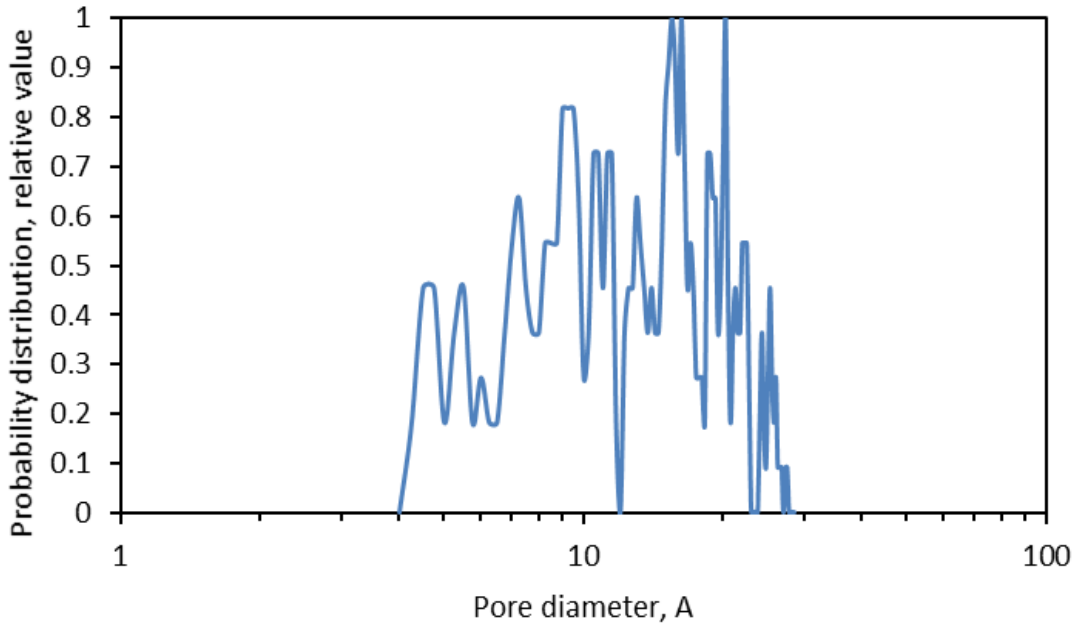

Figure 55. Pore size distribution of the pore network in Figure 54, calculated with (Bhattacharya & Gubbins, 2006), with minimum test particle size of 0.4 nm

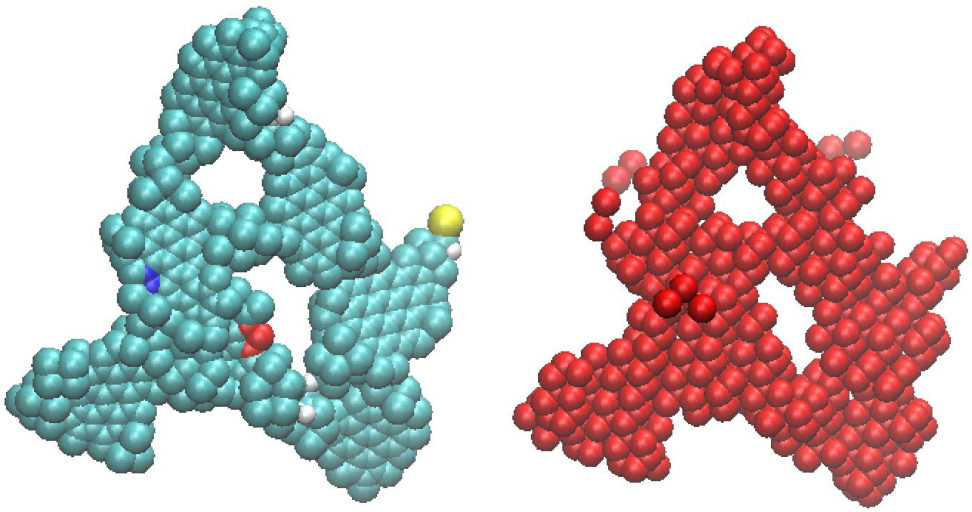

Figure 56. The comparison between the exact kerogen molecular structure (Type II-C kerogen, with most hydrogen atoms implicit, left. Cyan: carbon, yellow: sulfur, red: nitrogen, blue: oxygen, white: hydrogen) (Ungerer et al., 2015) to the simplified model, packed with standard cubic packing (right).

removed afterward (Figure 53). Inserting dummy atoms has been proven to be an effective way to add larger pores in organic kerogen structure, and this approach was proposed independently by other researchers (Zhou, Xu, & Jiang, 2016) .

After the 3-D sample structure is generated, it can be scanned into 3-D voxel images, based on which the simplified molecular model, with identical geometric features, can be generated (Figure 54 and Figure 56).

Flow Simulations

The primary goal of this simplified molecular model is to accurately simulate fluid flow in realistic kerogen structures. To simulate transport in model organic porous media, non-equilibrium molecular dynamics simulation shall be used, with external field non-equilibrium molecular dynamics (EF-NEMD) and dual control volume grand canonical molecular dynamics (DCV-GCMD) being the most popular methods (Arya et al., 2001). In the first method, a uniform external force field is applied to all the fluid molecules in the porous medium as the driving force; whereas in the second method, two separate fluid reservoirs are placed on both sides of the porous medium and maintained at different constant pressures with Grand Canonical Monte Carlo (GCMC) simulation, to drive the fluid flow through the porous media.

Although the first method is simple and computationally efficient, the dynamics of each fluid molecule inside are modified directly by the external field instead of real intermolecular interaction. On the other hand, DCV-GCMD overcomes such problem by generating particle flow with a realistic chemical potential gradient, and pressure gradient can be generated and maintained directly. So, it is widely used for simulation of gas flowing through organic porous media (Collell et al., 2015; Firouzi & Wilcox, 2012). However, DCV-GCMD is computationally expensive for high-density fluid and polyatomic molecular fluids (I. Hanasaki & A. Nakatani, 2006), which is very common in the subsurface conditions.

Thus, an alternative method for the simulation of fluid flow is proposed in Figure 57. In this method, a constant pressure gradient is created and maintained efficiently outside of the digital kerogen segment using an external force field. However, the fluid flow inside the segment within the pores is not modified by the external force field. The molecular dynamics simulation box is shown in Figure 57. Specifically, the cuboid segment representing 3-D kerogen atomic structure is placed in between the two fluid reservoirs along the flow direction. The fluid is driven by an external force, which is only applied at the upstream end to a region (A), to enable flow through the porous kerogen medium.

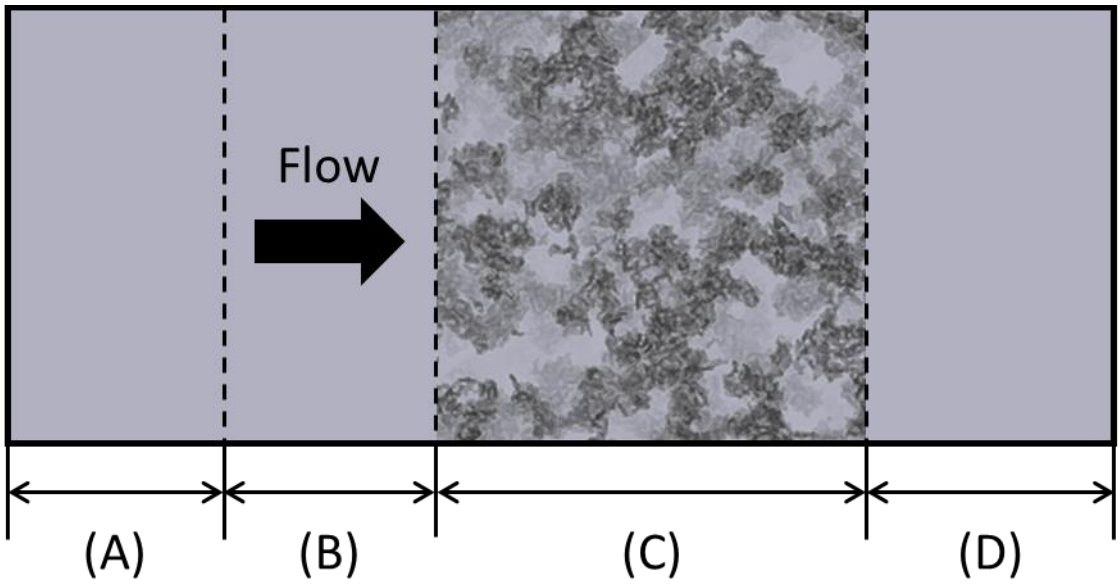

Figure 57. Molecular dynamics simulation box setup, showing an intersection parallel to flow direction, (A) External force driving region, (B) upstream free fluid region, (C) kerogen pore network region, (D) downstream free fluid region. Black areas are occupied by kerogen solid, light gray areas are occupied by reservoir fluid. The length of the edges of the kerogen block is around 30nm, depending on the simulation case.

First, with Grand Canonical Monte Carlo simulation, specific reservoir fluid can be filled into the entire simulation box, including the pores of the kerogen medium, at the desired subsurface temperature and pressure. Then, molecular dynamics simulation is run under NVT ensemble, under a constant external force uniformly applied to the region (A), to drive the fluid flow through the kerogen medium. When the fluid flow reaches steady-state, the pressure and concentration (or density) gradients of fluid can be maintained across the kerogen pore network.

The temperature of the system can be controlled by applying two separate thermostats, both applied on the fluid molecules only: one for all kerogen pores and one for fluid molecules in the other regions. The velocities of the molecules are only scaled at two directions which are perpendicular to flow direction. In this way, the temperature of the system can be controlled, the excess viscous heat generated in the porous media can be fully dissipated, with the dynamics along the flow direction untouched. During the simulation, periodic boundary conditions are applied to all x, y, and z directions.

Fluid molecules exiting from the right boundary of the region (D) re-enter the simulation box from the left boundary of the region (A). The length of the regions (A), (B) and (D) are set to 5nm, 5nm, and 5nm, respectively, the width and height of the simulation box are kept the same to the 3-D kerogen atomic structure. Thus, the permeability of the kerogen segment can be calculated using the values of the simulated flow rate and the pressure difference applied between region (B) and region (D).

In the simulations, pure methane is used to represent reservoir fluid, which is described by the OPLS-AA force field. Arithmetic mixing rule is used to calculate

Lennard-Jones interaction terms using Lorentz-Berthelot mixing rule (Equation 10). The cutoff distance is set to 10.0 Angstroms, the time step is set to 1.0 femtosecond.

The density profile of the fluid in Figure 58 shows that a stabilized pressure gradient can be maintained using the external force approach, and a stable steady-state flow can be reached after sufficient simulation time (Figure 59). Figure 60 shows that the simulation model generates a laminar flow field inside the porous structure. The permeability of the porous medium can be calculated using Equation 27, with ΔX taken as the thickness of the medium, ΔP as the pressure drop across the medium, $\overline{v_x}$ as the Darcy velocity along the flow direction, assuming methane's viscosity is unchanged across the segment.

$$\overline{v_x} = \frac{k}{\mu}\frac{\Delta P}{\Delta X} \qquad \textbf{Equation 27}$$

During the simulation, tail correction is ignored when calculating local pressures. Although ignoring this term underestimate the pressure especially when fluid density is high (Evans & Morriss, 1983) (which can be common in high pressure reservoir conditions), these error terms cancel each other out when calculating the pressure drop (Equation 27), given that ΔP is comparably smaller than the average pressure of the entire system.

To validate the effectiveness of the simplified molecular model, the size of the kerogen sample has to be as large as computationally possible to cover realistic mesopores characteristics, connectivity and pore size distribution (Adesida, Akkutlu, Resasco, & Rai, 2011; Feng & Akkutlu, 2015).

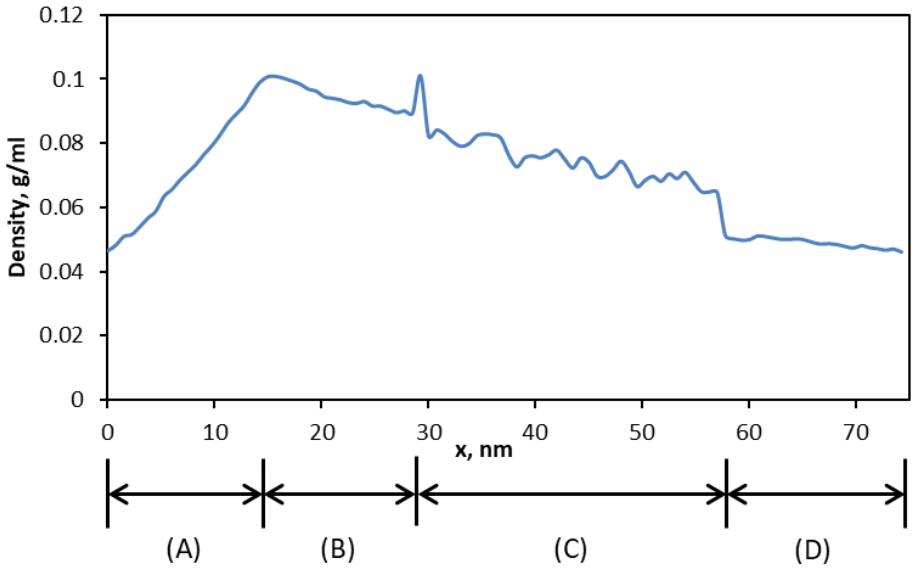

Figure 58. Density profile of methane flow stream through the pore network, along with the fluid flow direction, snapshot after simulation for 1ms. The external force field is applied to the 0~18nm region. The regions described in Figure 55 is marked with (A), (B), (C) and (D), respectively. Reprinted with permission from Springer Nature B.V., Copyright 2018.

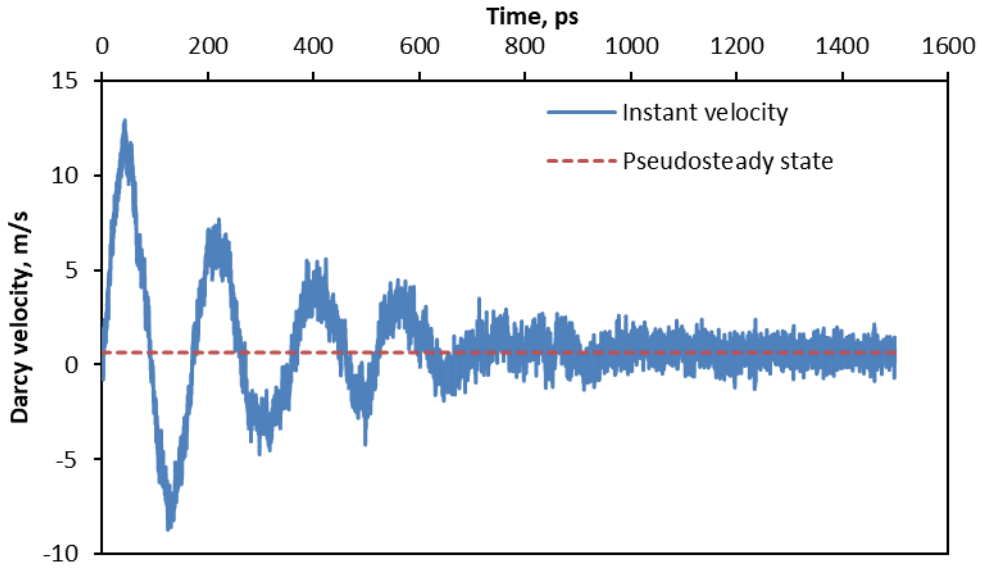

Figure 59. Darcy velocity vs. simulation time, showing a steady state flow can be eventually reached. Reprinted with permission from Springer Nature B.V., Copyright 2018.

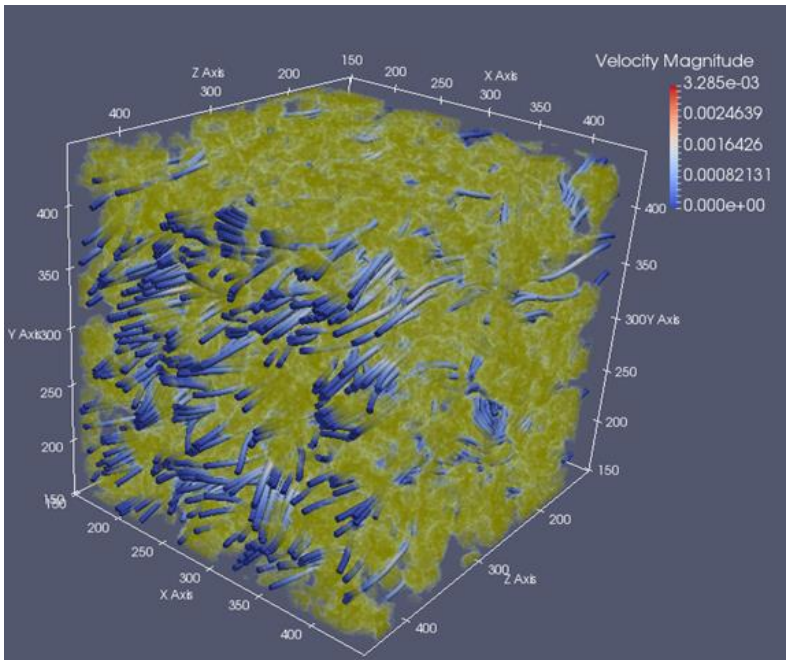

Figure 60. Streamlines showing fluid flow through porous media (length unit is Angstrom; velocity unit is relative value). Reprinted with permission from Springer Nature B.V., Copyright 2018.

Results

Using molecular dynamics simulations, the new simplified kerogen model can be evaluated, by comparing the simulation results from both the simplified model and the exact molecular model. The new molecular model is tested at different scenarios. For the simplified model, we assume that the positions of all kerogen atoms are fixed. Then, the effectiveness of the simplified molecular model can be validated by comparing it to the ones described by actual kerogen molecular structures. The results show the simplified model is a decent approximation against PCFF and CVFF force fields, see Figure 61. During the simulation, for atomic interactions not included in PCFF, CVFF force fields, the force field parameters from the most similar atomic interactions are used as replacements. If otherwise specified, all simulations are run under 353 K, 13.8 MPa subsurface conditions.

Hydrocarbon-bearing kerogens are of different types. Type I, II and III kerogen samples from previous research (Ungerer et al., 2015) are tested separately to compare the effectiveness of the simplified model on different geochemistry (Figure 62). Although the kerogen of each type has a different chemical structure, it turns out that the pore structure of the type is more important for the fluid flow. Varying sizes of the kerogen sample pores using the simplified molecular model is proven to be effective on a 3-D pore-network system with a significant number of mesopores (Figure 63). The

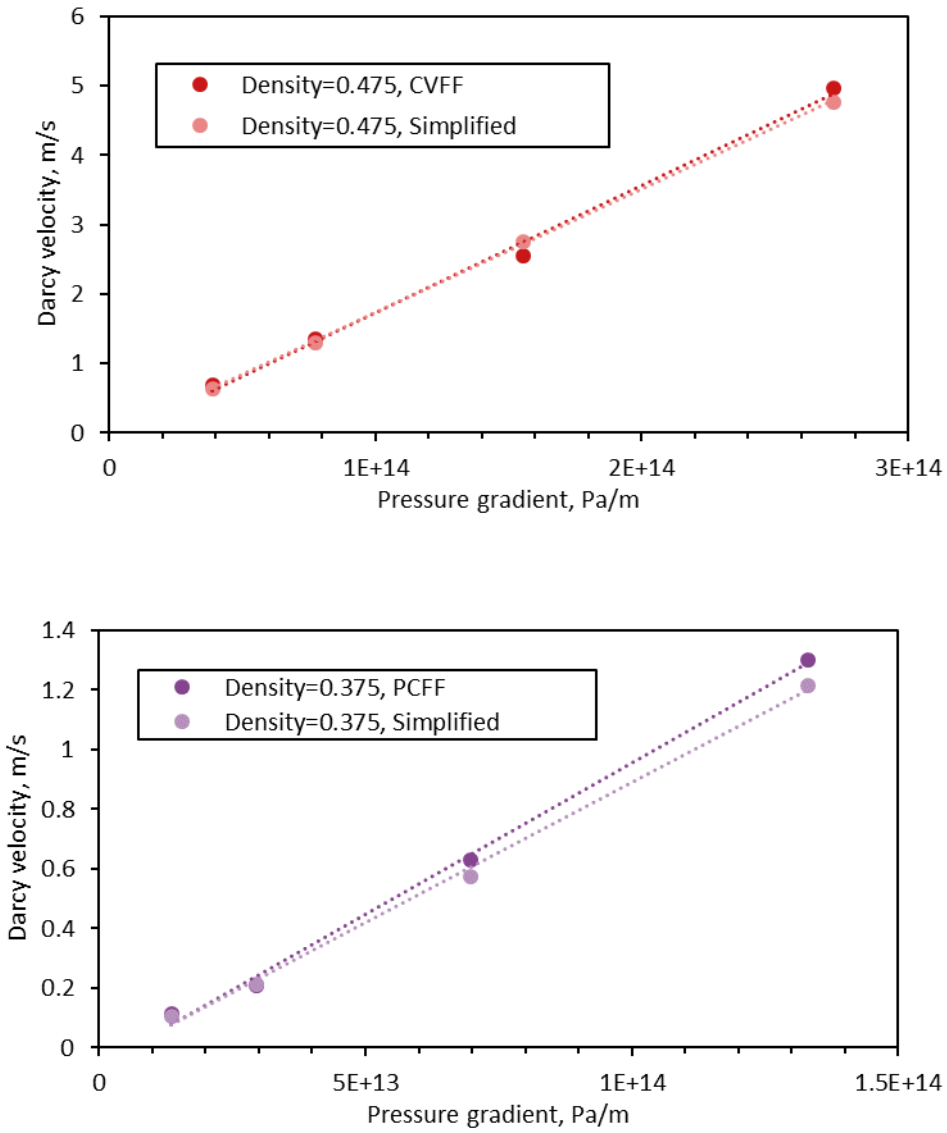

Figure 61. Flow simulation through porous kerogen, simplified force field vs exact force fields, Type II kerogen, the number on the legend is the density, with the unit of g/cm^3 . Reprinted with permission from Springer Nature B.V., Copyright 2018.

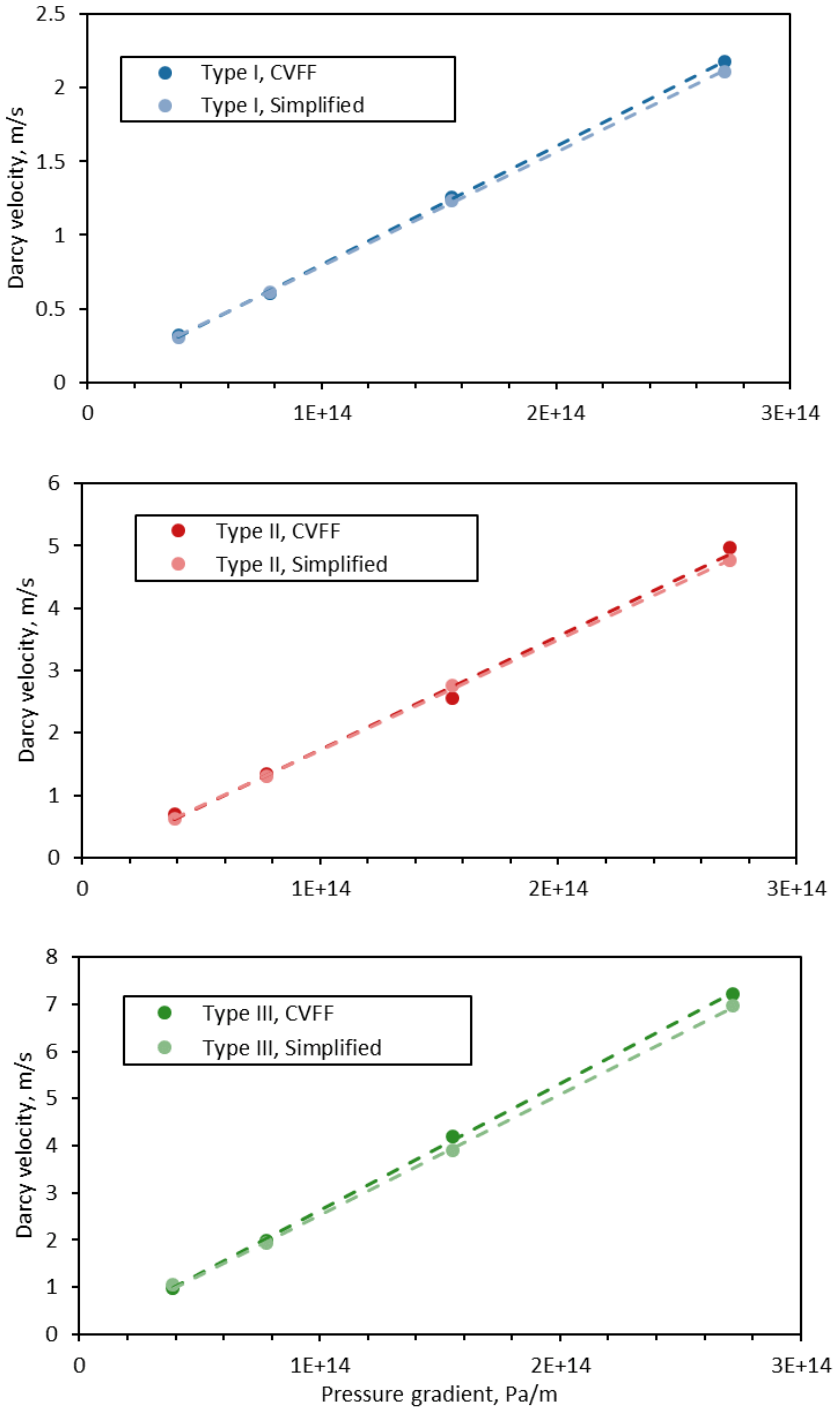

Figure 62. Flow simulation through porous kerogen, simplified force field vs exact force fields, varying kerogen geochemistry, CVFF force field, kerogen samples with similar pore size distributions are used for the simulation, the densities are 0.371g/cm^3, 0.475g/cm^3, 0.488g/cm^3, respectively. Reprinted with permission from Springer Nature B.V., Copyright 2018.

apparent porosity, permeability, and transport diffusivity data for the simplified model structures are calculated and listed in Table 3. Specifically, the apparent porosity is calculated based on the atomic radius data of the molecular structures, counting all void space in the kerogen skeleton, thus it is higher than experimentally measured porosity, whose value depends on the measurement method. Also, the transport diffusivities are of the same order of magnitude to the experimental measurement results using pulsed field gradient NMR method for samples of similar pore sizes (Y. L. Hu et al., 2016).

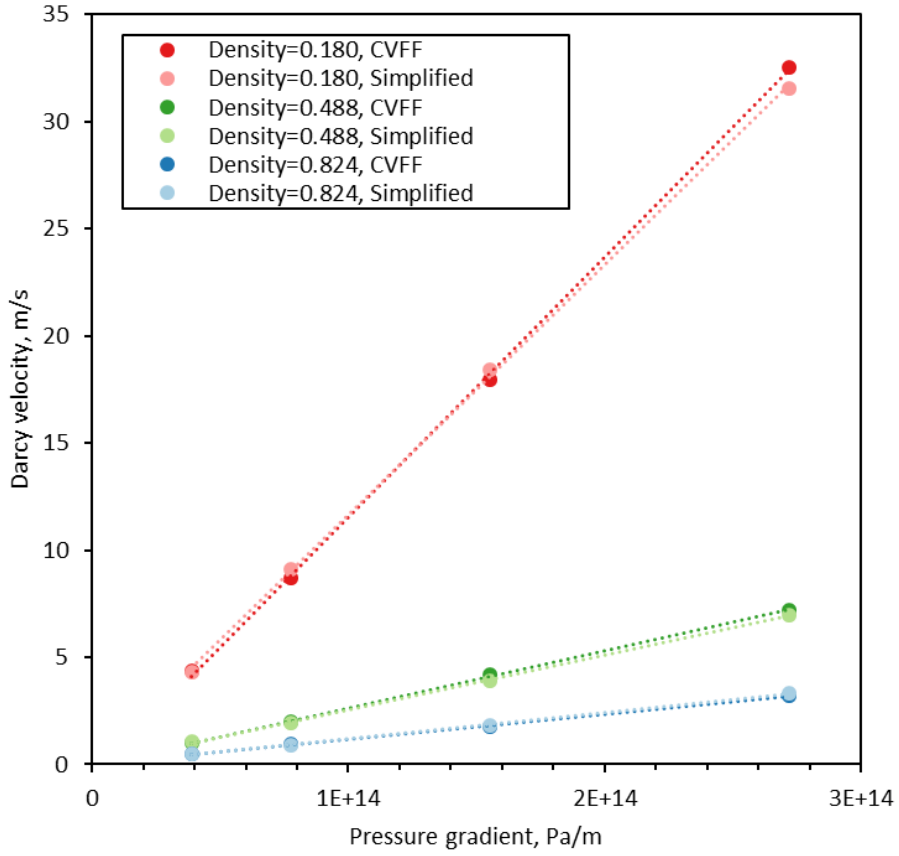

Figure 63. Flow simulation through porous kerogen, simplified force field vs exact force fields, using pore networks of different pore sizes, the number on the legend is the density, with a unit of g/cm^3 . Reprinted with permission from Springer Nature B.V., Copyright 2018.

Table 3. Porosity, permeability, and diffusivity of the structures above. Reprinted with permission from Springer Nature B.V., Copyright 2018.

Structure Name	Apparent porosity	Permeability, 10^{-4} *mD*	Transport Diffusivity, 10^{-6} m^2/s
Type I, 0.371 g/cm^3	64%	1.4	0.28
Type II, 0.475 g/cm^3	53%	3.5	0.71
Type III, 0.180 g/cm^3	86%	21.0	4.2
Type III, 0.488 g/cm^3	51%	4.4	0.89
Type III, 0.824 g/cm^3	14%	1.6	0.32

Discussion

Previous research (Chapter I) using single capillaries have discovered that the mobile adsorbed molecules in small pores could lead to enhanced fluid transport and greater permeability in kerogen (Fathi & Akkutlu, 2013; Feng & Akkutlu, 2015; Riewchotisakul, 2014) (Figure 34 and Figure 64). Based on the Hagen-Poiseuille equation with a non-zero boundary condition at the pore wall (Equation 28), the flow rate in a nanocapillary can be expressed as Equation 29 and Equation 30, which can be proved using molecular dynamics simulations, of methane carbon nanotube as the nanocapillary. An external force field is applied as the driving force, with the simulation setup and results shown in Figure 32 and Figure 64.

$$v_z(r) = -\frac{1}{4\mu}\frac{dp}{dz}(R^2 - r^2) + v_z(r = R) \qquad \textbf{Equation 28}$$

$$q_{total} = q_{H-P} + q_{surface} \qquad \textbf{Equation 29}$$

$$q_{total} = \frac{\pi\left(2r_{in,tube}^2 r_{in,ads}^2 - r_{in,ads}^4\right)}{8\mu}\frac{dP}{dL} + C_{sv}\frac{dP}{dL}\pi\left(r_{in,ads}^2\right) + \frac{\rho_{ads}}{\rho_{bulk}}C_{sv}\frac{dP}{dL}\pi\left(r_{in,\,tube}^2 - r_{in,ads}^2\right) \qquad \textbf{Equation 30}$$

in which C_{sv} is a constant parameter, indicating the contribution of surface flow enhancement.

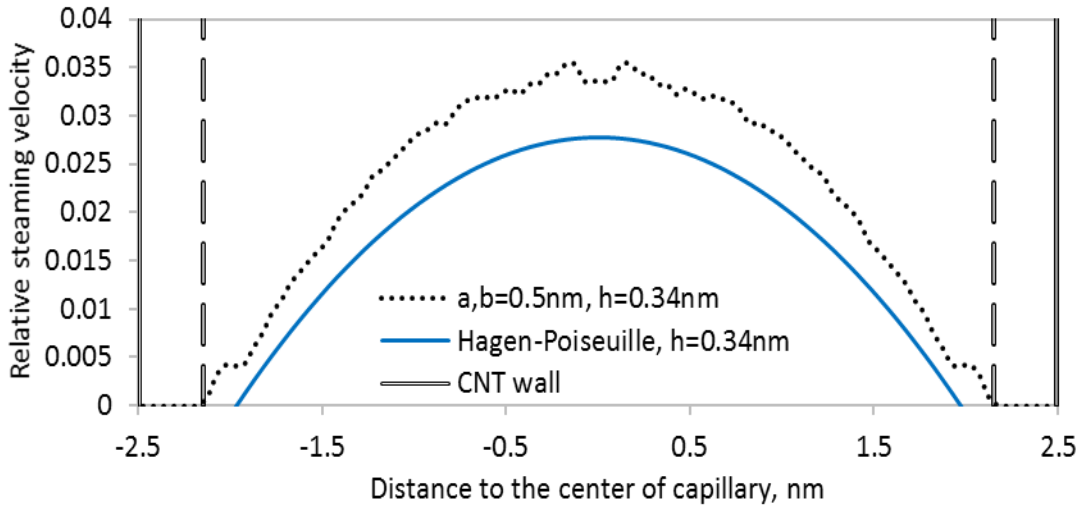

Figure 64. Velocity profile of methane across the nanocapillary, simulation is run at 353K, 13.8 MPa. (Feng & Akkutlu, 2015) The a, b and h are parameters describing the roughness of the capillaries. Reprinted with permission from Springer Nature B.V., Copyright 2018.

Using the magnified 3-D organic porous network, and the simplified kerogen pore network model, it can be shown that the surface transport enhancement due to mobile adsorbed molecules still exists in 3-D tortuous nanoporous media. Specifically, the statistical average velocity along the main flow direction of all the adsorbed molecules ($\bar{v}_{z,adsorbed}$) can be used as a measure for the surface transport enhancement effect. This would be the deviation from the traditional Hagen-Poiseuille flow. This velocity is calculated dynamically, by averaging the velocity of all adsorbed molecules throughout the simulation using (Equation 31).

$$\bar{v}_{z,adsorbed} = \frac{\int_0^t \sum v_{z,adsorbed}\, dt}{\int_0^t \sum n_{adsorbed}\, dt} \qquad \textbf{Equation 31}$$

If we assume Equation 29 is still valid for the 3-D case, the total Darcy velocity can be broken down into the contributions from the Hagen-Poiseuille flow and the surface transport (Equation 32).

$$q_{total} = q_{H-P} + q_{surface}$$

$$Av_{Darcy,\,total} = Av_{Darcy,H-P} + A\bar{v}_{z,adsorbed} \qquad \textbf{Equation 32}$$

$$v_{Darcy,\,total} = v_{Darcy,H-P} + \bar{v}_{z,adsorbed}$$

in which A is the cross-sectional area. $\bar{v}_{z,adsorped}$ can be calculated using the trajectory information from molecular dynamics simulations.

Figure 65 shows that a significant amount of flow in the nanopores is contributed by the surface enhancement phenomenon. As a result, the permeability of the organic nanopore medium is much higher than that predicted using the conventional petrophysics and fluid dynamics. Our results show that the contribution of the adsorbed phase to the total mass flux is more significant when the applied pressure gradient is low.

To simulate steady-state flow, it is necessary to allow enough time for the system to fully stabilize. The characteristic time required to establish a steady-state flow system is $t_d = \frac{L^2}{D}$, where L is the characteristic length and D is diffusivity. As a result, limiting the time spent on establishing a pseudo-steady state flow is crucial for simulating larger pore network models. It could be achieved by setting a proper initial streaming velocity and density distribution for all fluid molecules. And this initial guess can be determined from existing simulation results.

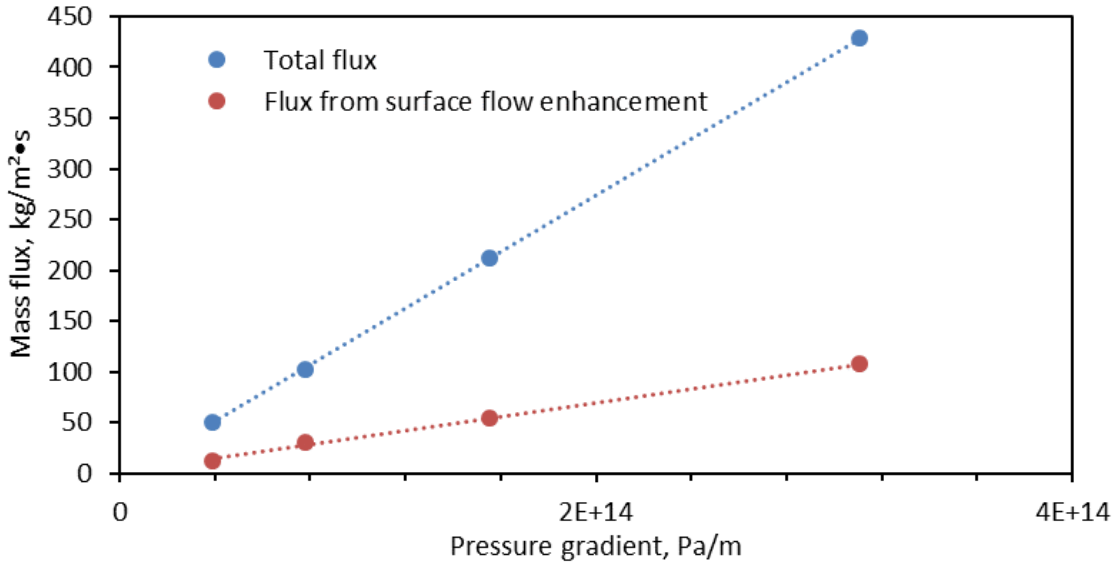

Figure 65. Darcy velocity of all fluid molecules vs. Darcy velocity of adsorbed molecules only, calculated from the simulation results based on Figure 61-A, with the exact model being used. The difference between the two curves is the flow contribution with the conventional Hagen-Poiseuille equation. Reprinted with permission from Springer Nature B.V., Copyright 2018.

In addition, the variance of the sample is proportional to the sample size, given all sample data are from the same distribution (pseudo-steady state flow). As a result, despite increasing the size of the pore network increases the computational cost required for each time step, it also reduces the number of time steps to get a simulated permeability with acceptable precision. The overall computational cost should stay the same regardless of the pore network model size (after the system reaches pseudo-steady state). To further reduce computational complexity, kerogen molecules far from the surface can be set to frozen during the simulation, which reduces the number of effective molecules to $O(L^2)$. In sum, the overall computational complexity is $O(L^4)$, limited by the transient period, and it can be potentially optimized by further algorithm design. Alternatively, when the system size is large and uniform enough, it is possible to build a

transient GRMD diffusion model (Figure 27) to calculate diffusivity/permeability and to make better use of the data in the transient stage.

Thanks to parallel computing and GPU acceleration technologies, today supercomputers can now handle molecular simulations at large scale. GPU has superior power in solving matrix equations than CPU, which is usable for most Molecular Dynamics simulations. In this work, because we need to theoretically investigate the contribution of surface flow enhancement by dynamically identifying the adsorbed molecules and frequent property computations, which requires frequent data transfer from GPU to CPU, the speedup using GPU will be limited. However, in real industrial applications which do less property computations, the speedup gained using GPU will be significant.

Another challenge is to reduce the pressure gradient used in the simulation to a smaller, more realistic value. Because of statistical variation, longer simulation is required to obtain a reliable data set to determine pressure gradient and flux, as pressure gradient goes smaller. Currently, due to limited computational capacity, the pressure gradient applied to the simulation system is at the scale of 10^{13} Pa/m, which is much higher than those in real gas reservoirs. This can be fixed by using more computational power.

Moreover, it usually requires samples with sizes in micrometers to cover the complete pore size distribution and the other pore network characteristics. To effectively reduce computational cost, Monte Carlo sampling can be used. The whole system can be divided into smaller blocks at the size of around 100 nm, then we only perform

molecular modeling and simulations for some randomly selected blocks. Then the petrophysical properties of the sample can be calculated statistically. Compared to directly simulating the whole system at one time, Monte Carlo allows simulations with limited computational resources, and uncertainty can be reduced by simulating more randomly selected samples.

The kerogen rock samples are usually measured at laboratory temperature and pressure, which is different from the subsurface conditions. Thus, the actual porous structure subsurface can be different from what is measured in the lab, due to thermal expansion and compaction. This can be corrected with the coefficient of thermal expansion and compressibility, either measured in the laboratory or simulated with molecular simulation, prior to populating the porous structure with the simplified molecular model.

This work focuses on the validation of high pressure, supercritical fluid. Although this simplified model work for this fluid, further investigation into the low pressure, high Knudsen number fluid are meaningful.

In this chapter, we proposed a simplified effective kerogen molecular model for simulating reservoir fluid transport, with accuracy comparable to the exact kerogen models. Once the pore structure is obtained from 3-D TEM tomography, together with the basic geochemical information of kerogen, we showed that the kerogen molecular model can be built. Using molecular dynamics simulation, accurate transport parameters can be simulated for reservoir engineering applications. Our results indicate the presence of a mobile adsorbed phase in the kerogen pore network during the steady-state flow of

methane in the kerogen segment. This result independently confirms the previous flow simulations using single-capillary with smooth and rough surfaces.

CHAPTER IV

SUMMARY AND PROSPECT

In this study, we first explored the transport phenomenon in kerogen mesopores using carbon nanotubes and their derivatives as analogies and proved the existence of surface transport under various conditions; then we provided a unique method to convert the 3-D kerogen porous network from TEM tomography into a simplified molecular model, without sacrificing simulation accuracy. The brief methodology is illustrated in Figure 66. The methods from this study can be used to evaluate novel oilfield technologies including CO_2 fracturing, huff & puff to enhance hydrocarbon recovery.

Despite our current 3-D modeling approach only used kerogen sample size of ~100nm, thanks to the potential future improvement in parallel computing, especially

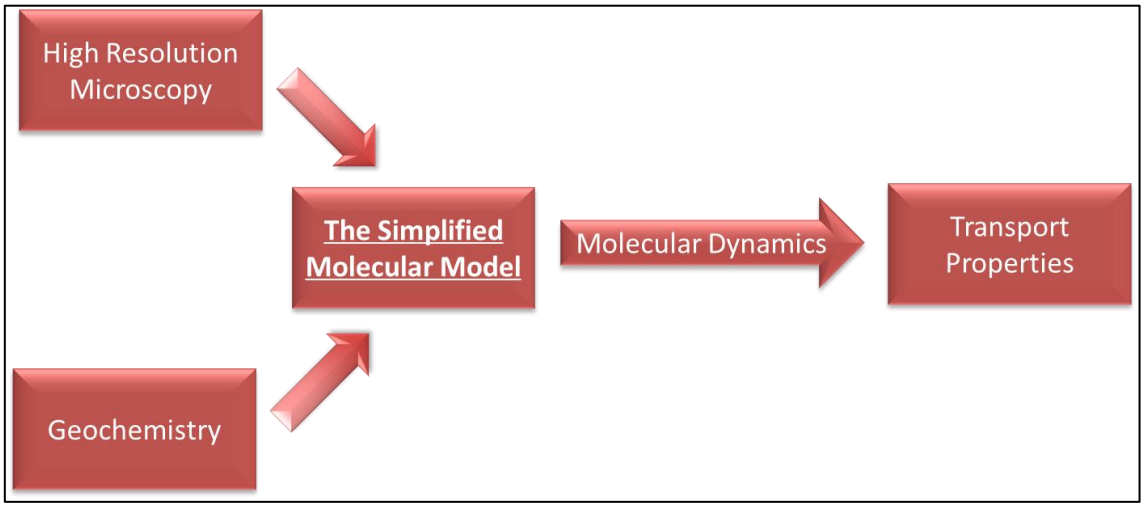

Figure 66. Methodology of building the simplified 3-D kerogen molecular model for molecular dynamics flow simulation

GPU accelerated computing, together with better algorithm design to minimize the transient period, it is possible to scale up this approach to larger pore network samples (Figure 67). This also allows simulations using lower pressure gradients by using longer simulation time. For samples even larger, multiple random segments from the entire sample can be extracted to build models and to run simulations, thus a reasonable estimate of the permeability of the large sample can be achieved by calculating the mean and variance.

Moreover, once a better understanding of the kerogen maturation process is achieved, if there is limited TEM tomography available, one can always make assumptions of the pore connectivity, and come up with a pore network generating algorithm, and randomly generates a series of pore network molecular models to run molecular simulation with. In this way, a reasonable estimation of the permeability can also be achieved.

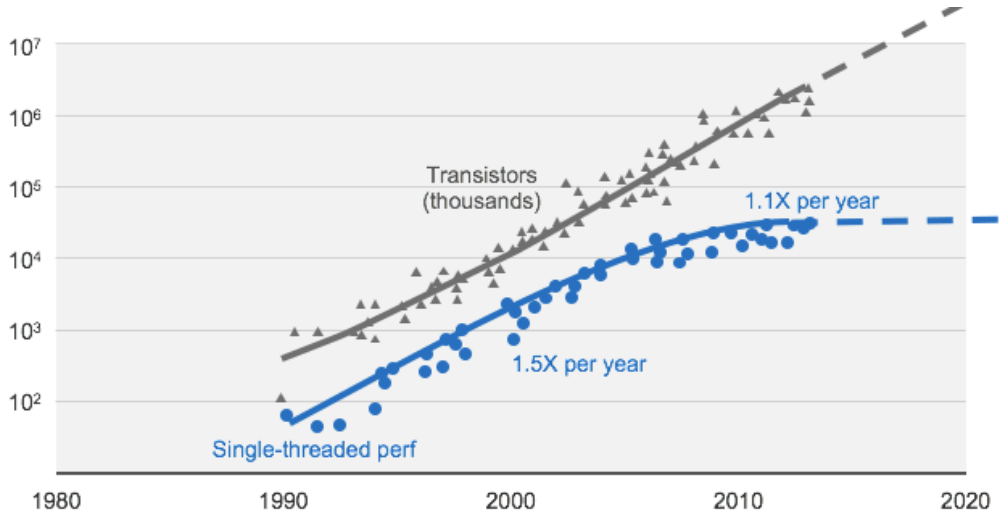

Figure 67. Forty years of microprocessor trend data (with y-axis to be floating point calculation speed), showing the advantage of GPU over CPU. (Nvidia, 2018)

In the future, it is meaningful to use more experimental results to better validate the modeling and simulation work, and to apply the same methodology to inorganic nanopores. The 3-D models can be further tested and modified to match transport simulation for additional components and their mixtures, especially polar molecules (e.g. H_2O). It can also be potentially improved to match adsorption and phase behavior prediction. Another possible work is to use the 3-D simulation results and experimental pore-size characterization results to better parameterize the 1-D model.

REFERENCES

Adesida, A., Akkutlu, I., Resasco, D., & Rai, C. (2011). Kerogen pore size distribution of Barnett shale using DFT analysis and Monte Carlo simulations. Paper SPE 147397 presented during the SPE annual technical conference and exhibition held in Denver, Colorado, 30 October–2 November. *DOI: http://dx. doi. org/10.2118/147397-MS*.

Akkutlu, I. Y., & Didar, B. R. (2013). *Pore-size Dependence of Fluid Phase Behavior and Properties in Organic-Rich Shale Reservoirs*. Paper presented at the SPE International Symposium on Oilfield Chemistry.

Akkutlu, I. Y., & Fathi, E. Multiscale Gas Transport in Shales With Local Kerogen Heterogeneities. doi:10.2118/146422-PA

Albo, S. E., Broadbelt, L. J., & Snurr, R. Q. (2006). Multiscale modeling of transport and residence times in nanostructured membranes. *AIChE Journal, 52*(11), 3679-3687. doi:10.1002/aic.10998

Allinger, N. (1976). Calculation of molecular structure and energy by force-field methods *Advances in physical organic chemistry* (Vol. 13, pp. 1-82): Elsevier.

Ambrose, R. J., Hartman, R. C., Diaz Campos, M., Akkutlu, I. Y., & Sondergeld, C. (2010). *New pore-scale considerations for shale gas in place calculations*. Paper presented at the SPE Unconventional Gas Conference.

Andra, H., Combaret, N., Dvorkin, J., Glatt, E., Han, J., Kabel, M., . . . Zhan, X. (2013a). Digital rock physics benchmarks-Part I: Imaging and segmentation. *Computers & Geosciences, 50*, 25-32. doi:10.1016/j.cageo.2012.09.005

Andra, H., Combaret, N., Dvorkin, J., Glatt, E., Han, J., Kabel, M., . . . Zhan, X. (2013b). Digital rock physics benchmarks-part II: Computing effective properties. *Computers & Geosciences, 50*, 33-43. doi:10.1016/j.cageo.2012.09.008

Arya, G., Chang, H. C., & Maginn, E. J. (2001). A critical comparison of equilibrium, non-equilibrium and boundary-driven molecular dynamics techniques for

studying transport in microporous materials. *Journal of Chemical Physics, 115*(17), 8112-8124. doi:Doi 10.1063/1.1407002

Balach, J., Soldera, F., Acevedo, D. F., Mucklich, F., & Barbero, C. A. (2013). A Direct and Quantitative Three-Dimensional Reconstruction of the Internal Structure of Disordered Mesoporous Carbon with Tailored Pore Size. *Microscopy and Microanalysis, 19*(3), 745-750. doi:10.1017/S1431927613000238

Bhatnagar, P. L., Gross, E. P., & Krook, M. (1954). A Model for Collision Processes in Gases .1. Small Amplitude Processes in Charged and Neutral One-Component Systems. *Physical Review, 94*(3), 511-525. doi:DOI 10.1103/PhysRev.94.511

Bhattacharya, S., & Gubbins, K. E. (2006). Fast method for computing pore size distributions of model materials. *Langmuir, 22*(18), 7726-7731. doi:10.1021/la052651k

Blunt, M. J. (2001). Flow in porous media - pore-network models and multiphase flow. *Current Opinion in Colloid & Interface Science, 6*(3), 197-207. doi:Doi 10.1016/S1359-0294(01)00084-X

Bousige, C., Botan, A., Ulm, F. J., Pellenq, R. J. M., & Coasne, B. (2015). Optimized molecular reconstruction procedure combining hybrid reverse Monte Carlo and molecular dynamics. *Journal of Chemical Physics, 142*(11). doi:Artn 114112 10.1063/1.4914921

Bousige, C., Ghimbeu, C. M., Vix-Guterl, C., Pomerantz, A. E., Suleimenova, A., Vaughan, G., . . . Coasne, B. (2016). Realistic molecular model of kerogen's nanostructure. *Nature Materials, 15*(5), 576-+. doi:10.1038/Nmat4541

Brooks, B. R., Bruccoleri, R. E., Olafson, B. D., States, D. J., Swaminathan, S., & Karplus, M. (1983). Charmm - a Program for Macromolecular Energy, Minimization, and Dynamics Calculations. *Journal of Computational Chemistry, 4*(2), 187-217. doi:DOI 10.1002/jcc.540040211

Brown, G. P., Dinardo, A., Cheng, G. K., & Sherwood, T. K. (1946). The Flow of Gases in Pipes at Low Pressures. *Journal of Applied Physics, 17*(10), 802-813. doi:Doi 10.1063/1.1707647

Bulba, K. A., & Krouskop, P. E. (2009). Compositional variety complicates processing plans for US shale gas. *Oil & Gas Journal, 107*(10), 50-55.

Cai, Q., Buts, A., Seaton, N. A., & Biggs, M. J. (2008). A pore network model for diffusion in nanoporous carbons: Validation by molecular dynamics simulation. *Chemical Engineering Science, 63*(13), 3319-3327. doi:10.1016/j.ces.2008.03.032

Chalmers, G. R., Bustin, R. M., & Power, I. M. (2012). Characterization of gas shale pore systems by porosimetry, pycnometry, surface area, and field emission scanning electron microscopy/transmission electron microscopy image analyses: Examples from the Barnett, Woodford, Haynesville, Marcellus, and Doig units. *Aapg Bulletin, 96*(6), 1099-1119. doi:10.1306/10171111052

Chen, L., Zhang, L., Kang, Q. J., Viswanathan, H. S., Yao, J., & Tao, W. Q. (2015). Nanoscale simulation of shale transport properties using the lattice Boltzmann method: permeability and diffusivity. *Scientific Reports, 5*. doi:ARTN 8089 10.1038/srep08089

Chen, S., & Doolen, G. D. (1998). Lattice Boltzmann method for fluid flows. *Annual Review of Fluid Mechanics, 30*, 329-364. doi:DOI 10.1146/annurev.fluid.30.1.329

Cheng, C. Y., & Bowers, C. R. (2007). Direct observation of atoms entering and exiting L-Alanyl-L-valine nanotubes by hyperpolarized xenon-129 NMR. *Journal of the American Chemical Society, 129*(45), 13997-14002. doi:10.1021/ja074563n

Chib, S., & Greenberg, E. (1995). Understanding the Metropolis-Hastings Algorithm. *American Statistician, 49*(4), 327-335. doi:Doi 10.2307/2684568

Cocco, A. P., Nelson, G. J., Harris, W. M., Nakajo, A., Myles, T. D., Kiss, A. M., . . . Chiu, W. K. S. (2013). Three-dimensional microstructural imaging methods for energy materials. *Physical Chemistry Chemical Physics, 15*(39), 16377-16407. doi:10.1039/c3cp52356j

Collell, J., Galliero, G., Gouth, F., Montel, F., Pujol, M., Ungerer, P., & Yiannourakou, M. (2014). Molecular simulation and modelisation of methane/ethane mixtures

adsorption onto a microporous molecular model of kerogen under typical reservoir conditions. *Microporous and Mesoporous Materials, 197*, 194-203. doi:10.1016/j.micromeso.2014.06.016

Collell, J., Galliero, G., Vermorel, R., Ungerer, P., Yiannourakou, M., Montel, F., & Pujol, M. (2015). Transport of Multicomponent Hydrocarbon Mixtures in Shale Organic Matter by Molecular Simulations. *Journal of Physical Chemistry C, 119*(39), 22587-22595. doi:10.1021/acs.jpcc.5b07242

Collell, J., Ungerer, P., Galliero, G., Yiannourakou, M., Montel, F., & Pujol, M. (2014). Molecular Simulation of Bulk Organic Matter in Type II Shales in the Middle of the Oil Formation Window. *Energy & Fuels, 28*(12), 7457-7466. doi:10.1021/ef5021632

Cui, X., Bustin, A. M. M., & Bustin, R. M. (2009). Measurements of gas permeability and diffusivity of tight reservoir rocks: different approaches and their applications. *Geofluids, 9*(3), 208-223. doi:10.1111/j.1468-8123.2009.00244.x

Darden, T., York, D., & Pedersen, L. (1993). Particle Mesh Ewald - an N.Log(N) Method for Ewald Sums in Large Systems. *Journal of Chemical Physics, 98*(12), 10089-10092. doi:Doi 10.1063/1.464397

Dauberosguthorpe, P., Roberts, V. A., Osguthorpe, D. J., Wolff, J., Genest, M., & Hagler, A. T. (1988). Structure and Energetics of Ligand-Binding to Proteins - Escherichia-Coli Dihydrofolate Reductase Trimethoprim, a Drug-Receptor System. *Proteins-Structure Function and Genetics, 4*(1), 31-47. doi:DOI 10.1002/prot.340040106

Dodson, B. W. (1987). Development of a Many-Body Tersoff-Type Potential for Silicon. *Physical Review B, 35*(6), 2795-2798. doi:DOI 10.1103/PhysRevB.35.2795

Donohue, M. D., & Aranovich, G. L. (1998). Classification of Gibbs adsorption isotherms. *Advances in Colloid and Interface Science, 76*, 137-152. doi:Doi 10.1016/S0001-8686(98)00044-X

Espanol, P., & Warren, P. (1995). Statistical-Mechanics of Dissipative Particle Dynamics. *Europhysics Letters, 30*(4), 191-196. doi:Doi 10.1209/0295-5075/30/4/001

Estrada, J. M., & Bhamidimarri, R. (2016). A review of the issues and treatment options for wastewater from shale gas extraction by hydraulic fracturing. *Fuel, 182*, 292-303. doi:10.1016/j.fuel.2016.05.051

Etminan, S. R., Javadpour, F., Maini, B. B., & Chen, Z. X. (2014). Measurement of gas storage processes in shale and of the molecular diffusion coefficient in kerogen. *International Journal of Coal Geology, 123*, 10-19. doi:10.1016/j.coal.2013.10.007

Evans, D. J., & Holian, B. L. (1985). The Nose-Hoover Thermostat. *Journal of Chemical Physics, 83*(8), 4069-4074. doi:Doi 10.1063/1.449071

Evans, D. J., & Morriss, G. P. (1983). Isothermal Isobaric Molecular-Dynamics. *Chemical Physics, 77*(1), 63-66. doi:Doi 10.1016/0301-0104(83)85065-4

Falk, K., Coasne, B., Pellenq, R., Ulm, F. J., & Bocquet, L. (2015). Subcontinuum mass transport of condensed hydrocarbons in nanoporous media. *Nature Communications, 6*. doi:ARTN 6949

10.1038/ncomms7949

Falk, K., Pellenq, R., Ulm, F. J., & Coasne, B. (2015). Effect of Chain Length and Pore Accessibility on Alkane Adsorption in Kerogen. *Energy & Fuels, 29*(12), 7889-7896. doi:10.1021/acs.energyfuels.5b02015

Fathi, E., & Akkutlu, I. Y. *Macro-kinetics of Matrix Gas Release and its Influence on Coalbed Methane Flow and Production*.

Fathi, E., & Akkutlu, I. Y. (2009). Matrix heterogeneity effects on gas transport and adsorption in coalbed and shale gas reservoirs. *Transport in Porous Media, 80*(2), 281-304.

Fathi, E., & Akkutlu, I. Y. (2013). Lattice Boltzmann Method for Simulation of Shale Gas Transport in Kerogen. *Spe Journal, 18*(1), 27-37.

Fathi, E., & Akkutlu, I. Y. (2014). Multi-component gas transport and adsorption effects during CO2 injection and enhanced shale gas recovery. *International Journal of Coal Geology, 123*, 52-61. doi:10.1016/j.coal.2013.07.021

FEI. (2018). Confidence: Generating Reliable Data, Faster. Retrieved from https://www.fei.com/software/pergeos-for-oil-gas/

Feng, F., & Akkutlu, I. Y. (2015). *Flow of hydrocarbons in nanocapillary: A non-equilibrium molecular dynamics study*. Paper presented at the SPE Asia Pacific Unconventional Resources Conference and Exhibition.

Firdaus, G., & Heidari, Z. (2015). *Quantifying Electrical Resistivity of Isolated Kerogen from Organic-Rich Mudrocks using Laboratory Experiments*. Paper presented at the SPE Annual Technical Conference and Exhibition.

Firouzi, M., Alnoaimi, K., Kovscek, A., & Wilcox, J. (2014). Klinkenberg effect on predicting and measuring helium permeability in gas shales. *International Journal of Coal Geology, 123*, 62-68. doi:10.1016/j.coal.2013.09.006

Firouzi, M., Rupp, E. C., Liu, C. W., & Wilcox, J. (2014). Molecular simulation and experimental characterization of the nanoporous structures of coal and gas shale. *International Journal of Coal Geology, 121*, 123-128. doi:10.1016/j.coal.2013.11.003

Firouzi, M., & Wilcox, J. (2012). Molecular modeling of carbon dioxide transport and storage in porous carbon-based materials. *Microporous and Mesoporous Materials, 158*, 195-203. doi:10.1016/j.micromeso.2012.02.045

Firouzi, M., & Wilcox, J. (2013). Slippage and viscosity predictions in carbon micropores and their influence on CO2 and CH4 transport. *Journal of Chemical Physics, 138*(6). doi:Artn 064705

10.1063/1.4790658

Frenkel, D., & Smit, B. (2002). *Understanding molecular simulations: from algorithms to applications*. Retrieved from

Frentrup, H., Avendaño, C., Horsch, M., Salih, A., & Müller, E. A. (2012). Transport diffusivities of fluids in nanopores by non-equilibrium molecular dynamics

simulation. *Molecular Simulation, 38*(7), 540-553. doi:10.1080/08927022.2011.636813

Groen, J. C., Peffer, L. A. A., & Perez-Ramirez, J. (2003). Pore size determination in modified micro- and mesoporous materials. Pitfalls and limitations in gas adsorption data analysis. *Microporous and Mesoporous Materials, 60*(1-3), 1-17. doi:10.1016/S1387-1811(03)00339-1

Groot, R. D., & Warren, P. B. (1997). Dissipative particle dynamics: Bridging the gap between atomistic and mesoscopic simulation. *Journal of Chemical Physics, 107*(11), 4423-4435. doi:Doi 10.1063/1.474784

Hahn, K., Karger, J., & Kukla, V. (1996). Single-file diffusion observation. *Physical Review Letters, 76*(15), 2762-2765. doi:DOI 10.1103/PhysRevLett.76.2762

Hanasaki, I., & Nakatani, A. (2006). Flow structure of water in carbon nanotubes: poiseuille type or plug-like? *Journal of Chemical Physics, 124*(14), 144708. doi:10.1063/1.2187971

Hanasaki, I., & Nakatani, A. (2006). Fluidized piston model for molecular dynamics simulations of hydrodynamic flow. *Modelling and Simulation in Materials Science and Engineering, 14*(5), S9.

Hartman, R. C., Ambrose, R. J., Akkutlu, I. Y., & Clarkson, C. R. *Shale Gas-in-Place Calculations Part II - Multicomponent Gas Adsorption Effects*.

Hautman, J., & Klein, M. L. (1992). An Ewald Summation Method for Planar Surfaces and Interfaces. *Molecular Physics, 75*(2), 379-395. doi:Doi 10.1080/00268979200100301

Heffelfinger, G. S., & Swol, F. v. (1994). Diffusion in Lennard-Jones fluids using dual control volume grand canonical molecular dynamics simulation (DCV-GCMD). *The Journal of Chemical Physics, 100*(10), 7548. doi:10.1063/1.466849

Hess, B., Kutzner, C., van der Spoel, D., & Lindahl, E. (2008). GROMACS 4: Algorithms for highly efficient, load-balanced, and scalable molecular simulation. *Journal of Chemical Theory and Computation, 4*(3), 435-447. doi:10.1021/ct700301q

Ho, T. A., Criscenti, L. J., & Wang, Y. F. (2016). Nanostructural control of methane release in kerogen and its implications to wellbore production decline. *Scientific Reports, 6*. doi:ARTN 28053

10.1038/srep28053

Hospital, A., Goñi, J. R., Orozco, M., & Gelpí, J. L. (2015). Molecular dynamics simulations: advances and applications. *Advances and applications in bioinformatics and chemistry: AABC, 8*, 37.

Hu, Q. H., Ewing, R. P., & Dultz, S. (2012). Low pore connectivity in natural rock. *Journal of Contaminant Hydrology, 133*, 76-83. doi:10.1016/j.jconhyd.2012.03.006

Hu, Y. L., Zhang, Q., Li, M. R., Pan, X. L., Fang, B., Zhuang, W., . . . Bao, X. H. (2016). Facilitated Diffusion of Methane in Pores with a Higher Aromaticity. *Journal of Physical Chemistry C, 120*(35), 19885-19889. doi:10.1021/acs.jpcc.6b07500

Humphrey, W., Dalke, A., & Schulten, K. (1996). VMD: Visual molecular dynamics. *Journal of Molecular Graphics & Modelling, 14*(1), 33-38. doi:Doi 10.1016/0263-7855(96)00018-5

Hwang, M. J., Stockfisch, T. P., & Hagler, A. T. (1994). Derivation of Class-Ii Force-Fields .2. Derivation and Characterization of a Class-Ii Force-Field, Cff93, for the Alkyl Functional-Group and Alkane Molecules. *Journal of the American Chemical Society, 116*(6), 2515-2525. doi:DOI 10.1021/ja00085a036

Javadpour, F. (2009). Nanopores and Apparent Permeability of Gas Flow in Mudrocks (Shales and Siltstone). *Journal of Canadian Petroleum Technology, 48*(8), 16-21. doi:Doi 10.2118/09-08-16-Da

Javadpour, F., Fisher, D., & Unsworth, M. (2007). Nanoscale gas flow in shale gas Sediments. *Journal of Canadian Petroleum Technology, 46*(10), 55-61. doi:Doi 10.2118/07-10-06

Jorgensen, W. L., Maxwell, D. S., & Tirado-Rives, J. (1996). Development and testing of the OPLS all-atom force field on conformational energetics and properties of

organic liquids. *Journal of the American Chemical Society, 118*(45), 11225-11236.

Jorgensen, W. L., Maxwell, D. S., & TiradoRives, J. (1996). Development and testing of the OPLS all-atom force field on conformational energetics and properties of organic liquids. *Journal of the American Chemical Society, 118*(45), 11225-11236. doi:DOI 10.1021/ja9621760

Kaminski, G. A., Friesner, R. A., Tirado-Rives, J., & Jorgensen, W. L. (2001). Evaluation and reparametrization of the OPLS-AA force field for proteins via comparison with accurate quantum chemical calculations on peptides. *The Journal of Physical Chemistry B, 105*(28), 6474-6487.

Kapteijn, F., Bakker, W. J., Zheng, G., Poppe, J., & Moulijn, J. A. (1995). Permeation and separation of light hydrocarbons through a silicalite-1 membrane: Application of the generalized Maxwell-Stefan equations. *The Chemical Engineering Journal and The Biochemical Engineering Journal, 57*(2), 145-153.

Kärger, J., & Ruthven, D. M. (1992). *Diffusion in zeolites and other microporous solids*: Wiley New York.

Kettering, C. F., Shutts, L. W., & Andrews, D. H. (1930). A representation of the dynamic properties of molecules by mechanical models. *Physical Review, 36*(3), 0531-0543. doi:DOI 10.1103/PhysRev.36.531

Klinkenberg, L. (1941). *The permeability of porous media to liquids and gases.* Paper presented at the Drilling and production practice.

Koppel, H., Domcke, W., & Cederbaum, L. S. (1984). Multimode Molecular-Dynamics Beyond the Born-Oppenheimer Approximation. *Advances in Chemical Physics, 57*, 59-246.

Kou, R., Alafnan, S. F. K., & Akkutlu, I. Y. (2017). Multi-scale Analysis of Gas Transport Mechanisms in Kerogen. *Transport in Porous Media, 116*(2), 493-519. doi:10.1007/s11242-016-0787-7

Krishna, R. (2000). Diffusion of binary mixtures in zeolites: molecular dynamics simulations versus Maxwell–Stefan theory. *Chemical Physics Letters, 326*(5), 477-484.

Kruk, M., Jaroniec, M., & Sayari, A. (1997). Application of large pore MCM-41 molecular sieves to improve pore size analysis using nitrogen adsorption measurements. *Langmuir, 13*(23), 6267-6273. doi:DOI 10.1021/la970776m

Kuila, U., & Prasad, M. (2013). Specific surface area and pore-size distribution in clays and shales. *Geophysical Prospecting, 61*(2), 341-362. doi:10.1111/1365-2478.12028

Lee, T., Bocquet, L., & Coasne, B. (2016). Activated desorption at heterogeneous interfaces and long-time kinetics of hydrocarbon recovery from nanoporous media. *Nature Communications, 7*. doi:ARTN 11890

10.1038/ncomms11890

Lemak, A. S., & Balabaev, N. K. (1994). On the Berendsen Thermostat. *Molecular Simulation, 13*(3), 177-187. doi:Doi 10.1080/08927029408021981

Liang, Z., & Tsai, H.-L. (2012). A method to generate pressure gradients for molecular simulation of pressure-driven flows in nanochannels. *Microfluidics and Nanofluidics, 13*(2), 289-298. doi:10.1007/s10404-012-0960-4

Liang, Z., & Tsai, H. L. (2012). A method to generate pressure gradients for molecular simulation of pressure-driven flows in nanochannels. *Microfluidics and Nanofluidics, 13*(2), 289-298. doi:10.1007/s10404-012-0960-4

Lin, J., & Murad, S. (2001). A computer simulation study of the separation of aqueous solutions using thin zeolite membranes. *Molecular Physics, 99*(14), 1175-1181.

Liu, K., Sun, J. M., Gu, M., Liu, H. T., & Chen, X. Y. (2017). A new method for estimating the free-to-adsorbed ratio in shale gas reservoirs using acoustic amplitude attenuation and porosity. *Journal of Geophysics and Engineering, 14*(5), 1042-1051. doi:10.1088/1742-2140/aa6fc9

Liu, X., Martín-Calvo, A., McGarrity, E., Schnell, S. K., Calero, S., Simon, J.-M., . . . Vlugt, T. J. (2012). Fick diffusion coefficients in ternary liquid systems from

equilibrium molecular dynamics simulations. *Industrial & Engineering Chemistry Research, 51*(30), 10247-10258.

Liu, X., Schnell, S. K., Simon, J.-M., Bedeaux, D., Kjelstrup, S., Bardow, A., & Vlugt, T. J. (2011). Fick diffusion coefficients of liquid mixtures directly obtained from equilibrium molecular dynamics. *The Journal of Physical Chemistry B, 115*(44), 12921-12929.

Loucks, R. G., Reed, R. M., Ruppel, S. C., & Hammes, U. (2012). Spectrum of pore types and networks in mudrocks and a descriptive classification for matrix-related mudrock pores. *Aapg Bulletin, 96*(6), 1071-1098. doi:10.1306/08171111061

Maginn, E. J., Bell, A. T., & Theodorou, D. N. (1993). Transport Diffusivity of Methane in Silicalite from Equilibrium and Nonequilibrium Simulations. *Journal of Physical Chemistry, 97*(16), 4173-4181. doi:DOI 10.1021/j100118a038

Makrodimitris, K., Papadopoulos, G. K., & Theodorou, D. N. (2001). Prediction of permeation properties of CO2 and N-2 through silicalite via molecular simulations. *Journal of Physical Chemistry B, 105*(4), 777-788. doi:DOI 10.1021/jp002866x

Mao, Z., & Sinnott, S. B. (2001). Separation of organic molecular mixtures in carbon nanotubes and bundles: molecular dynamics simulations. *The Journal of Physical Chemistry B, 105*(29), 6916-6924.

Maple, J. R., Hwang, M. J., Stockfisch, T. P., Dinur, U., Waldman, M., Ewig, C. S., & Hagler, A. T. (1994). Derivation of Class-Ii Force-Fields .1. Methodology and Quantum Force-Field for the Alkyl Functional-Group and Alkane Molecules. *Journal of Computational Chemistry, 15*(2), 162-182. doi:DOI 10.1002/jcc.540150207

Martin, M. G. (2013). MCCCS Towhee: a tool for Monte Carlo molecular simulation. *Molecular Simulation, 39*(14-15), 1184-1194. doi:10.1080/08927022.2013.828208

Martin, M. G., & Siepmann, J. I. (1998). Transferable potentials for phase equilibria. 1. United-atom description of n-alkanes. *Journal of Physical Chemistry B, 102*(14), 2569-2577. doi:DOI 10.1021/jp972543+

Martin, M. G., & Siepmann, J. I. (1999). Novel configurational-bias Monte Carlo method for branched molecules. Transferable potentials for phase equilibria. 2. United-atom description of branched alkanes. *Journal of Physical Chemistry B, 103*(21), 4508-4517. doi:DOI 10.1021/jp984742e

McCarthy, K., Rojas, K., Niemann, M., Palmowski, D., Peters, K., & Stankiewicz, A. J. O. R. (2011). Basic petroleum geochemistry for source rock evaluation. *23*(2), 32-43.

Mehmani, A., Prodanovic, M., & Javadpour, F. (2013). Multiscale, Multiphysics Network Modeling of Shale Matrix Gas Flows. *Transport in Porous Media, 99*(2), 377-390. doi:10.1007/s11242-013-0191-5

Milliken, K. L., & Curtis, M. E. (2016). Imaging pores in sedimentary rocks: Foundation of porosity prediction. *Marine and Petroleum Geology, 73*, 590-608. doi:10.1016/j.marpetgeo.2016.03.020

Monroe, C. W., & Newman, J. (2006). Onsager reciprocal relations for Stefan-Maxwell diffusion. *Industrial & Engineering Chemistry Research, 45*(15), 5361-5367. doi:10.1021/ie051061e

Mosher, K., He, J. J., Liu, Y. Y., Rupp, E., & Wilcox, J. (2013). Molecular simulation of methane adsorption in micro- and mesoporous carbons with applications to coal and gas shale systems. *International Journal of Coal Geology, 109*, 36-44. doi:10.1016/j.coal.2013.01.001

Mutat, T., Adler, J., & Sheintuch, M. (2012a). Single species transport and self diffusion in wide single-walled carbon nanotubes. *Journal of Chemical Physics, 136*(23). doi:Artn 234902

10.1063/1.4727759

Mutat, T., Adler, J., & Sheintuch, M. (2012b). Single species transport and self diffusion in wide single-walled carbon nanotubes. *Journal of Chemical Physics, 136*(23), 234902. doi:10.1063/1.4727759

Natural Gas Weekly Update. (2018). Retrieved from https://www.eia.gov/naturalgas/weekly/

Nelson, P. H. (2009). Pore-throat sizes in sandstones, tight sandstones, and shales. *Aapg Bulletin, 93*(3), 329-340. doi:10.1306/10240808059

Norris, R., & Lewis, J. (1991). *The geological modeling of effective permeability in complex heterolithic facies.* Paper presented at the SPE Annual Technical Conference and Exhibition.

Nvidia. (2018). Retrieved from https://www.nvidia.com/en-us/data-center/hpc/

Oran, E. S., Oh, C. K., & Cybyk, B. Z. (1998). Direct simulation Monte Carlo: Recent advances and applications. *Annual Review of Fluid Mechanics, 30*, 403-441. doi:DOI 10.1146/annurev.fluid.30.1.403

Outlook, A. E. (2012). Us energy information administration (eia). *Department of Energy (DoE)*.

Perilla, J. R., Goh, B. C., Cassidy, C. K., Liu, B., Bernardi, R. C., Rudack, T., . . . Schulten, K. (2015). Molecular dynamics simulations of large macromolecular complexes. *Current Opinion in Structural Biology, 31*, 64-74. doi:10.1016/j.sbi.2015.03.007

Plimpton, S., Crozier, P., & Thompson, A. (2007). LAMMPS-large-scale atomic/molecular massively parallel simulator. *Sandia National Laboratories, 18*, 43.

Raabe, D. (2004). Overview of the lattice Boltzmann method for nano- and microscale fluid dynamics in materials science and engineering. *Modelling and Simulation in Materials Science and Engineering, 12*(6), R13-R46. doi:Pii S0965-0393(04)77661-5

10.1088/0965-0393/12/6/R01

Rahmani, B., & Akkutlu, Y. I. (2015). *Confinement Effects on Hydrocarbon Mixture Phase Behavior in Organic Nanopore*.

Rappe, A. K., Casewit, C. J., Colwell, K. S., Goddard, W. A., & Skiff, W. M. (1992). Uff, a Full Periodic-Table Force-Field for Molecular Mechanics and Molecular-Dynamics Simulations. *Journal of the American Chemical Society, 114*(25), 10024-10035. doi:DOI 10.1021/ja00051a040

Riewchotisakul, S., Akkutlu, I. Y . (2014). Molecular Transport of Simple Gases in Carbon Nanotubes under High Pressure and Temperature using NEMD. *Submitted to AICHE Journal*.

Roy, S., Raju, R., Chuang, H. F., Cruden, B. A., & Meyyappan, M. (2003). Modeling gas flow through microchannels and nanopores. *Journal of Applied Physics, 93*(8), 4870-4879. doi:10.1063/1.1559936

Sander, R., Pan, Z. J., & Connell, L. D. (2017). Laboratory measurement of low permeability unconventional gas reservoir rocks: A review of experimental methods. *Journal of Natural Gas Science and Engineering, 37*, 248-279. doi:10.1016/j.jngse.2016.11.041

Schoen, M., & Hoheisel, C. (1984). The mutual diffusion coefficient D 12 in liquid model mixtures A molecular dynamics study based on Lennard-Jones (12-6) potentials: II. Lorentz-Berthelot mixtures. *Molecular Physics, 52*(5), 1029-1042.

Searles, D. J., & Evans, D. J. (2000). The fluctuation theorem and Green-Kubo relations. *Journal of Chemical Physics, 112*(22), 9727-9735. doi:Doi 10.1063/1.481610

Shale gas and oil plays, Lower 48 States (6/30/2016). (2016). Retrieved from https://www.eia.gov/maps/images/shale_gas_lower48.jpg

Soddemann, T., Dunweg, B., & Kremer, K. (2003). Dissipative particle dynamics: A useful thermostat for equilibrium and nonequilibrium molecular dynamics simulations. *Physical Review E, 68*(4). doi:ARTN 046702 10.1103/PhysRevE.68.046702

Soeder, D. J., Sharma, S., Pekney, N., Hopkinson, L., Dilmore, R., Kutchko, B., . . . Capo, R. (2014). An approach for assessing engineering risk from shale gas wells

in the United States. *International Journal of Coal Geology, 126*, 4-19. doi:10.1016/j.coal.2014.01.004

Sun, H. (1995). (PCFF) Ab-Initio Calculations and Force-Field Development for Computer-Simulation of Polysilanes. *Macromolecules, 28*(3), 701-712. doi:DOI 10.1021/ma00107a006

Sun, H. (1998). COMPASS: An ab initio force-field optimized for condensed-phase applications - Overview with details on alkane and benzene compounds. *Journal of Physical Chemistry B, 102*(38), 7338-7364. doi:DOI 10.1021/jp980939v

Sun, H., Mumby, S. J., Maple, J. R., & Hagler, A. T. (1994). PCFF: An Ab-Initio Cff93 All-Atom Force-Field for Polycarbonates. *Journal of the American Chemical Society, 116*(7), 2978-2987. doi:DOI 10.1021/ja00086a030

Sun, H., Ren, P., & Fried, J. R. (1998). The COMPASS force field: parameterization and validation for phosphazenes. *Computational and Theoretical Polymer Science, 8*(1-2), 229-246. doi:Doi 10.1016/S1089-3156(98)00042-7

Taylor, R. (1993). *Multicomponent mass transfer* (Vol. 2): John Wiley & Sons.

Tersoff, J. (1988). Empirical interatomic potential for silicon with improved elastic properties. *Physical Review B, 38*(14), 9902.

Tersoff, J. (1989). Modeling solid-state chemistry: Interatomic potentials for multicomponent systems. *Physical Review B, 39*(8), 5566.

Theodorou, D. N., Snurr, R. Q., & Bell, A. T. (1996). Molecular dynamics and diffusion in microporous materials. *Comprehensive Supramolecular Chemistry, 7*(Part II), 507.

Ungerer, P., Collell, J., & Yiannourakou, M. (2015). Molecular Modeling of the Volumetric and Thermodynamic Properties of Kerogen: Influence of Organic Type and Maturity. *Energy & Fuels, 29*(1), 91-105. doi:10.1021/ef502154k

Vandenbroucke, M. (2003). Kerogen: from types to models of chemical structure. *Oil & Gas Science and Technology-Revue D Ifp Energies Nouvelles, 58*(2), 243-269. doi:DOI 10.2516/ogst:2003016

Verlet, L. (1967). Computer Experiments on Classical Fluids .I. Thermodynamical Properties of Lennard-Jones Molecules. *Physical Review, 159*(1), 98-+. doi:DOI 10.1103/PhysRev.159.98

Wang, L. (2012). Molecular Dynamics Simulations of Liquid Transport through Nanofiltration Membranes.

Wang, Q., Chen, X., Jha, A. N., & Rogers, H. (2014). Natural gas from shale formation - The evolution, evidences and challenges of shale gas revolution in United States. *Renewable & Sustainable Energy Reviews, 30*, 1-28. doi:10.1016/j.rser.2013.08.065

Wasaki, A., & Akkutlu, I. Y. *Permeability of Organic-rich Shale*.

Weiner, P. K., & Kollman, P. A. (1981). Amber - Assisted Model-Building with Energy Refinement - a General Program for Modeling Molecules and Their Interactions. *Journal of Computational Chemistry, 2*(3), 287-303. doi:DOI 10.1002/jcc.540020311

Whitaker, S. (1996). The Forchheimer equation: A theoretical development. *Transport in Porous Media, 25*(1), 27-61. doi:Doi 10.1007/Bf00141261

Wu, T. H., & Zhang, D. X. (2016). Impact of Adsorption on Gas Transport in Nanopores. *Scientific Reports, 6*. doi:ARTN 23629

10.1038/srep23629

Xiao, J. R., & Wei, J. (1992). Diffusion Mechanism of Hydrocarbons in Zeolites .1. Theory. *Chemical Engineering Science, 47*(5), 1123-1141. doi:Doi 10.1016/0009-2509(92)80236-6

Yan, B. C., Wang, Y. H., & Killough, J. E. (2016). Beyond dual-porosity modeling for the simulation of complex flow mechanisms in shale reservoirs. *Computational Geosciences, 20*(1), 69-91. doi:10.1007/s10596-015-9548-x

Yang, J., Ren, Y., Tian, A. M., & Sun, H. A. (2000). COMPASS force field for 14 inorganic molecules, He, Ne, Ar, Kr, Xe, H-2, O-2, N-2, NO, CO, CO2, NO2, CS2, and SO2, in liquid phases. *Journal of Physical Chemistry B, 104*(20), 4951-4957. doi:DOI 10.1021/jp992913p

Yang, R. Y., Huang, Z. W., Yu, W., Li, G. S., Ren, W. X., Zuo, L. H., . . . Sheng, M. (2016). A Comprehensive Model for Real Gas Transport in Shale Formations with Complex Non-planar Fracture Networks. *Scientific Reports, 6*. doi:ARTN 36673

10.1038/srep36673

Yi, J., Akkutlu, I. Y., Karacan, C. O., & Clarkson, C. R. (2009). Gas sorption and transport in coals: A poroelastic medium approach. *International Journal of Coal Geology, 77*(1-2), 137-144. doi:10.1016/j.coal.2008.09.016

Zhang, P. W., Hu, L. M., Meegoda, J. N., & Gao, S. Y. (2015). Micro/Nano-pore Network Analysis of Gas Flow in Shale Matrix. *Scientific Reports, 5*. doi:ARTN 13501

10.1038/srep13501

Zhou, B., Xu, R. N., & Jiang, P. X. (2016). Novel molecular simulation process design of adsorption in realistic shale kerogen spherical pores. *Fuel, 180*, 718-726. doi:10.1016/j.fuel.2016.04.096

Zottl, A., & Stark, H. (2014). Hydrodynamics Determines Collective Motion and Phase Behavior of Active Colloids in Quasi-Two-Dimensional Confinement. *Physical Review Letters, 112*(11). doi:ARTN 118101

10.1103/PhysRevLett.112.118101

APPENDIX

DETAILS FOR MOLECULAR SIMULATION

The OPLS united atom model (William L Jorgensen, Maxwell, & Tirado-Rives, 1996; Kaminski, Friesner, Tirado-Rives, & Jorgensen, 2001) is used to simulate CH_4 molecule and $-CH_3$, $-CH_2-$ groups in butane and octane, in other words, Hydrogen atoms are not treated separately. If the carbon atoms are allowed to move freely, to model the carbon atoms within carbon nanotube, the 3-body Tersoff potential is used, otherwise, they are kept at fixed positions (Tersoff, 1988, 1989).

Prior to molecular dynamics simulation, the simulation boxes are charged using GCMC (μVT) simulations, varying chemical potentials, at the given temperatures, to find the chemical potential ~ pressure relationships for both single and multicomponent cases. Also, the pressure gradient ~ external force relationship can be calculated with these correlations. Specifically, a grand canonical Monte Carlo (GCMC) simulation simulate the real fluid behavior under the given chemical potentials of each component,

Table 4. Lennard-Jones parameters used in Monte Carlo simulations and molecular dynamics simulations.

Atom/molecule	Model	ϵ/k_B, K	σ, nm
Carbon	-	28.0	0.340
Methane	OPLS-UA	147.9	0.373
$-CH_2-$	OPLS-UA	46.0	0.395
$-CH_3$	OPLS-UA	97.9	0.375

volume and temperature. The equilibrium can be reached by allowing intra-box, creation and annihilation moves in the simulation box. Intra-box moves controls temperature, and creation/annihilation moves controls chemical potential. The three types of moves are of the same probability. The creation move is done by creating a molecule at a random location and random orientation; the annihilation move is done by randomly choosing a molecule and removing it from the simulation. The creation and annihilation moves are accepted to ensure microscopic reversibility and guarantee that the distribution of states conforms to the Boltzmann distribution. During the GCMC simulation, intra-box moves, rotation move, creation move, and annihilation move are all allowed and only limited in the confined space inside the carbon nanotubes.

FORCEFIELD PARAMETERS

In the flow simulation, OPLS-AA force field is used to describe fluid molecules, with bond, angles, dihedrals described in the equation forms below.

$$E = K(r - r_0)^2 \quad \textbf{Equation 33}$$

$$E = K(\theta - \theta_0)^2 \quad \textbf{Equation 34}$$

$$E = \frac{1}{2}K_1[1 + cos(\phi)] + \frac{1}{2}K_2[1 - cos(2\phi)] + \frac{1}{2}K_3[1 + cos(3\phi)] + \frac{1}{2}K_4[1 - cos(4\phi)] \quad \textbf{Equation 35}$$

Table 5. Force field parameters used to calculate average parameters for the simplified molecular model

Atom name	Corresponding atom type in PCFF force field	ϵ, Kcal/mole	σ, Angstroms	Atomic mass, grams/mole	q, electron charge
C	c1	0.054	3.573	12.0107	0
H	hc	0.020	2.668	1.00794	0
N	nh	0.134	3.626	14.0067	0
O	oc	0.240	3.149	15.9994	0
S	sc	0.071	3.588	32.065	0

Table 6. Other force field parameters used in molecular simulations (Makrodimitris, Papadopoulos, & Theodorou, 2001; Martin & Siepmann, 1998, 1999)

Atom type	ϵ, Kcal/mole	σ,	Atomic mass, grams/mole	q, electron charge
CH_4	0.2941	3.730	16.0425	0
CH_3	0.1947	3.75	15.035	0
CH_2	0.09141	3.95	14.027	0
C (in CO_2)	0.05589	2.757	12.0107	0.6512
O (in CO_2)	0.15998	3.033	15.9994	-0.3256

Bond type	Bond coefficient, Kcal/Angstrom^2	Distance, Angstrom
CH_x-CH_y	317.0	1.54
C=O (in CO_2)	1283.34	1.15

Angle type	Angle coefficient, Kcal/rad^2	Angle, degree
CH_x-(CH)-CH_y	62.1	114
O=C=O (in CO_2)	147.7	180

Dihedral type	K_1, Kcal	K_2, Kcal	K_3, Kcal	K_4, Kcal
CH_x-(CH_2)-(CH_2)-CH_y	1.4108	-0.27104	3.14477	0

BASIC INFORMATION OF KEROGEN BUILDING BLOCKS

Table 7. Statistical information of kerogen building blocks

Kerogen building block	Total number of Atoms	C	H	N	O	S	H/C	O/C
I-A	659	251	385	7	13	3	1.53	0.05
II-A	579	252	294	6	24	3	1.17	0.10
II-B	518	234	263	5	14	2	1.12	0.06
II-C	481	242	219	5	13	2	0.90	0.05
II-D	292	175	102	4	9	2	0.58	0.05
III-A	468	233	204	4	27	0	0.88	0.12

SUPPLEMENTARY INTERACTION TERMS FOR PCFF, CVFF FORCE FIELDS

To validate the simplified molecular model, CVFF and PCFF shall include more interactions to better describe the exact kerogen molecule building block. For CVFF force field, the equivalency table is slightly expanded to accommodate more interaction types, both CVFF and PCFF have included additional bond and angle coefficients based on similar bonds and angles. For dihedrals and improper dihedrals which are not included in CVFF and PCFF, they are not taken into consideration. These parameters are listed in Table 8 through Table 12.

Table 8. Equivalency table for CVFF force fields

Type	NonB	Bond	Angle	Torsion	OOP
hs	h	h	h	h	h
hn	hn	h	h	h	h
c5	c'	cp	cp	cp	cp
cs	c'	cp	cp	cp	cp
np	n	cp	cp	cp	cp
sh	s	s	s	s	s
sp	s'	s	s	o	o

Table 9. Supplementary bond coefficients for CVFF

Quadratic bond		Parameters		Equivalent to	
I	J	R0	K2	I	J
cp	c=	1.34	280	cp	c5
cp	o	1.37	400	c'	o

Table 10. Supplementary angle coefficients for CVFF

Quadratic angle			Parameters		Equivalent to		
I	J	K	Theta0	K2	I	J	K
cp	cs	sp	111.039	88.7595	sp	cs	c5
c2	sh	hs	106	58.5	c	o	ho
cp	c1	oh	109.5	70	o	c	o
c5	c2	c'	110.5	46.6	c=	c	c=
c2	n	c5	118	111	c'	n	c
c1	n	c5	118	111	c'	n	c
c5	c1	oh	109.5	70	o	c	o
cp	c2	c'	110.5	46.6	c=	c	c=
o	c2	cp	109.5	70	o	c	o
c5	c5	op	120	90	c5	cp	np
h	c5	op	120	40	h	c5	np
cp	c1	o	109.5	70	o	c	o
cp	cp	c=	120	90	cp	cp	no
cp	c=	c=	120	90	c5	c5	c5
cp	c=	c2	120	44.2	c	c5	c5
cp	c=	h	120	37	c5	c5	h
c1	c2	c=	110.5	46.6	c=	c	c=
cp	o	cp	114	75.1	cp	np	c5
o	c2	np	109.5	70	o	c	o
o	c1	c5	110.5	46.6	c=	c	c=
cp	c1	c'	110.5	46.6	c=	c	c=
c1	c'	cp	120	44.2	c	c5	c5

Table 11. Supplementary bond coefficients for PCFF

Quadratic bond		Parameters				Equivalent to	
I	J	R0	K2	K3	K4	I	J
c	nn	1.452	327.1657	-547.899	526.5	c	n
cp	c=2	1.3521	545.2663	-1005.63	1225.742	c=	c=1
npc	c1	1.452	327.1657	-547.899	526.5	c	n
npc	c2	1.452	327.1657	-547.899	526.5	c	n

Table 12. Supplementary angle coefficients for PCFF

Quadratic angle			Parameters				Equivalent		to
I	J	K	Theta0	K2	K3	K4	I	J	K
c1	c5	nh	120.05	44.7148	-22.735	0	c	cp	np
c2	c5	nh	120.05	44.715	-22.735	0	c	cp	np
c1	nb	c2	107.513	42.518	-21.756	-4.3372	h*	nn	h*
c1	nb	c5	111.68	84.516	-48.553	0	cp	np	cp
c2	c1	nb	117.2847	55.443	0	0	c	c	n=
c2	c2	nb	117.2847	55.443	0	0	c	c	n=
c2	nb	c5	111.68	84.5159	-48.553	0	cp	np	cp
c5	c1	oh	106.1764	74.4143	-12.602	-48.785	c_0	c	o
c5	npc	c1	108.22	119.04	-24.206	0	cp	np	nh
c5	npc	c2	108.22	119.04	-24.206	0	cp	np	nh
cp	c=2	c=2	118.9	61.023	-34.993	0	cp	cp	cp
cp	c=2	c2	120.05	44.715	-22.735	0	c	cp	np
cp	c=2	hc	117.94	35.1558	-12.468	0	cp	cp	h
cp	c1	oc	106.1764	74.4143	-12.6018	-48.785	c_0	c	o
cp	c1	oh	106.1764	74.4143	-12.6018	-48.785	c_0	c	o
cp	c2	c_1	111	44.3234	-9.4454	0	cp	c	h
cp	c2	oc	106.1764	74.4143	-12.6018	-48.785	c_0	c	o

Table 12. Supplementary angle coefficients for PCFF (Continued)

Quadratic angle			Parameters				Equivalent		to
cp	cp	c=2	118.9	61.0226	-34.9931	0	cp	cp	cp
cp	oc	cp	104.5	35.7454	-10.0067	-6.2729	c	o	c
hc	c1	nb	107.4989	62.7484	0	0	h	c	n=2
hc	c2	nb	107.4989	62.7484	0	0	h	c	n=2
npc	c1	c1	117.2847	55.4431	0	0	c	c	n=
npc	c1	c2	117.2847	55.4431	0	0	c	c	n=
npc	c1	hc	107.4989	62.7484	0	0	h	c	n=2
npc	c2	hc	107.4989	62.7484	0	0	h	c	n=2
oc	c1	c5	106.1764	74.4143	-12.6018	-48.785	c_0	c	o
oc	c1	cp	106.1764	74.4143	-12.6018	-48.785	c_0	c	o
oc	c2	cp	106.1764	74.4143	-12.6018	-48.785	c_0	c	o
oc	c2	npc	117.2847	55.4431	0	0	c	c	n=
oh	c5	nh	123.42	73.6781	-21.6787	0	cp	cp	o